Dissertation

Search for supersymmetric partners of the top quark in models with compressed mass spectra with the CMS Detector

Ausgeführt zum Zwecke der Erlangung des Akademischen Grades eines Doktors der Technischen Wissenschaften unter der Leitung von

Univ.-Doz. Dr. techn. Dipl.-Ing. Claudia-Elisabeth Wulz

und

Dr. Ivan Mikulec

als verantwortlich mitwirkender Assistent

am Institut für Hochenergiephysik
der Österreichischen Akademie der Wissenschaften und am Atominstitut (E141)

Eingereicht an der Technischen Universität Wien
Fakultät für Physik

VON

Navid K. Rad

Matrikelnummer 1428507
navid.rad@cern.ch

Wien, am 24.Oktober 2018

ای دل تو به اسرار معمّا نرسی
در نکتهٔ زیرکانِ دانا نرسی
اینجا به می لعل بهشتی می ساز
کانجا که بهشت است رسی یا نرسی

خیّام نیشابوری

"Oh dear! The secrets of this labyrinth, you may never reach!
The wisdom of the sages, you may never reach!
Here! With this crimson wine raise a paradise
For the paradise there, you may never reach!"
Omar Khayyam

Abstract

Supersymmetry (SUSY) is one of the most promising theories for physics beyond the standard model as it explains many of the current problems with the standard model of particle physics (SM). For instance, in many minimal supersymmetric extensions of the SM the lightest supersymmetric particle (LSP) is a stable weakly interacting particle and is therefore an excellent dark matter candidate. However, searches at Tevatron, LEP and the LHC have not been able to find any signs of SUSY so far. This lack of indications for SUSY may be explained if the LSP and the next-to-lightest SUSY particle have a small mass difference, a scenario which is referred to as *compressed SUSY*. In particular, SUSY scenarios with a light top squark ($\widetilde{t}$) are well motivated since they allow for a natural mechanism to stabilize the loop corrections to the Higgs mass by partially cancelling the contributions coming from the top quark. Additionally, the co-annihilation cross section between the LSP and a light top squark can predict the dark matter relic density which is observed in the universe. This thesis presents a search for the pair production of the top squarks in SUSY models with compressed mass spectra using the 2016 proton-proton collision data collected at the CMS detector of the LHC. The single lepton channel of the four-body ($\widetilde{t} \to \mathrm{b}ff'\,\mathrm{LSP}$) and chargino-mediated ($\widetilde{t} \to \mathrm{b}\widetilde{\chi}_1^+ \to \mathrm{b}ff'\,\mathrm{LSP}$) decays of the top squark are investigated. The data are found to be compatible with the predicted SM background processes and the results are used to set limits on the production cross section of the top squark. Assuming 100% branching fraction of each decay mode, top squark masses of up to 500 and 540 GeV are excluded at 95% confidence level for the four-body and chargino-mediated decays respectively.

Deutsche Kurzfassung

Die Supersymmetrie (SUSY) kann viele der aktuellen Probleme des Standardmodells der Teilchenphysik (SM) lösen und ist daher eine der vielversprechendsten Theorien für Physik jenseits des Standardmodells (BSM). In vielen minimalen supersymmetrischen Erweiterungen des SMs ist das leichteste supersymmetrische Teilchen (LSP) ein stabiles, schwach wechselwirkendes Teilchen und dadurch ein idealer Kandidat für Dunkle Materie. Verschiedenste Analysen am Tevatron, LEP und LHC waren bisher erfolglos in der Suche nach Anzeichen von SUSY. Das Ausbleiben dieser Hinweise kann durch ein als *compressed SUSY* bekanntes Szenario erklärt werden, in dem die Massendifferenz zwischen dem LSP und dem nächst leichteren SUSY Teilchen gering ist. SUSY Szenarien mit einem leichen Top-Squark ($\widetilde{t}$) werden durch einen natürlichen Mechanismus, der die Beiträge des Top-Quarks zur Higgsmasse teilweise aufhebt und damit die Schleifenkorrekturen stabilisiert, motiviert. Zusätzlich kann der Koannihilationswirkungsquerschnitt zwischen dem LSP und einem leichten Top-Squark die heute gemessene Dichte der Dunklen Materie korrekt vorhersagen. Die vorliegende Arbeit präsentiert eine Suche für Paarproduktion von Top-Squarks in SUSY Modellen mit komprimierten Massenspektren in Proton-Proton Kollisionsdaten, die 2016 vom CMS Detektor am LHC aufgezeichnet wurden. Der Einzelleptonkanal des Vierkörperzerfalls ($\widetilde{t} \to \mathrm{b}ff'\,\mathrm{LSP}$) und der chargino-vermittelte Zerfall ($\widetilde{t} \to \mathrm{b}\widetilde{\chi}_1^+ \to \mathrm{b}ff'\,\mathrm{LSP}$) werden untersucht. Die gemessenen Daten sind in guter Übereinstimmung mit der Vorhersage der SM Hintergrundprozesse und die Ergebnisse werden zur Bestimmung von Obergrenzen des Produktionswirkungsquerschnitts des Top-Squarks verwendet. Mit der Annahme eines 100% Verzweigungsverhältnisses sowohl für den Vierkörper- als auch den chargino-vermittelten Zerfallskanal werden Top-Squarkmassen von bis zu 500 beziehungsweise 540 GeV mit einem Konfidenzintervall von 95% ausgeschlossen.

Contents

Introduction

The standard Model (SM) of particle physics [1–3] has been extremely successful in describing the observed fundamental particles and their interactions at high energy physics experiments. The Higgs boson as predicted by Higgs, Englert, and Brout [4, 5] was the last missing piece of the SM and its observation by the ATLAS and CMS collaborations [6, 7] in 2012 was yet another testimony for the veracity of the SM. Despite the extraordinary success of the SM, the observation of neutrino mass [8, 9] and cosmological observations of dark matter [10] and dark energy [11] all suggest that SM can only be an effective theory which is to be replaced by a more fundamental theory at energy scales much larger than the electroweak scale. Over the years many extensions of the SM have been proposed in an attempt to bridge the gap between SM and a unified theory of the fundamental forces. Supersymmetry (SUSY) [12–16], in particular, has been one of the promising extensions of SM and has been the focus of numerous searches at high energy physics experiments since its inception. In many SUSY scenarios, the neutralino, a new neutral and weakly interacting stable particle, is considered to be the lightest supersymmetric particle (LSP) and can be a suitable dark matter candidate. Due to their weakly interacting nature, the neutralinos, similar to neutrinos, cannot be observed directly by the detectors and their presence can only be deduced from the imbalance in the momenta of the observed particles in the event —a quantity referred to as *missing transverse energy*. Furthermore, the supersymmetric partner of the top quark, the top squark, may help stabilize the quantum corrections to the bare Higgs boson mass, and thus offering a solution to the so-called electroweak hierarchy problem.

This thesis describes a search for the pair production of top squarks and their four-body or chargino-mediated decays into neutralinos in supersymmetric models in which the mass difference between the top squark and the neutralino is less than the W boson mass. The analysis is performed on the data collected by Compact Muon Solenoid (CMS) detector during the 2016 proton-proton run of the Large Hadron Collider with a center-of-mass energy of 13 TeV and an integrated luminosity of 36 fb^{-1}. This search focuses only on final states with one electron or muon (single lepton channel). The SUSY scenarios considered in this analysis,

referred to as compressed SUSY, are particularly motivated by dark matter constraints as the coannihilation between the top squark and the neutralino can help predict the observed dark relic densities.

The missing transverse energy of the signal events is expected to be much smaller than those of typical SUSY searches since previous searches have not yet excluded relatively light neutralinos in the compressed regions of the SUSY parameter space. Moreover, the small mass differences between the top squark and the LSP results in jets and leptons with very low transverse momenta which may often fail to pass the trigger and reconstruction thresholds of the experiment. Discrimination of signal-like events with respect to the background processes can be achieved by taking advantage of events with an energetic initial state radiation (ISR) which can boost the top squark pair and consequently enhance the missing transverse energy of the event. The dominant SM processes with similar final states as the signal are the production of W and top pairs in association with jets. These background processes are estimated using a semi data-driven method in which the normalization of the corresponding simulated samples are obtained from dedicated regions enriched in the backgrounds. Systematic uncertainties affecting the expected signal and background estimation are taken into account. One of the important sources of uncertainty in this analysis is the modeling of the ISR multiplicity in the simulated samples. The results of the analysis are interpreted within the context of simplified models (SMS) [17] corresponding to the four-body and chargino-mediated decays of the top squark. Additional material such as covariance matrix of the background estimations, and signal efficiency maps are provided in order to facilitate the reinterpretation of the analysis results.

As the author of this document, significant contributions have been made to a recent publication [18] and a previous preliminary result [19] containing the results presented in this thesis. My contribution to the analysis included the simulation of benchmark signal samples for initial studies, optimization of event categorization for an improved sensitivity to the signals of interest, implementing the analysis software framework, estimating the dominant backgrounds, validation of the full background estimation process, estimation of the dominant sources of the uncertainties, performing the statistical interpretation of the results, and performing the statistical combination of the results with the previously published results of the "all hadronic" search involving the same signal processes. I have also presented the results of this analysis and other CMS SUSY searches at SUSY17 (Mumbai, India) and DIS2018 (Kobe, Japan) conferences [20].

Theoretical Introduction

The standard model (SM) of particle physics is a quantum field theory based on the local gauge symmetries which successfully describe the fundamental interactions of particles at the highest energies currently probed by particle physics experiments. In this chapter a very brief overview of SM, some of its greatest achievements will be discussed. Next, we will discuss a few downfalls of SM and how they might give us hints to the physics beyond SM; in particular the basic ideas of supersymmetry and the minimal supersymmetric extension of SM (MSSM) are presented as a possible solution to some of the shortcomings of the SM.

2.1 The Standard Model

The formulation of the standard model has been the result of the interplay between the theoretical ideas and experimental observations carried out since the second half of the 20th century. SM is a relativistic quantum field theory (QFT) which is invariant under local gauge transformations of the symmetry group $SU(3)_C \otimes SU(2)_L \otimes U(1)_Y$. This symmetry group describes three of the four known fundamental interactions in nature, namely the strong, weak and the electromagnetic interactions. Including the fourth interaction, the gravitational force, in the same theoretical framework as the other three is one of the most tantalizing goals of modern physics. Two crucial concepts which have been instrumental in advancing our understanding of high energy phenomena are the principle of gauge invariance and the Noether's Theorem. The gauge principle is essentially the requirement that the laws of physics should not depend on arbitrary gauges or coordinate systems. The seemingly simple requirement indicates that the invariance of a free quantum field theory under some local transformation can be achieved by introducing new interaction terms consisting of the gauge fields which correspond to the generators of the gauge symmetry. The Noether's Theorem on the other hand, guarantees that corresponding to every local symmetry of the theory there exists a conserved current [21]. Therefore these two powerful concepts allow us to not only organize

different fields by their quantum numbers, but also to determine their allowed interactions based on the overarching symmetries.

One complication that arises in the case of SM is the fact that requiring gauge invariance implies massless gauge fields. The theoretical expectation for photons and gluons to be massless is indeed consistent with experimental observations [22]. The mediators of the weak force, on the other hand, have been observed to have relatively large masses [23–26]. Therefore, for SM to be compatible with the gauge principle, some additional mechanism must be responsible for providing mass to the gauge bosons without violating the gauge principle. The solution for this dilemma was proposed by Higgs, Englert and Brout [4,5] in which the gauge bosons acquire mass through spontaneous breaking of electroweak symmetry.

In this chapter we will remind the reader of the field content of the SM, show briefly how the gauge principle can be used to derive each of the interactions in SM and also discuss the mechanism of *spontaneous symmetry breaking*.

2.1.1 Gauge and matter fields of SM

The field content of the SM includes spin-$\frac{1}{2}$ fermionic matter fields, spin-1 gauge fields which are the force mediators and last but not least the scalar field known as the Higgs field. The fundamental interactions are mediated by the gauge bosons which arise as the generators of the symmetry group for the interaction. For example, for a special unitary symmetry $SU(N)$, the number of generators is given by $N^2 - 1$, where N is the degree of the group. This relation immediately gives important insights to the required number of gauge fields for each interaction. The strong interaction between colored particles is governed by $SU(3)$ and is therefore mediated by 8 colored gluon fields. The electroweak interactions are governed by $SU(2) \otimes U(1)$, and are mediated by a linear combination of $W^{\pm}$ and the Z and the photon. The reason for the mixing of these gauge fields will be discussed in Sec. 2.1.4.

The matter fields of the SM are divided into three nearly identical generations which share the same quantum numbers but have different masses. Each generation consists of a charged lepton, a neutrino, an up-type and a down-type quark. Quarks in the SM are the only type of particles which interact with all four fundamental forces. Leptons do not have a color charge and neutrinos only interact with the weak and gravitational forces. An important feature of SM is its chiral structure which allows for left- and right-handed particles to have different interactions[1]. More specifically, the weak gauge bosons only interact with the left-handed particles and the right handed anti-particles. This creates an additional difficulty in writing mass terms for the fermions since a mass term would mix the left and right chiralities

[1]Here and throughout the rest of this thesis the "handedness" of the particles refers to their weak hypercharge and not their helicity.

	1st Generation	2nd Generation	3rd Generation
Leptons:	$\begin{pmatrix}\nu_e\\ e^-_L\end{pmatrix}$, e^-_R	$\begin{pmatrix}\nu_\mu\\ \mu^-_L\end{pmatrix}$, μ^-_R	$\begin{pmatrix}\tau_e\\ \tau^-_L\end{pmatrix}$, τ^-_R
Quarks:	$\begin{pmatrix}\mathrm{u}_L\\ \mathrm{d}_L\end{pmatrix}$, u_R , d_R	$\begin{pmatrix}\mathrm{c}_L\\ \mathrm{s}_L\end{pmatrix}$, c_R , s_R	$\begin{pmatrix}\mathrm{t}_L\\ \mathrm{b}_L\end{pmatrix}$, t_R , b_R

Table 2.1: Organization of the SM fermions for different generations in terms of left handed doublets and right handed singlets.

and therefore break the $SU(2)_L$ symmetry. Interestingly, the same mechanism that makes it possible to give mass to the weak gauge bosons, can provide mass for fermions as well. The left-handed fermions are then organized into chiral doublets and right handed ones are singlets as shown in Tab. 2.1. It should be noted that since neutrinos only[2] interact with the weak force, and weak gauge bosons do not interact with right-handed fermions, the right handed neutrinos would have no way of communicating with the SM particles. Thus, these right handed neutrinos do not play a role in the formulation of SM as described here. In the following sections the gauge symmetries of the SM and their implicates are briefly described.

2.1.2 Quantum Electrodynamics

The free Lagrangian density for a massive spin-$\frac{1}{2}$ fermionic field, ψ, is given by:

$$\mathcal{L}_{\text{fermion}} = i\bar{\psi}(x)\gamma^\mu\partial_\mu\psi(x) - m\bar{\psi}(x)\psi(x), \tag{2.1}$$

where the conjugate field, $\bar{\psi}$, is defined by $\bar{\psi} = \psi^\dagger\gamma^0$ and m is the Dirac mass. The application of the Euler-Lagrange equation on this Lagrangian does indeed result in the Dirac equation which is the correct equation of motion for spin-$\frac{1}{2}$ fermions. This Lagrangian is invariant under a global U(1) transformation of the form:

$$\psi(x) \to \psi'(x) \equiv e^{iq\theta}\psi(x) \tag{2.2}$$

where q and θ are real constants. The global gauge invariance implies that any choice for the phase of $\psi(x)$ is arbitrary and will not change the equations of motion for the field so long as θ does not depend on the space-time coordinates. A local transformation where $\theta \equiv \theta(x)$ would on the other hand break the symmetry due to the action of partial derivative on the transformed field. Imposing the Lagrangian to be invariant under a local gauge transformation is then seen as a natural requirement since the choice of a reference point for the coordinate

[2] Gravitational interactions of neutrinos can be neglected due to their small mass.

system must not have an effect on the physics. Since the partial derivative, ∂_μ is the culprit of local symmetry breaking, we would like to promote it to a covariant derivative, $\mathcal{D}_\mu$, so that it would transform like the field:

$$\mathcal{D}_\mu\psi \to (\mathcal{D}_\mu\psi)' = e^{iq\theta}\mathcal{D}_\mu\psi. \tag{2.3}$$

In order to achieve this goal we define the covariant derivative as:

$$\mathcal{D}_\mu = \partial_\mu - iqA_\mu(x) \tag{2.4}$$

where q is a coupling constant and A_μ is a spin-1 gauge field (since it has one Lorentz index) with the following transformation property:

$$A_\mu(x) \to A'_\mu(x) = A_\mu(x) + \partial_\mu\theta \tag{2.5}$$

Now we can rewrite the Lagrangian as:

$$\mathcal{L} = i\bar{\psi}(x)\big(\gamma^\mu\mathcal{D}_\mu - m\big)\psi(x) \tag{2.6}$$

$$= i\bar{\psi}(x)\big(\gamma^\mu(\partial_\mu - iqA_\mu) - m\big)\psi(x) \tag{2.7}$$

comparing Eq. 2.7 with the free Lagrangian that we started with, we can notice a new term, $\bar{\psi}A_\mu\psi$, which indicates the interaction between the fermion field and gauge field. The requirement of the free Lagrangian to be invariant under the local gauge transformation has led to a new term describing the dynamics of the fields; this is indeed the powerful consequence of gauge principle. For A_μ to be a physical spin-1 field it must also follow the so-called Proca Lagrangian:

$$\mathcal{L}_{Proca} \equiv -\frac{1}{4}F_{\mu\nu}(x)F^{\mu\nu}(x) + \frac{1}{2}m_A^2A_\mu A^\mu \tag{2.8}$$

Where m_A is the mass of gauge boson and $F_{\mu\nu} \equiv \partial_\mu A_\nu - \partial_\nu A_\mu$. Since we would like this theory to describe the electromagnetic interaction at the classical level, we can identify q as the electric charge, A_μ as the photon field, and $F_{\mu\nu}$ as the Maxwell's electromagnetic field strength tensor. Adding the mass term from the Proca Lagrangian to Eq. 2.7 would spoil the $U(1)$ symmetry, therefore the QED theory predicts (postdicts) that photons are massless. The full QED Lagrangian can then be written in full as:

$$\mathcal{L}_{QED} = i\bar{\psi}(x)(\gamma^{\mu}\mathcal{D}_{\mu} - m)\psi(x) - \frac{1}{4}F_{\mu\nu}(x)F^{\mu\nu}(x). \tag{2.9}$$

Knowing the gauge symmetry of this group we can take advantage of the Noether's Theorem to get the conserved electromagnetic current, $J_{\mu} = q\bar{\psi}\gamma_{\mu}\psi$. Also applying the Euler-Lagrange equation on the QED Lagrangian in terms of the gauge field gives the following expression:

$$\partial_{\mu}F^{\mu\nu} = qJ^{\nu} \tag{2.10}$$

which in addition to the current conservation law form the Maxwell equations. When we apply the Euler-Lagrange procedure in terms of the fermion field one obtains the equations:

$$i\gamma_{\mu}\partial^{\mu}\psi - m\psi = q\gamma_{\mu}A^{\mu}\psi \tag{2.11}$$

which is the Dirac equation in the electromagnetic field, indicating the interaction of the fermionic fields with photon. The calculations done in the framework of QED for the anomalous magnetic moment of the electron have been verified by experiments to an unprecedented precision.

2.1.3 Quantum Chromodynamics

Quantum Chromodynamics is the gauge theory which describes the interactions between the quarks and gluons and is the underlying theory responsible for the zoo of baryons and mesons. The free Lagrangian of QCD has similar structure to that of QED, however the symmetry group responsible for the interactions in QCD is the $SU(3)$ group. The $SU(3)$ group is a non-abelian group which means that the generators of the group do not commute which each other. The physical consequence of having a non-abelian gauge group is that the gauge bosons of the theory (gluons in the case of QCD) have self interactions. The $SU(3)$ charge of quarks is referred to as the color charge and is commonly labeled as red, green or blue. The free Lagrangian for a quark of a given flavor, f, can be written as:

$$\mathcal{L}_{free} = \bar{q}(x)_f(i\gamma^{\mu}\partial_{\mu} - m_f)q(x)_f. \tag{2.12}$$

Here q is a vector in the color space:

$$q = \begin{pmatrix} q_r \\ q_g \\ q_b \end{pmatrix}. \tag{2.13}$$

The Lagrangian in Eq. 2.12 is invariant under global $SU(3)$ transformations in the color space. In order to extend this invariance to local $SU(3)$ transformations, we can again promote the partial derivative to a covariant derivative in such a way to ensure local gauge invariance; however, since there are eight $SU(3)$ generators, we now need eight new gauge fields to achieve this task. The covariant derivative then becomes:

$$\mathcal{D}_\mu = \partial_\mu - \frac{i}{2}\mathrm{g}_s G^a_\mu \lambda_a \tag{2.14}$$

Here λ_a are the Gell-Mann matrices with $a = 1..8$ and therefore G_a are the gluon fields which mediate the strong interactions. The QCD Lagrangian can be written as:

$$\mathcal{L}_{QCD} = \sum_f \bar{q}_f (i\gamma_\mu \mathcal{D}^\mu - m_f) q_f - \frac{1}{4} G^a_{\mu\nu} G^{a\mu\nu}, \tag{2.15}$$

where $G^a_{\mu\nu}$ is the gluon field strength and is defined by:

$$G^a_{\mu\nu} = \partial_\mu G^a_\nu - \partial_\nu G^a_\mu + g_s f^{abc} G^b_\mu G^c_\nu. \tag{2.16}$$

The extra term in the gluon field strength tensor, contain the $SU(3)$ structure constants f^{abc}, compared to that of the photon is another product of the non-abelian nature of $SU(3)$ and the source of the gluon self interaction. Similar to photons, gluons must also follow massless Proca Lagrangian. It should be noted that Proca term in the Lagrangian 2.15 includes cubic and quartic self-interaction terms for gluons with the same coupling, g_s, as the quark-gluon vertex.

2.1.4 Electroweak Unification

Although the interactions in QED and QCD are different in many ways, they share a common but important feature of having massless gauge bosons, namely photons and gluons. On the other hand, we know experimentally that the mediators of the weak interaction, the $W^\pm$ and

Z bosons, have masses of 81.4 and 91.2 GeV respectively. This feature indeed hinders writing a gauge invariant Lagrangian for the weak interaction since a mass term for the gauge bosons would break the gauge invariance. Moreover, the weak force interacts differently between the left- and right-handed fermions. More specifically, only left-handed fermions (and right-handed antifermions) interact with the $W^{\pm}$ which is a maximal breaking of charge and parity symmetries, "once-thought" fundamental symmetries of nature.

Knowing that the weak force is mediated by three gauge bosons, a natural first attempt for writing down the symmetry of the interaction would be $SU(2)_L$ group. However, similar to the case of QCD and $SU(3)$ this would result in identical couplings of the gauge bosons to the fermions which we know experimentally to not be true. The electrically charged nature of the W boson may be seen as a hint that the correct symmetry is the $SU(2)_L \otimes U(1)_Y$, which would unify the the weak and electromagnetic interactions. We can write down the free Lagrangian for leptons or quarks of a given family, with the left-handed doublet, ψ_L, and the right-handed singlet, ψ_R, as shown in Tab. 2.1 in the following form:

$$\mathcal{L}_{free} = \bar{\psi}_L \gamma_\mu \partial^\mu \psi_L + \bar{\psi}_R \gamma_\mu \partial^\mu \psi_R. \tag{2.17}$$

Due to the chiral nature of the fermions, a fermion mass term would mix the left and right chiralities to a term of the form $-m(\bar{\psi}_L \psi_R)$, which would automatically break the $SU(2)_L$ symmetry since the doublets and singlets transform differently under the gauge group. For now we set the fermion mass to be zero and assume that some additional mechanism will give mass to the fermions.

The left- and right-handed fields would transform under the local $SU(2)_L \otimes U(1)_Y$ transformation as:

$$\psi_L \to \psi'_L = \exp(\frac{i}{2}\vec{\xi}(x) \cdot \vec{\sigma} + iy\beta(x))\psi_L \tag{2.18}$$

$$\psi_R \to \psi'_R = \exp(iy\beta(x))\psi_R \tag{2.19}$$

where $\vec{\sigma}$ are the three Pauli matrices, y the hypercharge and $\vec{\xi}(x)$ and $\beta(x)$ are arbitrary functions of spacetime coordinate. In order to keep the Lagrangian invariant under this local transformation, we again upgrade to the covariant derivative with the following transformational properties:

$$\mathcal{D}_\mu \psi_L = (\partial_\mu - \frac{i}{2} g \vec{W}_\mu \cdot \vec{\sigma} + \frac{i}{2} g' B_\mu)\psi_L, \tag{2.20}$$

$$\mathcal{D}_\mu \psi_R = (\partial_\mu + \frac{i}{2} g' B_\mu)\psi_R, \tag{2.21}$$

with the new $\vec{W}$ and B fields transforming as:

$$W_\mu^i \to W_\mu^i + \frac{1}{g}\partial_\mu \xi^i - \epsilon^{ijk}\xi^j G_\mu^k, \tag{2.22}$$

$$B_\mu \to B_\mu + \frac{1}{g'}\partial_\mu \beta. \tag{2.23}$$

Using the corresponding massless Proca Lagrangian terms for the $\vec{W}$ and B fields, the electroweak Lagrangian is written as:

$$\mathcal{L}_{ewk} = -\frac{1}{4}\vec{W}^{\mu\nu}\cdot\vec{W}_{\mu\nu} - \frac{1}{4}B^{\mu\nu}B_{\mu\nu} + i\bar{\psi}_L\gamma_\mu\mathcal{D}^\mu\psi_L + i\bar{\psi}_R\gamma_\mu\mathcal{D}^\mu\psi_R \tag{2.24}$$

where the $\vec{W}^{\mu\nu}$ and $B^{\mu\nu}$ are the field strength tensors of the corresponding gauge fields. From the left-handed fermion term and with the help of some algebra, it can be seen only W_μ^1 and W_μ^2 contribute to the charged current terms, e.g lepton-neutrino term or up-antidown terms. Therefore from a linear combination of these two fields we can construct the $W^\pm$ bosons:

$$W_\mu^\pm \equiv \frac{1}{\sqrt{2}}(W_\mu^1 \mp W_\mu^2). \tag{2.25}$$

Obtaining the photon requires a bit more head-scratching, since both remaining fields, W_μ^3 and B_μ can couple to the neutrinos which is electrically neutral. However, it was shown by Glashow, Salam and Weinberg [2,3,27] that these two field could mix to form the photon field, A_μ and also predicted the existence of a new neutral field, Z. The mixing of the neutral components can be written as:

$$\begin{pmatrix} A_\mu \\ Z_\mu \end{pmatrix} = \begin{pmatrix} \cos\theta_w & \sin\theta_w \\ -\sin\theta_w & \cos\theta_w \end{pmatrix} \begin{pmatrix} B_\mu \\ W_\mu^3 \end{pmatrix} \tag{2.26}$$

where the θ_w is the weak mixing angle and is also known as the Weinberg angle. Although the Lagrangian 2.24 can describe the interactions between the fermions and gauge bosons, the lack of mass term for the gauge bosons gives rise to long-range interactions. Next we describe the mechanism responsible giving mass to the weak gauge bosons while keeping the photon massless.

2.1.5 EBH Mechanism

In this chapter we describe the mechanism first proposed by Englert, Brout and Higgs [4, 5] referred to here as *the EBH mechanism* which can break the symmetry and in return provide mass terms for the bosons. This can be achieved with the help of Goldstone's theorem [28–30] which states for every broken symmetry generator there exists a massless field, which is often referred to as the Goldstone boson. These Goldstone fields can then be gauged away and become the longitudinal component of the gauge bosons and hereby bestowing mass upon the previously massless gauge fields. We first introduce a new complex scalar field, ϕ:

$$\phi(x) \equiv \begin{pmatrix} \phi^+ \\ \phi^0 \end{pmatrix}, \tag{2.27}$$

and with an appropriately gauged covariant derivative of the form,

$$\mathcal{D}_\mu \phi = (\partial_\mu - \frac{i}{2} g \vec{W}_\mu \cdot \vec{\sigma} + \frac{i}{2} g' B_\mu)\phi, \tag{2.28}$$

we can write down a general kinetic Lagrangian as:

$$\mathcal{L}_{Higgs} = (\mathcal{D}_\mu \phi)^\dagger (\mathcal{D}^\mu \phi) - V(\phi, \phi^\dagger). \tag{2.29}$$

Now, considering a general potential of the form,

$$V(\phi, \phi^\dagger) = \mu^2 \phi\phi^\dagger + h(\phi\phi^\dagger)^2 \tag{2.30}$$

we can observe that h must be bounded from below if any ground states are to exist. A positive quadratic term produces a trivial minimum, but the case is more interesting for $\mu^2 < 0$ which has a ground state at

$$|\phi_{min}| = \sqrt{\frac{-\mu^2}{2h}}. \tag{2.31}$$

Now the perturbation of the $\mathcal{L}_{Higgs}$ around this minimum, i.e, $\phi(x) = \phi_{min} + H(x)$ breaks the symmetry and leads to a Lagrangian which can be written in terms of $W^\pm$ and Z bosons as:

$$\mathcal{L}_{broken} = \frac{1}{2}\partial_\mu H \partial^\mu H + \mu^2 H^2 + \frac{1}{4} g^2 v^2 \mathrm{W}^+_\mu \mathrm{W}^{-\mu} + \frac{1}{8} v^2 (g^2 + g'^2) Z_\mu Z^\mu \tag{2.32}$$

From this Lagrangian we can identify the masses of the gauge bosons and also the new H field, which we refer to as the Higgs field. The $W^{\pm}$ bosons share the common mass of $\frac{gv}{2}$, the Z boson receives a mass equal to $m_Z = \frac{v}{2}\sqrt{g^2 + g'^2}$, and finally the scalar Higgs field obtains a mass of $m_H = \sqrt{-2\mu^2}$. It must be noted that this mechanism, by design, keeps the photon field, A_μ, massless while giving masses to the $SU(2)$ and also predicts a new massive scalar boson.

The mass problem for the fermion still remains but if the Higgs field also couples to the fermions, then it could also provide with mass as well. Particularly, because the scalar field allows for gauge invariant terms which couple the left-handed doublet and right-handed singlet states of the form $\bar{\psi}_L \phi \psi_R$, referred to as Yukawa terms. After the symmetry is broken the Yukawa Lagrangian can be written as:

$$\mathcal{L}_{Yukawa} = -\frac{v+H}{\sqrt{2}} \sum_{i}^{fermions} y_i \bar{\psi}_L \psi_R \tag{2.33}$$

where y_i are the Yukawa couplings which are essentially the proportionality constant between the mass of a fermion and the Higgs vacuum energy, v. Therefore, mass of a fermion f can be written in terms of its Yukawa coupling as:

$$m_f = y_f \frac{v}{\sqrt{2}} \tag{2.34}$$

For each Yukawa mass term there is also an interaction term between the fermion and the Higgs field which is also proportional to the mass of the fermion. Followed by the observation of Higgs boson with mass of approximately 125 GeV by the ATLAS and CMS experiments [6,31], the boson's various properties such as its spin and coupling strengths to SM particles have so far been measured to be compatible with the SM Higgs boson by both experiments. The calculated production cross sections and decay branching fractions of the Higgs boson within the context of SM have been shown to match the observations by both experiments (see Fig. 2.1). In particular, the recent observations of the Higgs boson production in association with a top pair [32,33], the decay of Higgs boson to a pair of bottom quarks [34,35] by ATLAS and CMS Collaborations and its decay into a pair of τ leptons [36] by the CMS Collaboration have further tested the validity of the SM and confirmed the Yukawa mechanism.

Despite the numerous achievements of the SM, its few shortcomings are indications that it is not complete theory and may lose validity some higher energies. Some of these issues are discussed in the next section.

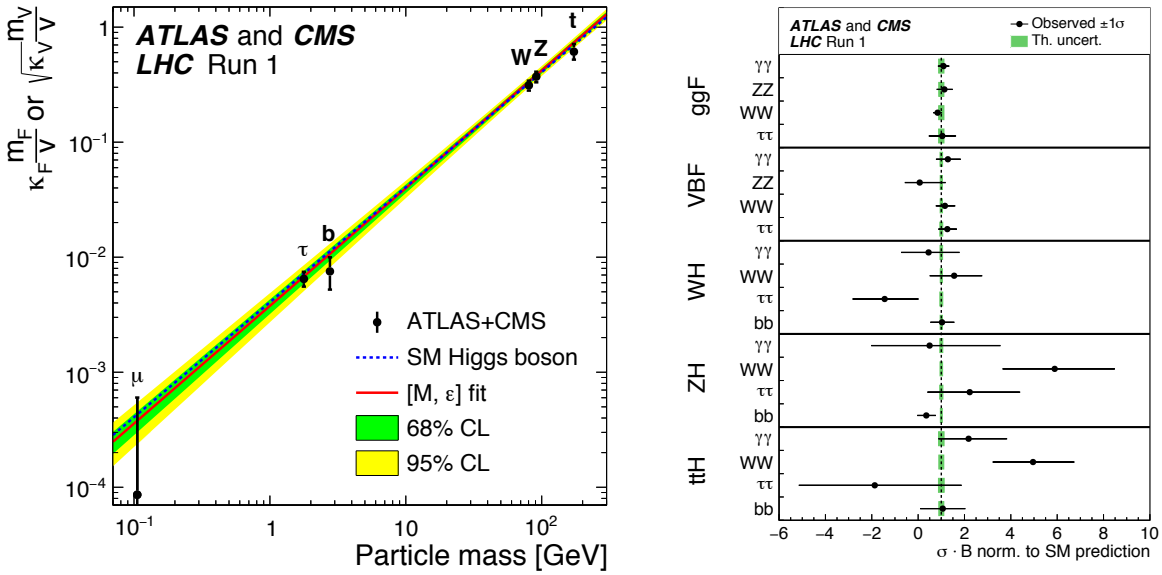

Figure 2.1: Top: Shows the best fit values, using the combined measurements from ATLAS and CMS, for parameters $\kappa_F \frac{m_F}{v}$ for fermions and $\kappa_V \frac{m_V}{v}$ for weak vector bosons, where $\kappa_{V,F}$ and $m_{V,F}$ are the coupling modifiers and masses of vector bosons and fermions. Bottom: Shows the best fit values for cross section times branching fraction of various Higgs production modes and decay channels for the combination of the ATLAS and CMS measurements. The error bars show the 1 standard deviation of the measurement and indicate the good agreement between the measured and the predicted SM values [37].

2.1.6 Shortcomings of SM

The predictions of the standard model have been extraordinarily successful in describing the numerous experimental observations performed in the previous and current centuries. From the magnetic dipole moment of the electron [38] to the production cross sections of various particles (see Fig. 2.2), the observed quantities match the predicted values from SM calculations with an unparalleled precision. Despite the unrivaled success of SM, there exist numerous unanswered questions and limitations in the theory which yield many to believe that SM is only an effective field theory (EFT) valid up to some higher energy (Λ), beyond which a more general theory is needed. The observation of neutrino mass by the SuperKamiokande collaboration [8] is perhaps the most compelling evidence for suggesting that the SM cannot be the ultimate theory of nature. This is due to the fact that within the context of SM, neutrinos are massless, and an extension of the SM Lagrangian would be needed to provide the mass terms for these particles. Moreover, the quantum gravitational effects, which SM is fully blind to, become increasingly more important at energies closer to the planck mass. Therefore the higher energy theory must be able to incorporate gravity within the same framework as the SM. However, accepting the SM as an EFT results in another distressing issue, referred to as the electroweak hierarchy problem, which can be expressed as the fact that the observed

mass of the Higgs boson is $\sim\mathcal{O}(16)$ orders of magnitude smaller than the value expected from the cut-off scale Λ at which SM EFT becomes invalid and the quantum gravitational effects take over.

SM also faces multiple challenges from the large scale observations of the universe. Namely, the the rotation curves of galaxies, gravitational lensing effects of distant objects, and the power spectrum of cosmic microwave background (CMB) point to the existence of a mass source, referred to as dark matter, which does not correspond to any of the known forms of matter. The recent measurements by the Planck Collaboration, estimate the relative contribution of dark matter density to be $12.00\pm0.12\%$ of the total matter and energy content of the universe (more than 5 times that of the regular matter) [39]. The same studies also estimate that the majority of the current energy content of the universe ($68.48\pm0.73\%$) is a uniform energy form referred to as dark energy which is responsible for the acceleration in the expansion of the universe. In SM the ground state energy of quantum fields, believed to be a contributing source to dark energy, is calculated to be $\sim\mathcal{O}(120)$ orders of magnitude larger than the observed value [40]. This so called cosmological constant problem is perhaps an even deeper mystery which further indicates to the gaps in our understanding of fundamental fields of nature. Additionally, the asymmetry between matter and antimatter in the universe as determined from the abundances of light elements in the intergalactic medium and the power spectrum of the CMB cannot be fully explained within the context of SM [41–43]. Some of these problems will be discussed in the context of supersymmetry in some more detail in the next chapter.

2.2 Supersymmetry

Supersymmetry (SUSY) is a theory for physics beyond the SM (BSM) which has been studied extensively since it was first proposed in the early 1970s. The symmetries involved in SUSY are radically different from the gauge symmetries discussed in Sec. 2.1. The SM gauge symmetries involve the internal degrees of freedom of the fields, which correspond to transformations of the fields themselves, while SUSY is a spacetime symmetry and is innately related to the Poincaré symmetry.

An interesting question, particularly in regards to obtaining a quantum theory of gravity, is whether there exists a theory which can relate the Poincaré symmetry with the internal gauge symmetries of QFTs. It should be noted that within the context of the SM, such a relationship already does exist, but only in trivial fashion, since the gauge generators commute with the Poincaré generators. In fact, according to the Coleman-Mandula (CM) theorem [45], there is no non-trivial way for the Poincaré and internal gauge symmetries to be combined.

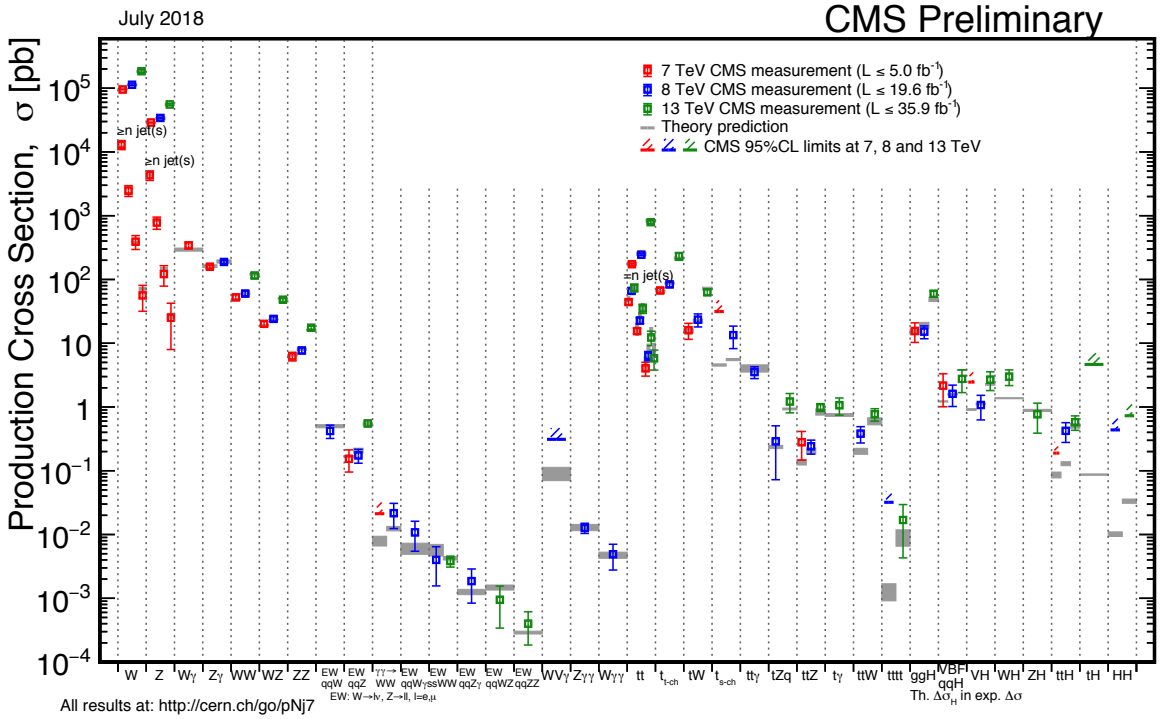

Figure 2.2: Summary of the theoretical cross sections for various SM processes and their comparison with the observed values by the CMS experiment [44].

This no-go theorem would have significantly disrupted any attempt for unifying gravity within the context of gauge QFTs, had it not been for its successor, the Haag-Łopuszanski-Sohnius theorem [12]. This generalized version of the CM theorem proved that by including fermionic generators in addition to the bosonic ones, the Poincaré symmetry can be combined with the internal symmetries into what is now called the supersymmetric algebra. The supersymmetric algebra is a generalization of the Lie algebra and is also known as graded algebra.

The distinction between fermionic and bosonic generators is that a fermionic generator transforms a bosonic (fermionic) state into a fermionic (bosonic) state while a bosonic generator does not change the spin of the state. For operators of a Lie algebra, O_i, the graded algebra can be written as:

$$O_i O_j - (-1)^{\eta_i \eta_j} O_j O_i = i C_{ij}^k O_k, \tag{2.35}$$

where i, j, k are the indices of the operator and C_{ij}^k are the structure constants. The n_i is the grading of the operator and has value of 0 for bosonic generators and 1 for fermionic ones. It can be seen that for a bosonic (fermionic) generators Eq. 2.35 becomes a commutation (anti-commutation) relation. The generators of spacetime symmetries in SM are bosonic generators of Poincaré, Lorentz and rotational symmetries. In SUSY these are complemented with the

fermionic generators, Q_α, known as supercharge generators, which schematically have the property:

$$Q|\text{fermion}> \propto |\text{boson}>, \qquad Q|\text{boson}> \propto |\text{fermion}>. \tag{2.36}$$

In principle, the theory may contain $\mathcal{N}$ supersymmetric transformations, where in four dimensions the maximal number of considered supercharges is limited to $\mathcal{N} = 8$ [46]. For the case with only one supercharge, i.e. $\mathcal{N} = 1$, the relevant operators are the 1/2 Weyl spinor Q_α and their chiral conjugates $Q^\dagger_{\dot\alpha}$ with $\alpha, \dot\alpha \in \{1, 2\}$. The algebra of SUSY with respect to the spacetime translation operators, P_μ, and Lorentz generator, $M^{\mu\nu}$ can be summarized as:

$$\{Q_\alpha, Q^\dagger_{\dot\beta}\} = 2P_\mu \sigma^\mu_{\alpha\dot\beta}\,, \tag{2.37}$$

$$\{Q_\alpha, Q_\beta\} = \{Q^\dagger_{\dot\alpha}, Q^\dagger_{\dot\beta}\} = 0\,, \tag{2.38}$$

$$[Q_\alpha, M^{\mu\nu}] = (\sigma^{\mu\nu})^\beta_\alpha Q_\beta. \tag{2.39}$$

For the case of $\mathcal{N} > 1$, these relationships become more complicated and these cases are not considered in this document. According to the CM theorem, the internal symmetry generators, such as electric, weak isospin, and color charges, commute with the spacetime generators which now also include the supercharge generators as well. This implies that particles related to each other by a supercharge transformation (superpartners), have identical electric charges, weak isospin, and color charges. In the case of an unbroken SUSY, this identity would have applied to the mass of superpartners as well [3]. The supercharge transformations can be used to organize the SUSY and SM particles into supermultiplets containing the same number of bosonic and fermionic degrees of freedom. The new SUSY particles are discussed in the next section in the context of the Minimal Supersymmetric Standard Model (MSSM).

2.2.1 Minimal Supersymmetric Extension of the Standard Model

The MSSM is a supersymmetric extension of the SM with the minimum number of new particles and matter fields which already more than doubles the number of available degrees of freedom in the SM. The supersymmetric partners (*superpartners*) of SM fermions are often named by adding an "s" in front of the name of their SM partner. For example, stop and sbottom are superpartners of the top and bottom quarks and are also referred to as top and bottom squarks. In this document the symbols for the supersymmetric particles (*sparticles*) are denoted with the same symbol as their SM partner with the addition of a tilde on top. The superpartners of the left- and right-handed SM fermions, are referred to as sfermions,

[3] It is fair to say that the case for unbroken SUSY is closed since such SUSY particles would have been long observed. Therefore if SUSY is a symmetry of nature it can only be a broken one.

and denoted by $\widetilde{\mathrm{f}}_{\mathrm{L}}$, $\widetilde{\mathrm{f}}_{\mathrm{R}}$, respectively. The sfermions are scalars and therefore the "L" and "R" notation is only to indicate the chirality of their corresponding SM partner. Superpartners of bosons are referred to by their SM partner with the addition of "ino" at the end. For example, higgsino ($\widetilde{H}$) is the superpartner of the Higgs boson and superpartners of gauge bosons are referred to collectively as gauginos. In order for the MSSM to be anomaly free, the complex scalar corresponding to the SM Higgs field has to be replaced with two doublet fields,H_u and H_d which are responsible for providing mass to the up-type and down-type particles. The new particles introduced by MSSM are summarized in Tab. 2.4. The SM particles and their superpartners have identical Yukawa couplings and quantum numbers except for their spin which differs by 1/2. As mentioned earlier, in unbroken SUSY, the particles and sparticles would have a common mass, however from experimental observations we know this cannot be the case. The details of the mechanism responsible for breaking SUSY would then determine the mass spectrum of SUSY particles. Although there is no general consensus on how this mechanism should look like, theoretical and experimental constraints require that a viable SUSY breaking model should include a sector in which the breaking SUSY scale is much larger than the electroweak scale (soft breaking) and the breaking is communicated to the observable MSSM sector through an additional messenger sector. Two main types of messenger mechanisms are typically investigated: gravity mediation, in which the MSSM and the broken SUSY sectors interact only gravitationally, and the gauge mediation, in which the messenger sector is charged under the SM gauge groups. In order to parameterize our ignorance of the so-called soft SUSY breaking mechanism, we can express the MSSM Lagrangian as:

$$\mathcal{L}_{\mathrm{MSSM}} = \mathcal{L}_{\mathrm{SUSY}} + \mathcal{L}_{\mathrm{soft}}, \tag{2.40}$$

where $\mathcal{L}_{\mathrm{SUSY}}$ contains the unbroken SUSY Lagrangian and $\mathcal{L}_{\mathrm{soft}}$ includes the breaking terms which have been mediated to the MSSM sector. Similar to the way that the gauge bosons in SM mix with the goldstone bosons after electroweak breaking, the gauginos and higgsinos can also mix together as the result of SUSY breaking. The neutral gauginos ($\widetilde{B}$ and $\widetilde{W^0}$) and the neutral higgsinos ($\widetilde{H}_u^0$ and $\widetilde{H}_d^0$) can mix to form four neutral mass eigenstates referred to as neutralinos, $\widetilde{\chi}_i^0$ with $i = 1, 2, 3, 4$. Similarly, the charged gauginos ($\widetilde{W^+}$ and $\widetilde{W^-}$) and the charged higgsinos ($\widetilde{H}_u^+$ and $\widetilde{H}_d^-$) can mix to form four charged mass eigenstates referred to as charginos, $\widetilde{\chi}_i^\pm$ with $i = 1, 2$. In both cases, the indices i are set in ascending mass order so that $i = 1$ refers to the lightest neutralino or chargino. The breaking of SUSY also introduces the new massless Nambu-Goldstone particle, which is referred to as goldstino. A theory with a local SUSY would naturally unify spacetime symmetries of general relativity with the local supersymmetric transformations and is therefore also referred to as supergravity. Such a model would also include a gravitino as the superpartner of the hypothesized mediator for the

Names	spin-0	spin-$\frac{1}{2}$	$SU(3)_C$, $SU(2)_L$, $U(1)_Y$
squarks, quarks	$(\widetilde{u}_L \quad \widetilde{d}_L)$	$(u_L \quad d_L)$	$(\mathbf{3}, \mathbf{2}, \frac{1}{6})$
(×3 families)	$\widetilde{u}^*_R$	$u^\dagger_R$	$(\overline{\mathbf{3}}, \mathbf{1}, -\frac{2}{3})$
	$\widetilde{d}^*_R$	$d^\dagger_R$	$(\overline{\mathbf{3}}, \mathbf{1}, \frac{1}{3})$
sleptons, leptons	$(\widetilde{\nu} \quad \widetilde{\ell}_L)$	$(\nu \quad \ell_L)$	$(\mathbf{1}, \mathbf{2}, -\frac{1}{2})$
(×3 families)	$\widetilde{\ell}^*_R$	$\ell^\dagger_R$	$(\mathbf{1}, \mathbf{1}, 1)$
Higgs, higgsinos	$(H^+_u \quad H^0_u)$	$(\widetilde{H}^+_u \quad \widetilde{H}^0_u)$	$(\mathbf{1}, \mathbf{2}, +\frac{1}{2})$
	$(H^0_d \quad H^-_d)$	$(\widetilde{H}^0_d \quad \widetilde{H}^-_d)$	$(\mathbf{1}, \mathbf{2}, -\frac{1}{2})$

Table 2.2: The chiral supermultiplets introduced by MSSM. The spin-0 fields are complex scalar fields and include the sfermions and the MSSM Higgs doublets. The spin-$\frac{1}{2}$ fields are left-handed Weyl fermions of SM and the higgsinos [47].

Names	spin-$\frac{1}{2}$	spin-1	$SU(3)_C$, $SU(2)_L$, $U(1)_Y$
gluino, gluon	$\widetilde{g}$	g	$(\mathbf{8}, \mathbf{1}, 0)$
winos, W bosons	$\widetilde{W}^\pm \quad \widetilde{W}^0$	$W^\pm \quad W^0$	$(\mathbf{1}, \mathbf{3}, 0)$
bino, B boson	$\widetilde{B}^0$	B^0	$(\mathbf{1}, \mathbf{1}, 0)$

Table 2.3: Gauge supermultiplets of MSSM: the spin-$\frac{1}{2}$ MSSM gauginos and spin-1 SM gauge bosons [47].

gravitational force, the graviton. The breaking of local SUSY would result in the gravitino absorbing the goldstino as its longitudinal degrees of freedom and therefore become massive.

Of the most attractive features of SUSY has been its ability to offer solutions to multiple problems in SM. Supersymmetric theories can offer new particle which may be viable dark matter candidates and can also provide mechanism for natural cancellation of divergent corrections which are the source of the electroweak hierarchy problem. These features of SM are discussed in the next sections.

2.2.2 Natural SUSY and the hierarchy problem

Natural SUSY is a term used to refer to SUSY scenarios which offer a solution to the electroweak hierarchy problem (as briefly discussed in Sec. 2.1) or at least can significantly reduce the necessary amount of fine-tuning. The necessity of fine-tuning is due to the fact that the quantum corrections to the mass of the Higgs bosons at loop level receive contributions from three quadratically divergent sources, namely self interactions, gauge loops and fermion loops (particularly the top and bottom quarks), represented diagrammatically in Fig. 2.3.

Assuming a cut-off scale Λ_{UV} at which new physics becomes non-negligible, the dominant

Names	Spin	P_R	Gauge Eigenstates	Mass Eigenstates
Higgs bosons	0	$+1$	$H_u^0\ H_d^0\ H_u^+\ H_d^-$	$h^0\ H^0\ A^0\ H^\pm$
squarks	0	-1	$\widetilde{u}_L\ \widetilde{u}_R\ \widetilde{d}_L\ \widetilde{d}_R$ $\widetilde{s}_L\ \widetilde{s}_R\ \widetilde{c}_L\ \widetilde{c}_R$ $\widetilde{t}_L\ \widetilde{t}_R\ \widetilde{b}_L\ \widetilde{b}_R$	(same) (same) $\widetilde{t}_1\ \widetilde{t}_2\ \widetilde{b}_1\ \widetilde{b}_2$
sleptons	0	-1	$\widetilde{e}_L\ \widetilde{e}_R\ \widetilde{\nu}_e$ $\widetilde{\mu}_L\ \widetilde{\mu}_R\ \widetilde{\nu}_\mu$ $\widetilde{\tau}_L\ \widetilde{\tau}_R\ \widetilde{\nu}_\tau$	(same) (same) $\widetilde{\tau}_1\ \widetilde{\tau}_2\ \widetilde{\nu}_\tau$
neutralinos	1/2	-1	$\widetilde{B}^0\ \widetilde{W}^0\ \widetilde{H}_u^0\ \widetilde{H}_d^0$	$\widetilde{\chi}_1^0\ \widetilde{\chi}_2^0\ \widetilde{\chi}_3^0\ \widetilde{\chi}_4^0$
charginos	1/2	-1	$\widetilde{W}^\pm\ \widetilde{H}_u^+\ \widetilde{H}_d^-$	$\widetilde{\chi}_1^\pm\ \widetilde{\chi}_2^\pm$
gluino	1/2	-1	$\widetilde{g}$	(same)
goldstino (gravitino)	1/2 (3/2)	-1	$\widetilde{G}$	(same)

Table 2.4: The new particles introduced by MSSM, including the particles in the SUSY sector, indicated by their negative R-parity, $P_R = -1$ (see Sec. 2.2.3), and the new Higgs doublets in the SM sector, indicated by positive R-parity, $P_R = 1$. The sfermion mixing for the first two families are assumed to be negligible due to the small masses of their SM partners [47].

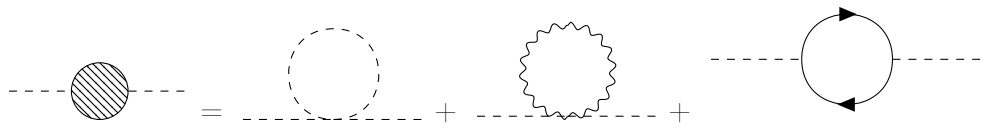

Figure 2.3: Diagrams contributing to the corrections of the Higgs mass.

correction to the Higgs mass comes from the contribution due to top quark:

$$\delta m_H^2|_t = -\frac{3y_t^2}{8\pi^2}\Lambda_{\rm UV}^2, \tag{2.41}$$

Where y_t is the top Yukawa coupling and has a value $y_t = 0.94$ and δm_H is the correction to the bare Higgs, $m_H^{\rm bare}$, giving the observed Higgs mass, m_H, i.e:

$$m_H = m_H^{\rm bare} + \delta m_H. \tag{2.42}$$

Then from Eq. 2.41, one would expect that the natural mass for the Higgs boson would be similar to the cut-off scale $\Lambda_{\rm UV}$. However, $\Lambda_{\rm UV}$ is typically expected to be close to the Planck mass or GUT scale, which would create a stark contradiction between the natural mass for the Higgs boson and its observed mass of $m_H \approx 125\,\text{GeV}$. In this case, we would be left

with a very unnatural solution of extreme fine-tuning of the bare mass in order to obtain the observed Higgs mass.

A much more satisfying answer can be offered in supersymmetric theories. In an unbroken SUSY the leading order loop diagram contribution of the top squark to δm_H can be calculated as:

$$\delta m_H^2|_{\tilde{t}} = \frac{3y_t^2}{8\pi^2}\Lambda_{\mathrm{UV}}^2, \tag{2.43}$$

which is equal to Eq. 2.41 up to a crucial sign difference which results in the total cancellation of the top and top squark corrections to the Higgs mass. A more in depth study can also show that these corrections in fact cancel for all orders in unbroken SUSY. On the other hand, we know that SUSY can only be a broken symmetry of nature, the top squark must have different Yukawa coupling than the top quark. This implies that for SUSY to be able to at least reduce the required amount fine-tuning, supersymmetric particles, and in particular the top squark should not be too heavy in order for the cancellation between fermionic and bosonic contributions to the Higgs mass to occur naturally [48–50].

2.2.3 R-Parity and dark matter candidates

There are a large number of Lorentz-invariant terms which can be added to the MSSM Lagrangian without violating any of the symmetries of the theory. However, many of these terms may violate lepton or baryon flavor numbers which would lead to an unrealistically short lifetime for the proton. The decay of the proton may be forbidden if an additional symmetry is imposed. One such symmetry is the so-called R-parity, P_R, and is defined by:

$$P_R \equiv (-1)^{3(B-L)+2S} = \begin{cases} +1 \text{ for SM particles} \\ -1 \text{ for SUSY particles} \end{cases}, \tag{2.44}$$

where B, L and S are the baryon number, the lepton number and the spin of the particle, respectively. R-parity is a discrete multiplicative symmetry and if conserved it would result in the following consequences:

1. No lepton and baryon violating interactions are allowed.

2. SUSY particles would always have to be produced in pairs. More generally, there must always be an even number of SUSY particles associated to each interaction vertex.

3. The lightest supersymmetric particle (LSP) is stable, since in order to conserve R-parity it would have to decay into another SUSY particle. Such a decay would be kinematically

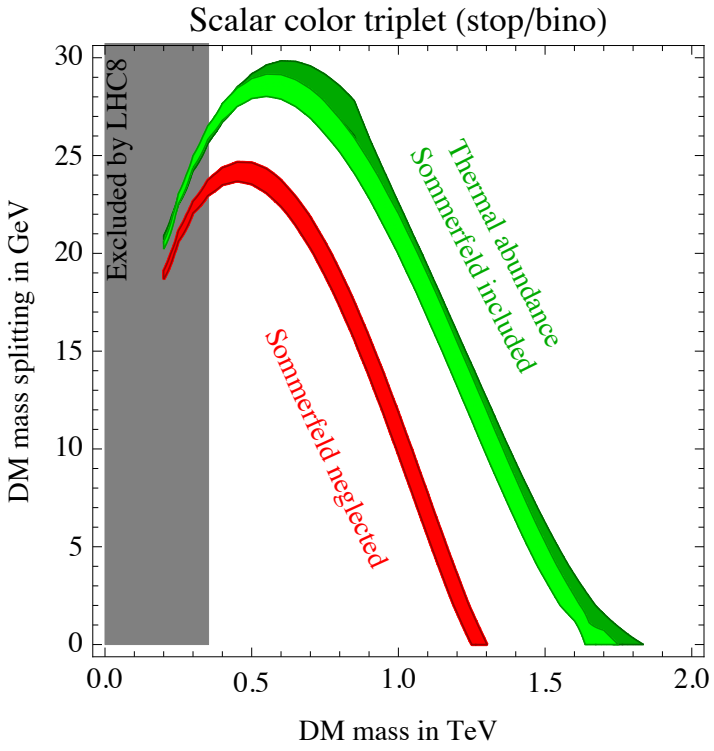

Figure 2.4: The green band indicates the SUSY mass configurations for the top squark and the LSP which can reproduce the observed dark matter relic densities [51].

forbidden since by definition there are no lighter SUSY particles.

A stable massive particle with an electric or color charge would have very distinct cosmological and possibly terrestrial signatures and since no such particles have been observed, it is often assumed that the LSP is a neutral particle. These properties make such a weakly interacting massive LSP a very suitable dark matter candidate. For this reason, in the rest of this thesis the lightest neutralino is assumed to be the LSP. In many SUSY models the calculated relic density from the LSP can be much larger than the observed values from the cosmological measurements. On the other hand, the correct dark matter relic density can be obtained in supersymmetric models with suitable parameters such as a nearly degenerate top squark and a neutralino as the LSP [51]. The small mass gap between the top squark and the LSP allows for the co-annihilation between the two particles which can result in the correct prediction for the dark relic density as shown in Fig. 2.4.

2.2.4 Unification of gauge couplings

Another attractive feature of many SUSY scenarios is that they allow for the convergence of the gauge coupling strengths at the GUT scale. Within the context of SM, the renormalization

group evolution of gauge couplings do approach each other at large scales but fail to unify at a single energy scale as seen in Fig. 2.5.

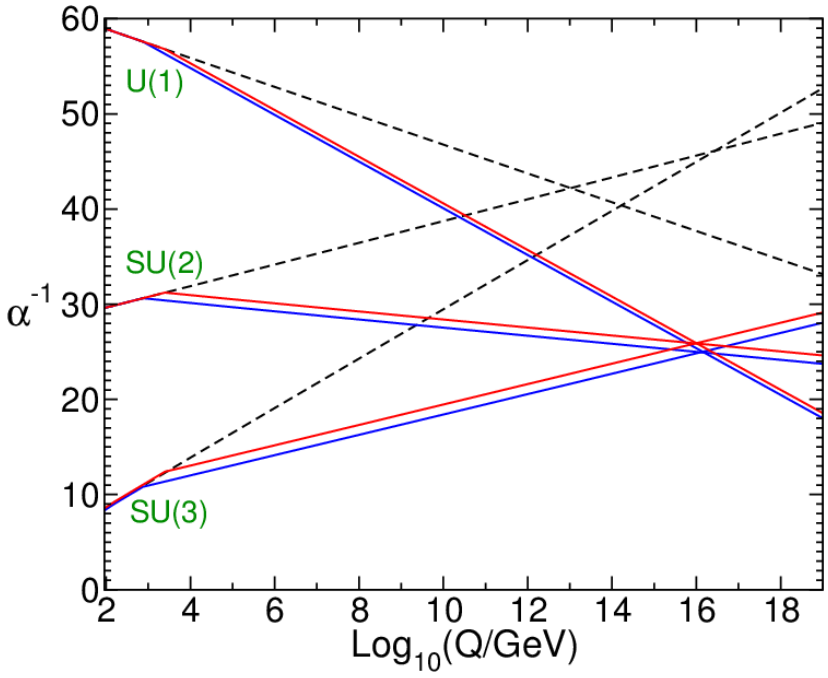

Figure 2.5: Evolution of the inverse of the three coupling constants of the SM within the context of SM and MSSM [47].

2.2.5 The case for light top squarks

As described in Sec. 2.2, for every bosonic (fermionic) degree of freedom in SM, a new fermionic (bosonic) one is introduced by SUSY. The MSSM in particular, predicts new scalar partners, $\tilde{f}_L$ and $\tilde{f}_R$, for each of the left- and right-handed fermions in the SM. The mixings of these eigenstates form the mass eigenstates, with the lighter and heavier states labeled as $\tilde{f}_1$ and $\tilde{f}_2$, respectively. The mixing matrices of the squarks have non-diagonal terms which are proportional to the mass of their SM partner. Therefore, the mixing between the superpartners of light quarks can be negligible, since the superpartners must have masses which are much heavier compared to their SM counterparts. On the other hand, the superpartners of top and bottom quark and the tau lepton can mix and result in mass eigenstates with large mass differences between the $\tilde{f}_1$ and $\tilde{f}_2$. Particularly, the large mass of the top quark may result in the mass difference between the top quark superpartners to be very large and for the $\tilde{t}_1$ to be much lighter than $\tilde{t}_2$. This large mass hierarchy may then result in $\tilde{t}_1$ to be the lightest squark making the search for the production of $\tilde{t}_1$ very well-motivated.

In order to investigate the available decay channels for the top squark, an important

quantity to consider is the mass difference, Δm, between the stop and the LSP:

$$\Delta m = m_{\tilde{\mathrm{t}}} - m_{\tilde{\chi}_1^0} \tag{2.45}$$

For instance, for $\Delta m > m_t$ the stop could decay into the onshell top quark and the $\tilde{\chi}_1^0$, i.e, $\tilde{\mathrm{t}} \to t\tilde{\chi}_1^0$. For values of $m_W < \Delta m < m_t$ the top in the decay chain would be offshell, resulting in a three-body decay of the stop: $\tilde{\mathrm{t}} \to bW\tilde{\chi}_1^0$. For regions with even smaller mass gaps, $\Delta m < m_W$, both top quark and W in the decay chain would have to be offshell which would result in a four body decay:

$$\tilde{\mathrm{t}} \to bff'\tilde{\chi}_1^0 \tag{2.46}$$

This region of parameter space, referred to compressed region, is highly motivated by cosmological constraints on the dark matter abundance, as described in Sec. 2.2.3. Assuming much larger masses for all other sparticles, in this compressed region, another possible decay channel for the top squark is the flavor changing neutral current (FCNC) decay, $\tilde{\mathrm{t}} \to c\tilde{\chi}_1^0$. Within the context of MSSM, FCNC couplings are allowed and depending on the details of the model the decay to the charm quark can become important. An example of such a scenario is depicted in Fig. 2.6 where FCNC mode is shown to dominate in cases with very small Δm, e.g, $\Delta m \lesssim 10$ GeV, while for $15 \lesssim \Delta m < m_w$ the four-body decay becomes the dominant decay mode. The search presented in this work focuses on final states with a single lepton and therefore only targets the top squark decay channels with a four-body final state. The four-body final state shown in Eq. 2.46 can have various contributing diagrams depending on the masses of other SUSY particles. If the top squark is the NLSP, then the stop would decay directly into the four-body final state. However, if the mass of the lightest chargino, $\widetilde{\chi}_1^{\pm}$, is between the stop and the LSP mass, the top squark could decay into the chargino and a b quark, followed by a three-body decay of the chargino into a fermion pair and the $\tilde{\chi}_1^0$, i.e: $\tilde{\mathrm{t}} \to b\widetilde{\chi}_1^{\pm} \to bff'\tilde{\chi}_1^0$. The decay chains for the direct-decay and the chargino-mediated decays of the top squark are shown in Fig. 2.7.

The main focus of this work is the search for the four-body and chargino-mediated decays of the top squark in the single lepton channel. The conservation of R-parity implies that the top squarks would be pair-produced. At the LHC the stop pair production at the leading order by quark-antiquark annihilation and gluon-gluon fusion with the partonic cross sections

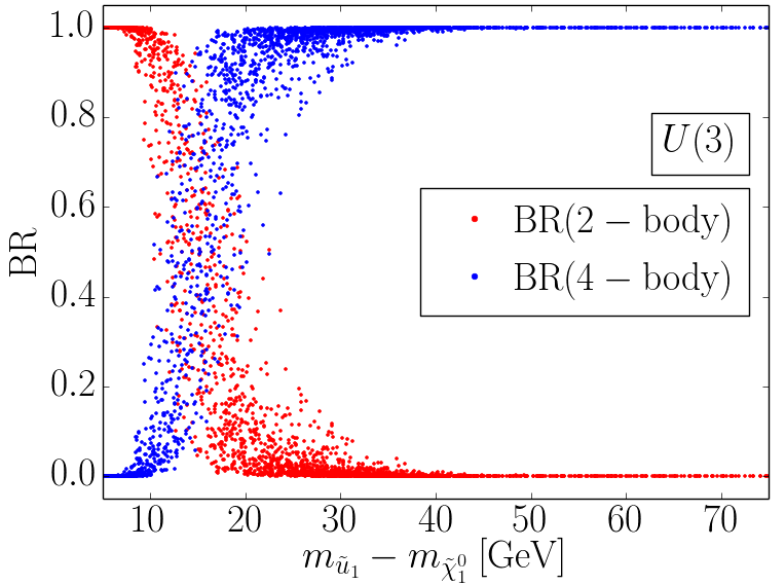

Figure 2.6: Branching ratios for the four-body (blue) and the FCNC (red) decays of the top squark corresponding to a specific flavor symmetry in the squark sector [52].

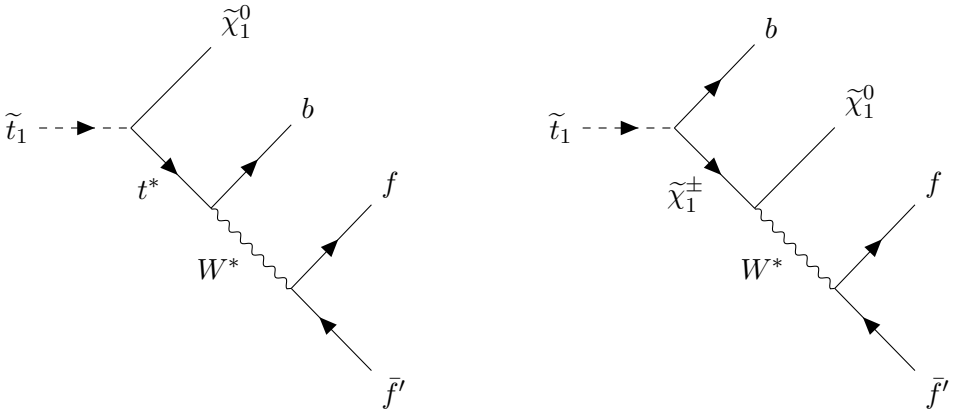

Figure 2.7: The four-body (left) and the chargino-mediated (right) decays of the stop.

given by [53]:

$$\sigma_{LO}(q\bar{q} \to \tilde{t}\bar{\tilde{t}}) = \frac{\alpha_s^2 \pi}{s} \frac{2}{27} \beta^3 \tag{2.47}$$

$$\sigma_{LO}(gg \to \tilde{t}\bar{\tilde{t}}) = \frac{\alpha_s^2 \pi}{s} \left[\beta \left(\frac{5}{48} + \frac{31 m_{\tilde{t}}^2}{24 s} \right) + \left(\frac{2 m_{\tilde{t}}^2}{3 s} + \frac{m_{\tilde{t}}^4}{6 s^2} \right) \log\left(\frac{1-\beta}{1+\beta} \right) \right] \tag{2.48}$$

Where s is the square of the invariant energy of the colliding partons, and $\beta_{\tilde{t}} = \sqrt{1 - 4m_{\tilde{t}}^2/s}$.

The total cross section, $\sigma(pp \to \tilde{t}\bar{\tilde{t}})$, can then be obtained by the convolution of the partonic cross sections with the parton density functions (PDFs). At the LHC the gluon-fusion is the dominating mechanism for the production of the stops. The relevant quark-antiquark and gluon-gluon diagrams are shown in the Fig. 2.8.

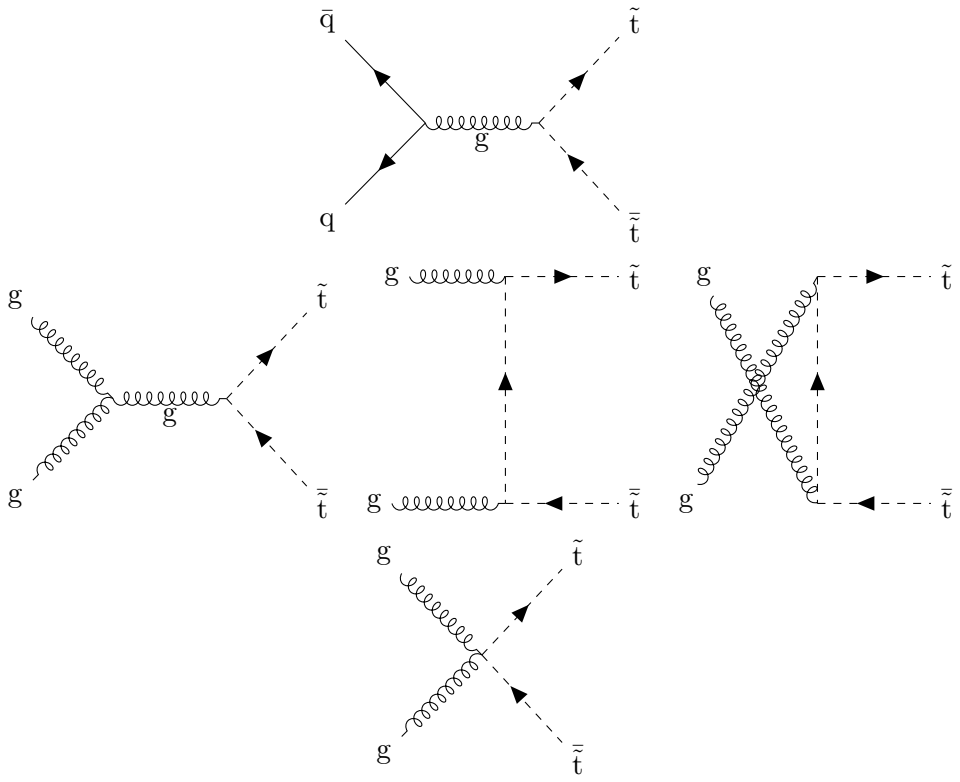

Figure 2.8: The quark-antiquark and gluon-gluon diagrams for the pair production of stops.

2.2.6 Simplified Models

The large number of new parameters introduced by SUSY can result in a wide spectrum of SUSY scenarios with different production and decay modes. This fact makes it very challenging and somewhat impractical for SUSY searches to be designed with sensitivity to large range of parameters in the full models. In order to reduce the model decadence of the SUSY searches, generic simplified topologies, referred to as Simplified Model Spectra (SMS) [17], are used which significantly reduce the number of parameters of interest for a given analyses. In these SMS, only a few new particles are considered and all other SUSY particles are then assumed to be decoupled, i.e. have large enough masses which do not affect production or decay modes of the lightest particles. The only relevant parameters in SMS are then the mass, cross sections and branching fractions of the light particles. Another advantage of performing searches within the context of SMS is that the model independence of these searches allows for

the reinterpretation of the results of the search in the context of any other BSM search with a similar final state as the SMS[4]. The branching ratios for the four-body and chargino-mediated SMS scenarios described in the previous chapter is assumed to be 100% for each of the models and the lifetime of the top squark is assumed to be zero. The calculated cross sections of the various SUSY production modes in the SMS scenarios [54] (including the pair production of the top squarks) and the cross sections for selected SM processes are shown in Fig. 2.9.

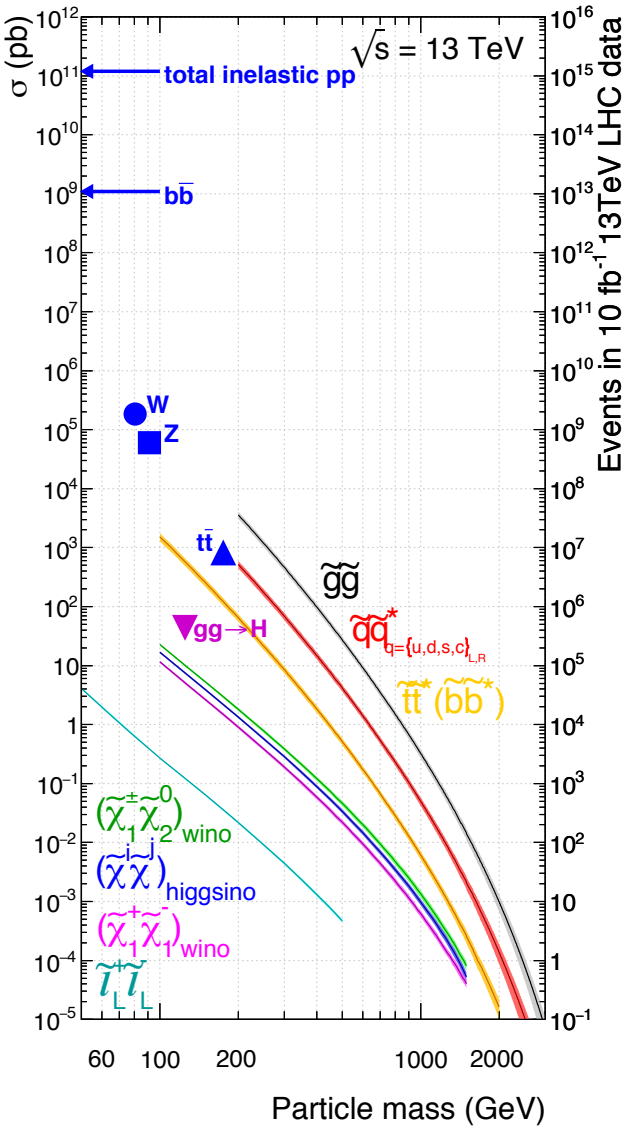

Figure 2.9: Cross sections for the production of standard model and SUSY particles at LHC pp collisions for a center-of-mass energy of 13 TeV are shown as a function of the particle mass [55]. The right vertical axis represents the expected number of produced events for an integrated luminosity of $10\,\mathrm{fb}^{-1}$.

[4]In order to facilitate the reinterpretation of the results of the analysis described in this thesis, additional information such as acceptance-times-efficiency maps of the signals and the covariance matrix of the background estimation are also provided. Examples of these material are shown in Appendix A.1.

The Large Hadron Collider and the Compact Muon Solenoid Experiment

3.1 The Large Hadron Collider

The Large Hadron Collider (LHC) is a circular apparatus designed to accelerate and collide proton beams at a center of a mass energy of 14 TeV [56]. The 26.7 km ring of the LHC, built and operated by the European Organization for Nuclear Research (CERN), lies 45-170 m underground and crosses the border of Switzerland and France. The LHC is housed in the preexisting tunnels of the Large Electron-Positron Collider (LEP) which stopped operation in the year 2000. In addition to proton-proton beams, for about one month per year the LHC is used to accelerate heavy-ion beams which are collided with either a proton beam or another heavy-ion beam.

3.1.1 The CERN Accelerator Complex

Before the protons are injected into the LHC they are accelerated to 450 GeV by the CERN accelerator complex shown in Fig. 3.1. The initial stage of this process is performed by the linear accelerator (LINAC2) which accelerates protons obtained from a hydrogen bottle to 50 MeV. Next, the protons are injected into the Proton Synchrotron Booster (PSB) in which they reach energies of 1.4 GeV before being injected into the Proton Synchrotron (PS). The four rings of PSB, each with a length equal to 1/4 of the PS circumference, sequentially fill the PS ring where the protons are accelerated to 26 GeV. The PS also separates the protons into bunches with a spacing of 25 ns before injecting the bunches into the Super Proton Synchrotron (SPS), the last stage of acceleration for the protons before entering the LHC. In the SPS the bunches are boosted to 450 GeV after which they are injected into the LHC. It takes 12 SPS cycles to fill the LHC which holds 2808 bunches. Currently the LHC is operating

at center-of-mass energy of 13 TeV. Each of the two oppositely-rotating beams of the LHC is currently accelerated to 6.5 TeV by 8 superconducting radiofrequency (RF) cavities oscillating at a frequency of 400 MHz. To ensure the functioning of the RF cavities, they are housed in cylindrical refrigerators and are kept at 4.5 K. The 25 ns bunch spacing of protons leads to a maximum bunch-crossing rate of 40 MHz.

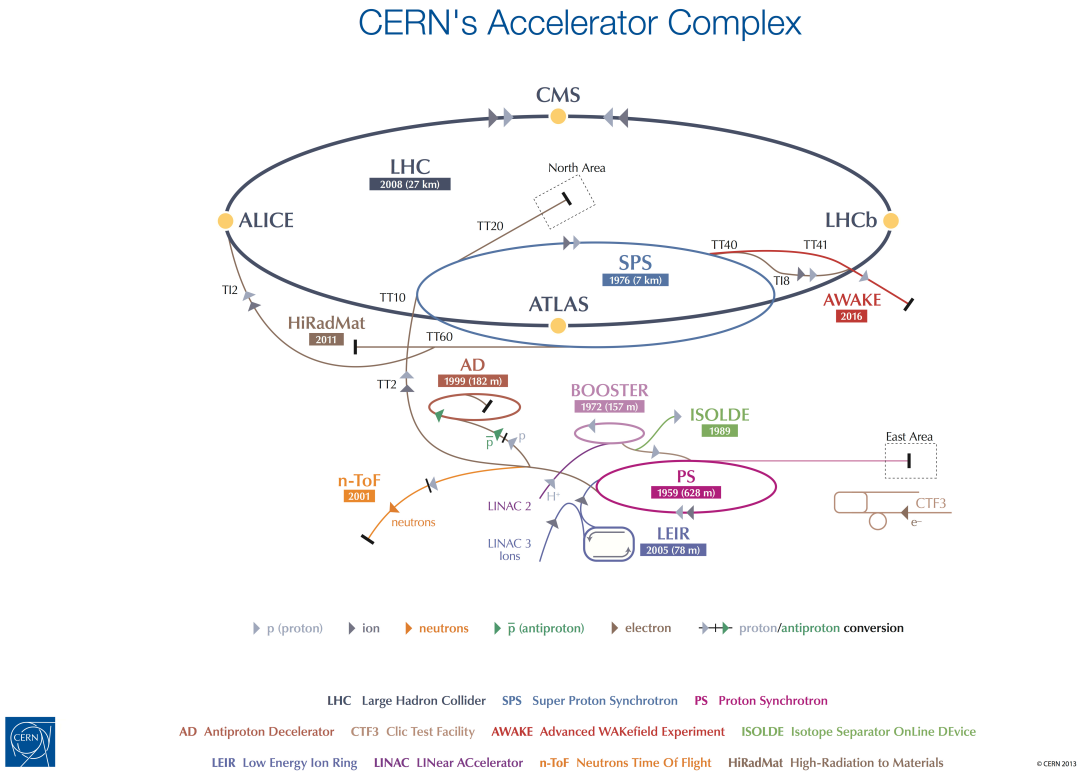

Figure 3.1: CERN accelerator complex [57].

3.1.2 LHC Parameters

In addition to the discovery of the Higgs boson, announced by the ATLAS and CMS Collaborations in 2012 [6,7,31], searching for physics beyond the standard model (BSM) has been one of the main goals of the physics program at the LHC. The physical processes which are being probed at the LHC are probabilistic in nature and therefore searches for BSM processes and precise measurements of already known physics processes are only feasible when statistically significant number of these processes can occur at the LHC. The expected number of events for a given process, N_{event}, is determined by the production cross-section of the process, $\sigma_{process}$, and the integrated luminosity registered by the experiment:

$$N_{event} = \sigma_{process} \int Ldt. \tag{3.1}$$

Searching for new physics typically involves looking for rare events with cross-sections much smaller than those of SM processes. Since the cross-section for an event is fixed by the underlying physics at the given energy scale, the luminosity of the experiment is a driving factor which determines the maximal statistical power of the searches and measurements performed within the experiment. The integrated luminosity can of course be increased by gathering data for longer and longer periods, however the ideal case is to increase the instantaneous luminosity, L. For a machine with n_b bunches per beam and N_b particles per bunch the instantaneous luminosity can be written as:

$$L = \gamma \frac{N_b^2 n_b f_r}{4\pi \epsilon_n \beta^*} F. \tag{3.2}$$

Here γ is the relativistic Lorentz factor, f_r is the revolution frequency, ϵ_n is the normalized transverse beam emittance which is a measure of the spread of beam in the momentum and position phase space, and β^* is the optical beta function at the collision point. The geometrical factor, F, depends on the length and size of the bunches and takes into account the reduction in the luminosity due to the crossing angle. Optimizing these factors in order to achieve the largest luminosity is the key challenge in designing an accelerator. The design peak luminosity for the ATLAS and CMS experiments is $L = 10^{34}\,\mathrm{cm}^{-2}\mathrm{s}^{-1}$. The integrated luminosities delivered by the LHC and recorded by the CMS detector during the 2016 data taking period are shown in Fig. 3.2.

3.1.3 The LHC Magnets

In order to keep the energetic proton beams circulating within the LHC ring, 1232 dipole magnets with a central field of 8.3 T are used. Additionally, around 850 quadrupole magnets are used for focusing the proton beams along the LHC arcs and near the interaction regions. Sextupole and octupole magnets are also used for additional fine tuning of the proton beam. The LHC magnets use a niobium-titanium (NbTi) superconductor technology and are cooled down to 1.9 K using superfluid helium in order to create the strong magnetic fields that are needed at the LHC.

Typically in particle-particle accelerators two completely separate rings have been used, since oppositely rotating beam of particles with the same charge require magnetic fields with opposite direction. However, the limited space of the existing LEP tunnels made this option impractical for the LHC and instead a twin-bore design for the magnets was proposed. In this

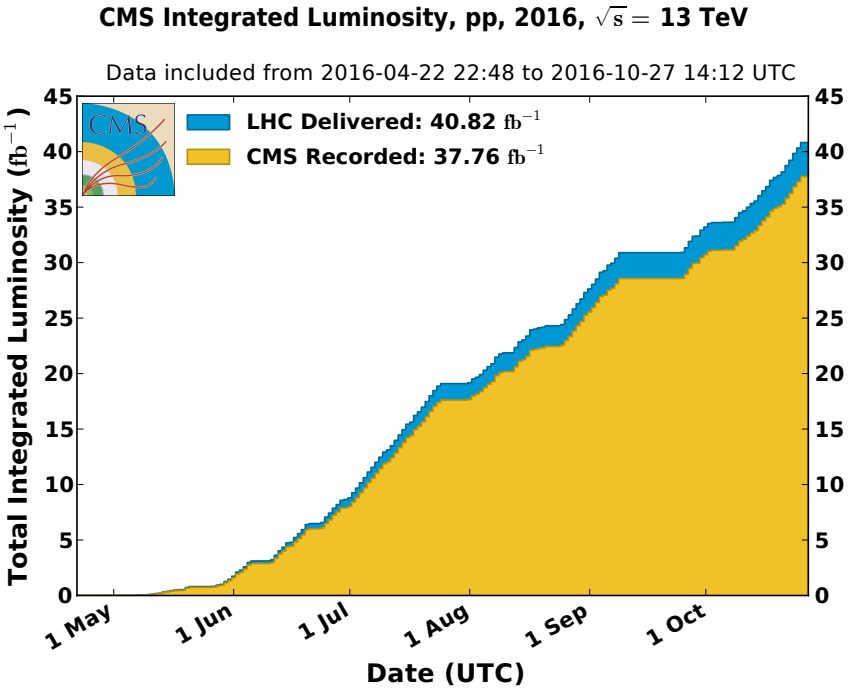

Figure 3.2: The measured integrated luminosity delivered by the LHC and recorded by CMS detector during the 2016 data taking [58].

"two-in-one" design the windings for the two beam channels are housed in a common cooling system. This space saving design comes of course with the complication that the two beam channels, particularly in the case of the dipoles, are coupled magnetically and mechanically due to the small separation of the two.

3.2 The Compact Muon Solenoid Detector

The CMS detector [60, 61] is a general-purpose experiment designed to take advantage of the full range of physics opportunities provided by the proton-proton and heavy-ion collisions of the LHC in order to precisely measure the properties of the SM and to search for physics beyond the SM. The wide range of geometric coverage of the detector which nearly covers the entire solid angle around the interaction region, allows for the products of the collision to be detected with high efficiency within the volume of the detector (15 m in diameter and 28.7 m in length). One of the key design features of CMS is the high resolution and efficiency in the identification of muons and capabilities of the detector for determining the transverse momentum and charge of the muons with transverse momenta of up to 1 TeV. The superconducting solenoid of CMS provides an impressive 3.8 T magnetic field which can bend the trajectory of charged particles, allowing for accurate measurement of their charge and mo-

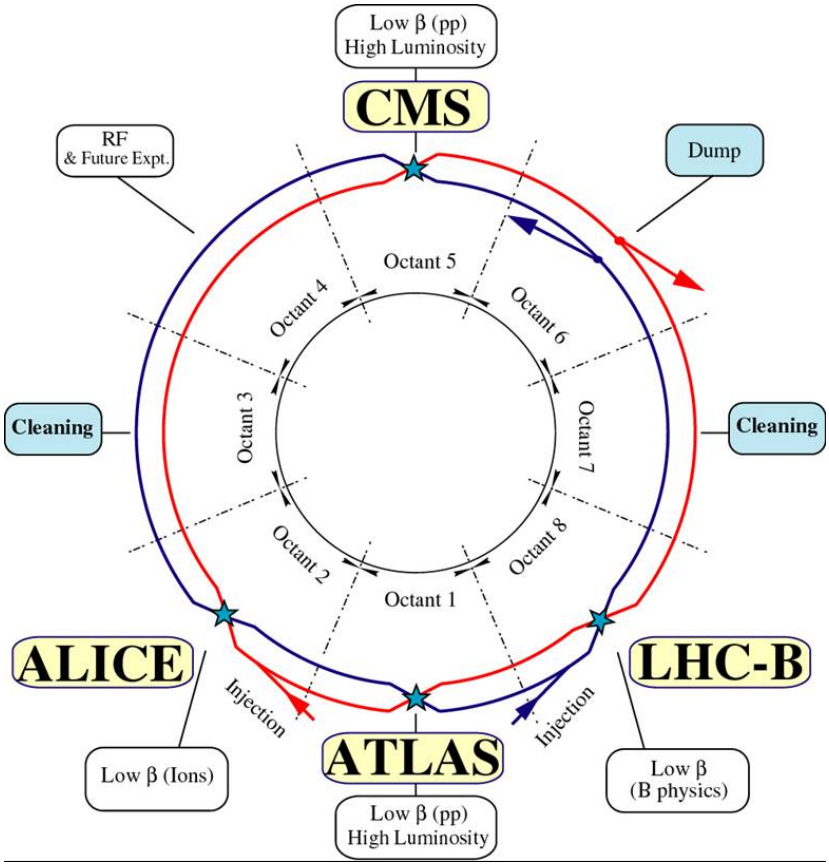

Figure 3.3: LHC schematic and the four main experiments located at the interaction region [59].

menta. The pixel and strip trackers are the innermost layers of the CMS detector and along with the electromagnetic and hadronic calorimeters are contained inside the magnet coil while the muon detectors are located outside the solenoid. A cross section of the CMS detector in the transverse plane, indicating the various sub-detectors is shown in Fig 3.4. In the rest of this section the main features of the various subsystems will be briefly discussed.

3.2.1 The CMS coordinate system

A Cartesian coordinate system with its origin at the nominal interaction point, the z-axis collinear along the beam and the x axis pointing radially toward the center of the LHC ring is chosen as the reference frame for the measurement of the physical quantities at the CMS detector. The y-axis is perpendicular to the x-z plane and points upward. The azimuthal angle, ϕ, is measured in the transverse x-y plane and with respect to the z-axis. The radial distance r and the polar angle θ are measured from the z-axis. Instead of θ a more useful

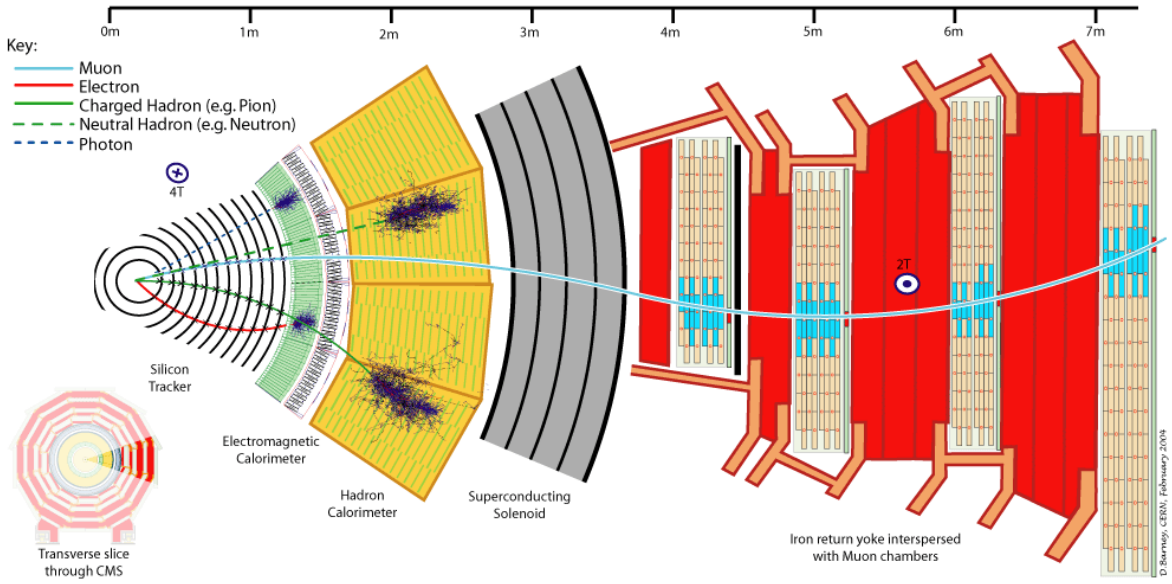

Figure 3.4: An illustration of a transverse slice of the CMS detector indicating various subsystems [62].

angular variable is the pseudorapidity which is defined as:

$$\eta = -\ln(\tan(\frac{\theta}{2})). \tag{3.3}$$

Pseudorapidity is a good approximation of the rapidity which is a Lorentz-invariant quantity defined by $y = \frac{1}{2}\log(\frac{E+p_z}{E-p_z})$, in terms of the energy of the particle, E, and the longitudinal component of its momentum, p_z. Another commonly used angular variable is ΔR which measures the distance between two particles in the η-ϕ plane and is defined by $\Delta R = \sqrt{\Delta\phi^2 + \Delta\eta^2}$.

Due to the complex partonic structure of hadrons, in proton-proton collisions the initial p_z of the colliding partons is not known. A more useful variable is then the transverse component of the momentum, $\vec{p}_{\mathrm{T}} = \vec{p}_{\mathrm{y}} + \vec{p}_{\mathrm{x}}$. The transverse momentum is particularly useful because it can be assumed that p_{T} of the incoming parton is close to zero. The conservation of momentum can then be used to quantify imbalances in the energies of the outgoing particles as discussed further in 4.6.

3.2.2 The Solenoid Magnet

The superconducting solenoid magnet of the CMS experiment has an internal diameter of 6 m and length of 12.5 m and designed to reach a magnetic field flux density of 4 T. A 10,000-tonne

iron yoke is used to contain the magnetic fields within the detector volume. The four-layer winding made from a stabilized reinforced NbTi conductor is embedded within an aluminum structure which provides the support to withstand the large mechanical deformations that may occur during the energizing of the magnet. It has been decided by the CMS collaboration to keep the operating magnetic field at 3.8 T in order to maximize the lifetime of the solenoid. A longitudinal section of CMS with the predicted magnetic flux densities [63] is shown in Fig. 3.5.

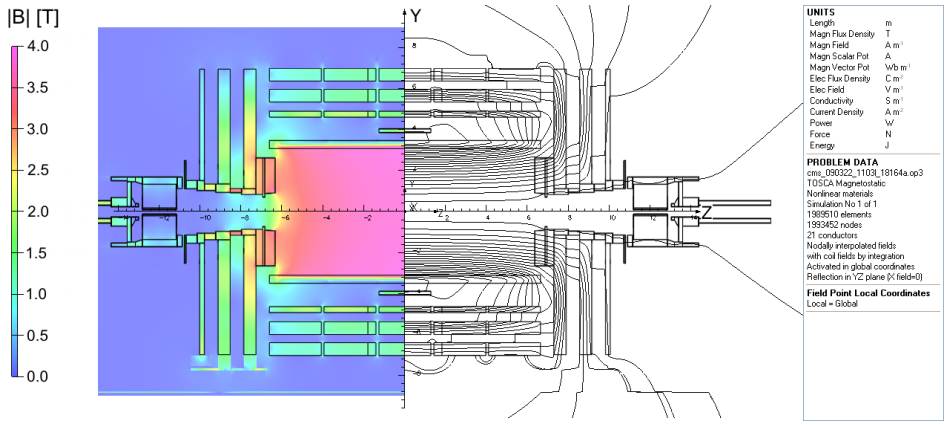

Figure 3.5: Predicted magnitude of the B-field and the field lines respectively shown on the left and the right of a longitudinal cross section of the CMS detector [63].

3.2.3 The Pixel and Strip Trackers

The CMS tracking system is the closest subdetector to the interaction point and has the task of measuring the trajectories of the charged particles emerging from the proton-proton collisions. The tracker also allows for precise measurement of secondary vertices arising from decay of heavy flavored hadrons which are produced in many physics channels. The full volume of the tracker which has a length of 5.8 m and a diameter of 2.5 m sits within the homogeneous magnetic field of 3.8 T and can provide tracking coverage for particles with $|\eta| < 2.5$. The challenging conditions created by the collisions at the LHC demand advanced technologies with high granularity and fast response in order to reliably measure the tracks and disentangle tracks from overlapping bunch crossings. The intense particle flux from the proton-proton interactions necessitates the use of radiation hard components in the detector, leading to the all-silicon design of the CMS tracker system with total active area of about 200 m^2. The tracker consists of two subsystems: the pixel tracker and the strip tracker.

The pixel detector covers a total area of 1 m^2 and consists of 66 million silicon pixels with dimensions 100 μm $\times$ 250 μm $\times$ 250 μm. It is composed of three cylindrical layers in the barrel region located at radii of 4.4, 7.3 and 10.2 cm from the beam-line and two disks in the forward

and backward regions each which extend the η coverage to 2.5. The pixel tracker can achieve a spatial resolution in the range of 10-15 μm in each direction, which is more than sufficient for track reconstruction and identification of primary and secondary vertices. However, over time the resolution can be degraded due to radiation damage. For this reason the CMS pixel detector was replaced and upgraded at the end of 2016 data taking.

The strip tracker encompassing the pixel detector consists of 10 barrel layers and 3 plus 9 disks on each side of the barrel as shown in Fig. 3.6. The barrel region consists of the Tracker Inner Barrel (TIB) and the Tracker Outer Barrel (TOB) which include 4 and 6 detection layers respectively. The TIB covers a distance of up to $|z| < 65\,\text{cm}$ from the interaction point, while the TOB extends up to $|z| < 110\,\text{cm}$. In the endcap region, the Tracker Inner Disks (TID) are made out of 3 disks and the Tracker End Cap (TEC) consists of 9 disks covering $120 < |z| < 280\,\text{cm}$. In the first two inner layers of each section and the fifth layer of the TEC a second detector module is mounted back-to-back with a stereo angle of 100 mrad. This double-layer setup provides measurements of the z and r directions in the barrel and the endcaps, respectively.

In total the strip tracker has 9.3 million silicon strips and has a designed resolution of 30 μm in (r, ϕ) and 300 μm in the z direction.

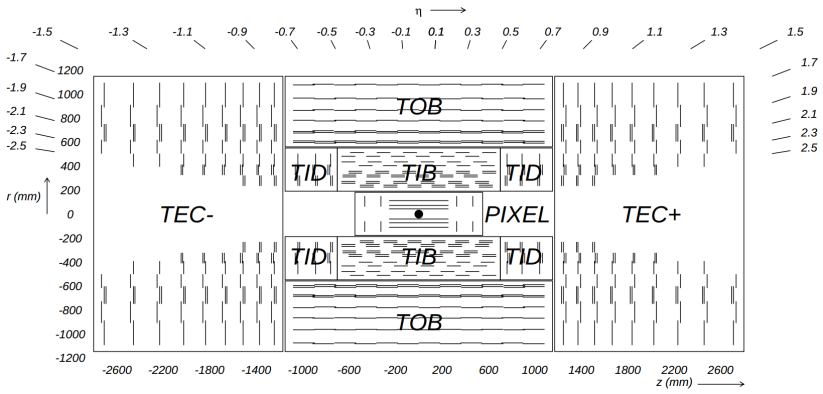

Figure 3.6: Schematic cross section of the CMS tracker displaying the pixel tracker (PIXEL) and different components of the silicon strip tracker (TIB, TOD, TEC, TID). The single and double lines represent the single and back-to-back detector modules, respectively [60].

3.2.4 The Electromagnetic Calorimeter

One of the important design goals of the CMS detector was the high precision measurements of the energy and position of photons and electrons by the electromagnetic calorimeter (ECAL) subdetector. In particular, capabilities to detect the di-photon final-state of the Higgs boson was one of the motivating factors in the design of the detector which in addition to high photon energy resolution also demands reliable separation of photons from neutral pions. The ECAL

is also essential for accurate measurement of jet energies since a non-negligible portion of the energy of jets is carried by photons.

The ECAL system at CMS, located outside the tracker, consists of 75848 lead tungstate ($PbWO_4$) crystals and is separated into barrel (EB) and two endcap (EE) sections. The high density, short radiation length, and small Molière radius of lead tungstate allow for the high granularity and compact size of the ECAL detector. The crystals have a radiation hardness of up to 10 Mrad and their short scintillation decay time allows for 80% of light to be emitted within 25 ns which makes them compatible with the bunch spacing at the LHC. The layout of the ECAL system is shown in Fig. 3.7.

As the energetic electrons and photons enter the ECAL, they begin a process known as *electromagnetic showering*, in which the bremsstrahlung of electrons and their pair-production by photons results in a cascade into lower energy electrons and photons. This process continues until the particle energies are below a critical energy at which point ionization becomes the dominant source of energy loss for the electrons. The ionized atoms in the $PbWO_4$ crystal then emit a blue-green scintillation light with a broad maximum frequency at 420-430 nm as they fall back into their lower energy state. This scintillation light is then captured by the photodetectors located at the outward facing end of the crystal. Due to different radiation exposures and different orientations in the magnetic field, silicon avalanche photodiodes and vacuum phototriodes were chosen as photodetectors in the barrel and endcap regions respectively.

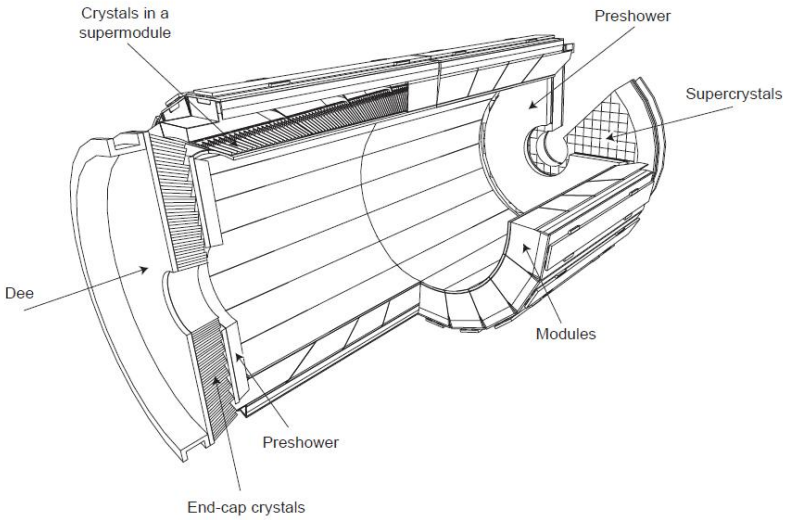

Figure 3.7: Layout of the CMS electromagnetic calorimeter [60]. The arrangement of the crystals, supermodules, endcap and the preshower are shown. The distance from the interaction point to the barrel and the endcaps is 1.29 m and 3.1 m respectively.

The EB covers a range of $|\eta| < 1.479$ and has an inner radius of 1.29 m. It consists of 61200 crystals with tapered shapes which vary slightly as a function of η. The crystals

are structured into 36 identical *supermodules* which surround the beam-line. In order to reduce gaps in geometrical acceptance and avoid cracks aligned with particle trajectories, the orientation of the modules is offset by a 3° angle (in both ϕ and η directions) with respect to the nominal interaction vertex. The crystals in the barrel have a front face cross section of $\approx 22 \times 22\,\mathrm{mm}^2$ and a length of 23 cm which corresponds to 25.8 radiation lengths (X_0) and allows for most of the energy of the electron or photon to be captured by a single crystal. The two EE disks are located 3.17 m away from the interaction point and cover the range $1.479 < |\eta| < 3.0$. The crystals in the EE have a front face cross section of $28.62 \times 28.62\,\mathrm{mm}^2$ and are 22 cm long.

In addition to the EE and EB, the electromagnetic calorimeter is equipped with the preshower detector (ES) which helps distinguish single photons from photon pairs produced in the decay of neutral pions. The ES is installed in front of the EE since the angle between photons emerging from the pion decay is likely to be smaller in the forward region. The high granularity of the ES detector also leads to an improved position measurement of the electrons and photons. The ES is a 20 cm thick ($3X_0$) sampling calorimeter with a first layer consisting of lead radiators which initiate the electromagnetic shower and the second layer made up of silicon strips which measure the energy depositions of the shower. The ES covers a pseudorapidity region of $1.653 < |\eta| < 2.6$.

A careful calibration of the CMS ECAL is necessary for achieving the optimal precision of the detector, both in terms of absolute value of measured energies and also the channel-to-channel relative effects. The calibration of the ECAL is performed both with the collision data and in laboratory using cosmic-rays and high energy electrons beams. The energy resolution for each 3×3 crystal setup was parameterized in terms of the energy, E, with a typical parameterization taking a form of [64]:

$$\left(\frac{\sigma}{E}\right)^2 = \left(\frac{2.8\%}{\sqrt{E}}\right)^2 + \left(\frac{12\%}{E}\right)^2 + \left(0.3\%\right)^2 \tag{3.4}$$

The first term parametrizes the stochastic contributions which include event-to-event fluctuations. The second term takes into account the contribution due to noise coming from sources such as the electronics, digitization and pileup. The constant term includes the non-uniformity of the longitudinal light collection in the crystals, channel-to-channel calibration errors and also the leakage of electromagnetic shower from the back of the crystals.

3.2.5 The Hadron Calorimeter

The outermost detector layer within the CMS magnet is the sampling hadron calorimeter (HCAL) designed to measure the energy and position of hadrons. The HCAL also extends the hermeticity of the detector to up to $|\eta| < 5$ which is essential for accurate measurements of the imbalance in missing transverse energy. Alternating layers of brass absorber and plastic scintillator materials are used in the HCAL. Brass was chosen as absorber as it is non-magnetic and has a short nuclear interaction length (16.24 cm). As the hadrons enter the absorber material, they interact strongly with the brass nuclei, resulting in a cascade of new particles referred to as *hadronic shower*. The particles in the shower eventually enter the plastic layer, where their energy is measured from the emitted light by the scintillator. The HCAL consists of about 70000 scintillating tiles and is divided into several subsystems in the different regions shown in Fig. 3.8: in the central region, the HCAL barrel (HB) and the HCAL outer (HO) and in the endcap region, the HCAL endcap (HE) and HCAL forward (HF).

The HB, located between ECAL and magnet coil ($1.77 < r < 2.95$m), is composed of 36 identical azimuthal wedges and provides coverage for the region $|\eta| < 1.3$. Each wedge has a weight of 26 tons and a transverse granularity of $\Delta\eta \times \Delta\phi = 0.087 \times 0.087°$. In order to provide enough structural support for the HB, the inner and outermost absorbers layers are made out of stainless steel. The thickness of the absorbers is 5.82 interaction lengths (λ_I) at $\eta = 0$ and increases to 10.6 λ_I at $|\eta| = 1.3$. The HO is located between the solenoid and the muon system in the region $|\eta| < 1.26$ and by collecting the energy that escapes the HB it increases the effective thickness and consequently the energy resolution of the HCAL. The solenoid acts as an additional absorber for the HO and allows it to identify late starting showers.

In order to extend the hermiticity of the detector in the forward region, the HF system is installed along the beampipe and 11.2 m away from the interaction point, covering the region with $3.0 < |\eta| < 5.0$. The hostile location of the HF exposes this subsystem to 7 times the energy deposition per collision as for the rest of the detector. Enduring these harsh conditions was a main driving force in the design of the HF leading to a sampling calorimeter design composed of 1.65 m thick steel absorbers and 0.6 mm radiation-hard quartz fibers as the active medium.

When charged particles entering the quartz travel at speeds faster than the speed of light in the medium, they emit Cherenkov light which is then captured by photomultiplier tubes. Therefore, the HF for the most part is only sensitive to the electromagnetic component of the showers. The HF has a granularity of 0.175 and 0.175° in the η and ϕ directions respectively. The single pion energy resolution for the scintillator based subsystems of the

HCAL is parameterized as [65]:

$$\left(\frac{\sigma}{E}\right)^2 = \left(\frac{94\%}{\sqrt{E}}\right)^2 + \left(8.4\%\right)^2 \tag{3.5}$$

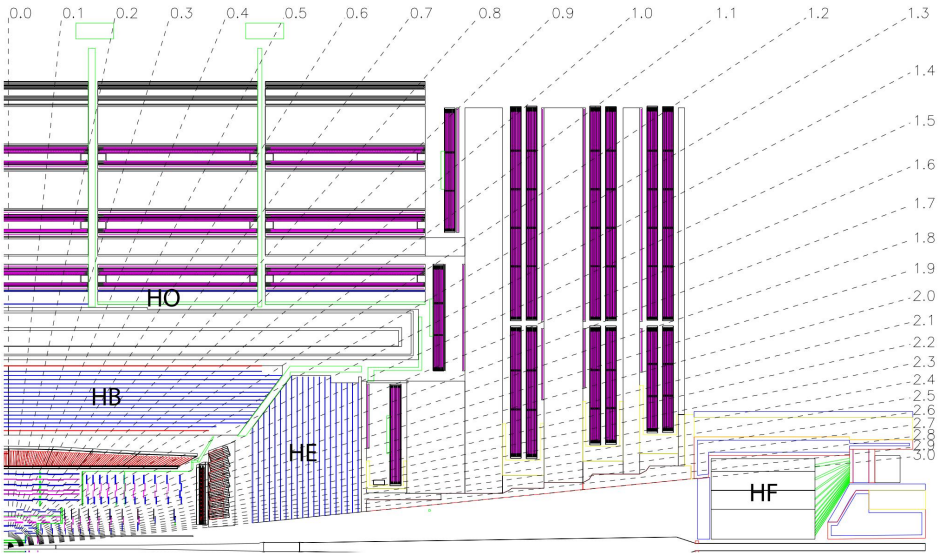

Figure 3.8: A longitudinal schematic of the CMS detector indicating the location of the hadronic barrel (HB), endcap (HE), outer (HO) and forward (HF) calorimeters. The numbers represent the value of η for a given black dashed line [60].

3.2.6 The Muon System

One of the main design goals of the CMS detector has been the effective identification and measurement of the muons. This was particularly motivated by one of the main discovery channels for the Higgs boson, $H \to ZZ^* \to \ell^+\ell^-\ell'^+\ell'^-$, where the final states including muons offered the best sensitivity [66, 67]. Muons also a critical rule in the analysis strategy used in this thesis which is on single-lepton final states with small transverse momenta. In addition to muon identification and momentum measurement, the muon system is also responsible for providing triggering capabilities for the detector. The high magnetic field and the flux-return yoke of the CMS allow for good momentum resolution and triggering of the muons over a very large kinematic range.

Due to their larger mass compared to electrons, muons experience smaller radiative losses in the tracker material and can also penetrate the calorimeters and the solenoid. As a consequence, the muon chambers are often located in the outermost regions of a detector, where other particles are much less likely to penetrate to. The thickness of various detector layers

crossed by muons is shown in Fig. 3.9. The muon system in CMS is a cylindrical detector with a barrel section and two endcap sections and uses three types of gaseous detectors: drift tubes (DTs), cathode strip chambers (CSCs) and resistive plate chambers (RPCs).

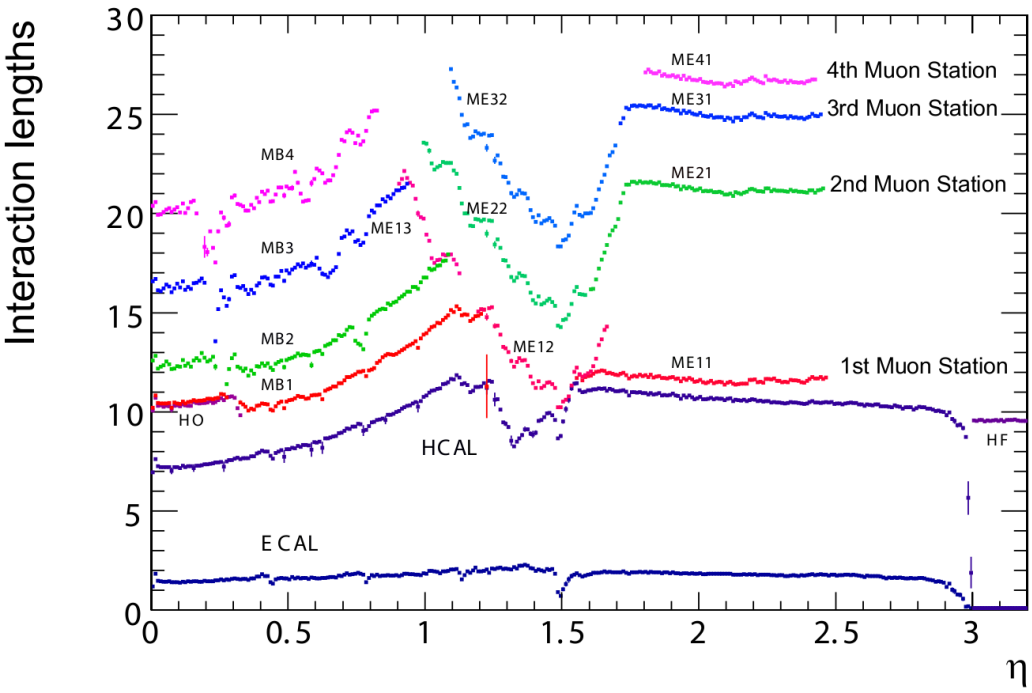

Figure 3.9: The thickness of material crossed by muons in units of interaction lengths and as a function of pseudorapidity, η [60].

The DTs are made of aluminum tubes filled at atmospheric pressure with an 85%-15% mixture of Ar/ CO_2. An anode wire is located in the center of the tube and collects the ionization energy. The DTs are utilized in the barrel region with $|\eta| < 1.2$ where the neutron-induced background and the muon rates are small and the magnetic field is uniform. They are organized into 4 stations with the first 3 stations divided into 2 groups of 4 chambers each, where one group measures the muon coordinate in the bending plane (r-ϕ plane) and the other group measures the z coordinate of the muon. The two groups are separated as much as possible in order to obtain the best angular resolution. The fourth station does not contain planes for z-measurement. In order to minimize the blind spots in the muon system, the DTs in each chamber are offset by a half-cell width with respect to their neighboring cells.

The two endcap regions of the muon system ($0.9 < |\eta| < 2.4$) are exposed to a large non-uniform magnetic field with high muon and background rates. In these regions, the CSCs were used by the muon system due to their fast response time and resistance to radiation. The chambers contain a 40%-50%-10% mixture of the $Ar/CO_2/CF_4$ gasses. The CSCs are organized into four stations in each endcap with the chambers running perpendicular to the beam-line and the cathode strips running radially outward from the beam-line in order to

provide a measurement in the bending plane. The anode wires run roughly perpendicular to the cathode strips and their read out provides measurement in the η direction and also the time of the beam-crossing for the muon. The CSCs include a total sensitive area of 5000 m^2, a gas volume of more than 50 m^3, and about 2 million wires. When a charged particle passes through the gas, the gas becomes ionized and as the free electrons move toward the anode, an electric signal is induced in the wire. The signal hit has a resolution of 100 μm and 10 mrad in the r and ϕ directions respectively. The RPC system of CMS provides extra coverage

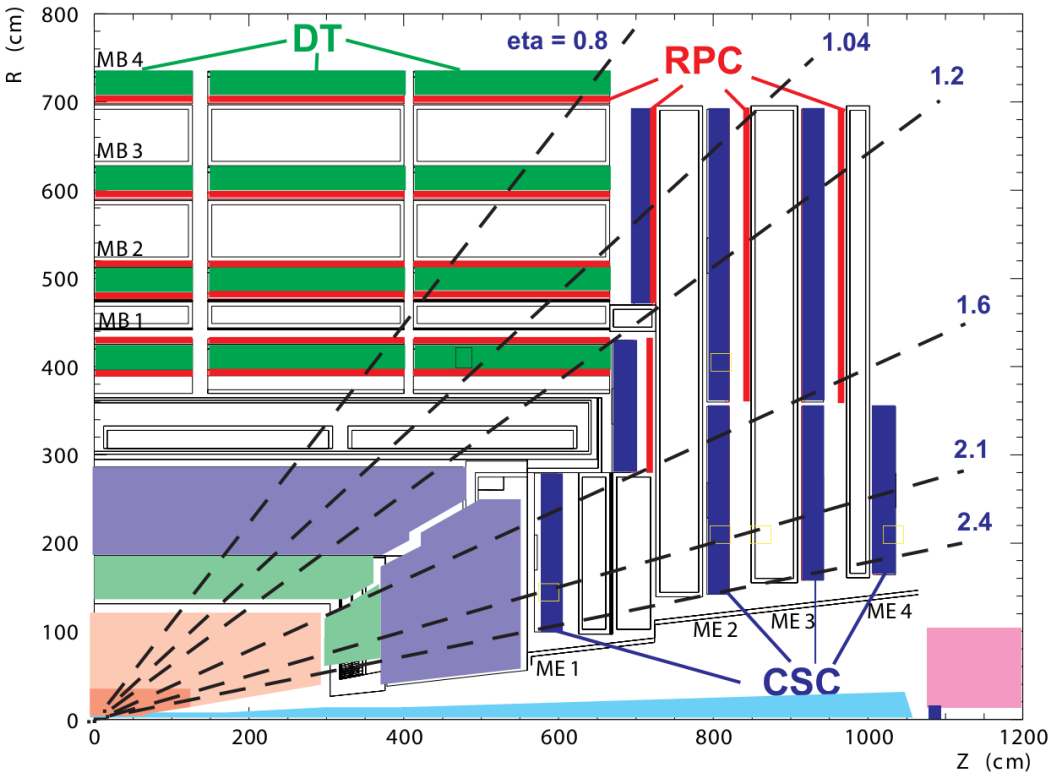

Figure 3.10: Schematic layout of a quarter of the CMS muon system with the beam-line running horizontally [68].

for the muon system in the pseudorapidity region $|\eta| < 1.6$. The RPCs have a low spatial resolution due to their large strip width but an excellent temporal resolution of about 1 ns which allows for unambiguous bunch crossing identification, essential for triggering on the muons. The RPCs consist of two oppositely charged parallel plates made with high resistance plastic material containing the volume filled gas mixture. In the barrel region, the six RPC layers are embedded in the muon system with some redundancy in the two inner stations in order to help with the efficient triggering of muons even with lower p_T. In the endcap region, three RPC layers are installed perpendicular to the beam which further improve the time and p_T resolution of the muons.

3.2.7 The CMS Trigger and Data Acquisition

The nominal bunch crossing of 25 ns (40 MHz) at the LHC corresponds to $\sim 10^9$ interactions per second for the design luminosity. Storing the collected data for each interaction would require more than 40 TB of storage per second which would not be feasible. A large majority of these events do not include a hard scattering interaction between the protons and are referred to as *minimum bias* events. Such events are not very likely to include interesting physics and can be discarded. The purpose of the two-tiered CMS trigger system is to reduce the number of events selected for storage to $\sim 10^2$ interactions/s. This goal is achieved in two steps, referred to as Level-1 Trigger (L1T) and High Level Trigger (HLT). For the decision making, L1T relies on highly programmable custom-designed electronics, and the HLT is implemented as a software system on a large computing farm. The L1T processes the raw information from the calorimeters and the muon systems in order to make a decision on whether to accept or reject an event for storage within 4 μs of collision. The limit for the output rate of the L1T must be kept below 100 kHz due to the front-end detector limitations and the restricted bandwidth and computing power in the HLT. Due to the limited time for processing the detector data, L1T uses reduced resolution and simple algorithms to process the incoming information on the custom hardware, namely field-programmable gate arrays and specific integrated circuits to construct the physics objects such as electrons, muons, jets, and missing transverse energy for the triggering decision. These trigger objects, referred to as trigger primitives (TPs) are generated based on the energy deposits in the calorimeters, and track segments or hit patterns in the muon chambers. Next the regional triggers combine this information to produce the trigger objects on which the final decision of the global trigger (GT) is based. The regional triggers also rank and sort the trigger objects based on the energy or momentum of the object and the quality of the reconstructed TPs. The ranked trigger objects are then evaluated by the Global Calorimeter and Muon Triggers and the ones with the highest rankings are passed on to the GT. These objects include the calculated missing transverse energy, the four highest ranked muon candidates and the best four isolated and non-isolated electrons and photons, jets and τ-like objects. The GT then uses a total of 128 programmable algorithms to make the triggering decision based on these trigger objects. All algorithms are evaluated and if any of them accept the event, then event is read out by the DAQ system and passed on to the HLT. The HLT can use more sophisticated algorithms, similar to those used in the offline analysis level to reconstruct the physics objects. The HLT has a processing delay time of about 100 ms and can reduce the rate of selected events for storage to less than 1 kHz.

Reconstruction of physics objects

The common software framework for the CMS experiment (CMSSW) is used to process the coarse output of various CMS detectors in order to reconstruct the physics objects such as jets, leptons, photons and missing transverse energy which are used for event selection at the analysis level. The performance of any physics analysis relies heavily on the efficiency and purity of the reconstructed physics objects. The traditional strategy for reconstructing these objects at hadron colliders has been to utilize mainly the information from the most relevant detector. For instance, jets can be reconstructed from calorimeter information without distinguishing the particles within the jet, ECAL can be used to reconstruct isolated photons and electrons, and muon detection can rely solely on the signals from the muon detector. However, the reconstruction of these objects can be significantly improved by taking a bottom-up approach and using the correlation between various subdetector signals in order to identify individual particles and then building up the physics objects from these identified particles.

This approach, referred to as the particle flow (PF) algorithm [69], was first developed by the ALEPH experiment, however CMS is the first experiment to take advantage of this method at a hadron collider. The fine granularity of the CMS subdetectors is one of the main features which allow for the identification of individual particles and therefore making it possible for the PF algorithm to provide a global description of the event. Another advantage of the PF method is that it allows for cross-calibration of different subdetectors and also to identify and mask detector backgrounds. Moreover, the PF algorithm has been implemented in the reconstruction of the objects at the HLT level.

The input *elements* of the PF algorithm are the trajectories of charged particles (tracks) from the tracker system and clusters of energy depositions from calorimeters. These PF elements and the reconstruction of physics objects by the PF algorithm are described in the rest of this chapter.

4.1 Tracks and clusters

Iterative tracking

The first step in reconstructing tracks is to cluster signals from the pixel and strip tracker subdetectors which pass the specified quality criteria into *hits*. The position and the uncertainty of the hits are given by the charged-weighted average of the strip positions, corrected for the Lorentz drift due to the magnetic field inside the tracker [70]. The tracker hits are then iteratively processed to reconstruct the tracks using an algorithm based on the Kalman filter which allows for pattern recognition and track fitting to occur within the same framework [71, 72].

In this *iterative tracking* strategy, the easiest tracks with tight selection criteria are found first. The hits associated with the found tracks are then removed which simplifies the next iteration in search for increasingly more difficult categories of tracks. A total of six iterations is performed where each iteration has the following four steps:

- **Seed generation**: provides the initial track candidate using 2-3 hits and includes the initial estimates of trajectory parameters and uncertainties.
- **Track finding**: a Kalman-filter based step which searches for additional hits by extrapolating the trajectory of the seed along the expected path of a charged particle in the magnetic field.
- **Track fitting**: provides the final estimation of the track parameters using a Kalman filter or Gaussian Sum Filter (GSF).
- **Track selection**: the reconstructed tracks that pass certain quality criteria are flagged and are discarded otherwise.

Calorimeter clusters

The energy deposits in the various calorimeter subsystems are clustered in order to detect and measure the energy and direction of stable neutral particles, separate the neutral particles from the charged hadrons, reconstruct and identify electrons including the radiated photons, and improve the energy measurement of charged hadrons for tracks with low quality or high-p_{T}. The clustering algorithm used at CMS was developed specifically with the PF algorithm in mind and is performed separately in each subdetector except for the HF where no clustering is needed. The initial seeds for the clustering are selected as cells passing a certain energy threshold. Neighbouring seeds with at least one common corner are aggregated together to form "basic clusters", representing local maxima of energy deposits. Then an expectation-maximization algorithm is used to reconstruct the clusters within these basic clusters [64].

The absolute energy scale of the 9 EB supermodules and 500 EE crystals was calibrated using high-energy electron beams prior to installation at CMS while the rest of the ECAL components were intercalibrated. The silicon modules of the ES were also calibrated with cosmic rays prior to installation. The resolution of the calibration for the ECAL components was measured at the start of 7 TeV operation and was estimated to be less than 2% in the EB, about 5% in EE and 2.5% in the ES. The HCAL system was calibrated in a similar fashion as the ECAL except by using pion test beams for the absolute energy calibration and a Cobalt 60 source for intercalibration [73].

Link algorithm

As a particle passes through the detector, depending on its nature it may interact with different subdetectors. The core of the PF algorithm is the *link algorithm* which combines the different signals from various subdetectors compatible with a given particle. Testing all possible combinations of PF elements for compatibility would make the required computing time grow quadratically with the number of particles. In order to reduce the computation time, only the nearest neighbouring elements in the η-ϕ plane are tested for compatibility. In case a link is established, the distance between the elements is used to quantify the quality of the link. The link algorithm produces *PF blocks* which consist of elements that are either linked directly together or indirectly through a common element. The specific requirements for compatibility of the elements to be linked depend on the individual subsystems and are described below:

- A charged track and energy deposits in the calorimeter can be linked by extrapolating the track through the ECAL and HCAL systems. The link is made if the extrapolated track is within the cluster boundaries.
- The energy of bremsstrahlung photons emitted by electrons can be collected by extrapolating the tangents to the tracks at the tracker layer to a cluster at the ECAL. The conversion of photons into e^+e^- pairs in the tracker material is taken into account by matching the vectorial sum of two track momenta compatible with a photon conversion to the track tangents. In this case, the two tracks are also linked to the original track.
- The different calorimeter clusters can be linked together depending on the region: the HCAL and ECAL cluster beyond the tracker acceptance, and the ECAL and preshower cluster within the preshower acceptance. The HCAL-ECAL links or the ECAL-preshower links are established when the more granular cluster (ECAL and preshower respectively) is within the boundaries of the less granular one (HCAL and ECAL respectively)
- In order to reconstruct the nuclear interactions in the tracker material which can cause

the production of secondary particles, charged tracks with a common secondary vertex may be linked together. These secondary vertices are kept if they include one incoming track and at least two outgoing ones with an invariant mass above 0.2 GeV.

- Tracks in the inner tracker are linked to the segments in the muon detector depending on various conditions explained in Section 4.2.

For a given PF block, the identification and reconstruction sequence first starts with muons, then followed by electrons and isolated photons. Then the remaining elements in the block are checked for compatibility with charged hadrons, neutral hadrons, and non-isolated photons, followed by hadrons from nuclear interactions. After each of step, the PF elements used to form the objects are removed for further consideration in order to avoid double counting. Once a global description of the event has been created, the event goes through a post-processing in order to reduce the misidentification rates of objects.

Vertex reconstruction

The large design luminosity and the small crossing angle of the LHC result in additional proton-proton interactions in the same or different bunch crossing to overlap with the hard scatter. These secondary collisions, referred to as *pileup*, can create a challenging environment for the measurement and identification of the particles originating from the primary interaction. During the 2016 data taking period the CMS detector recorded an average number of interaction vertices, $< n_{\text{vertex}} >= 27$ as shown in Fig. 4.1.

The reconstructed tracks are used in order to measure the location of all the proton-proton interaction points in the event and to identify the primary vertex (PV) as the vertex corresponding to the hard scatter [70]. First a set of tracks compatible with having originated from the beam spot and having a sufficient number of hits in the tracker are selected. These tracks are then clustered using a deterministic annealing algorithm [74, 75] which estimates the most probable position for each vertex and assigns the most probable vertex as the origin of each track. For the vertex candidates containing at least two tracks, an *adaptive vertex fitter* (AVF) [76] is used in order to obtain the best fit value for the 3D vertex position, the covariance matrix and estimate of the fit quality. The AVF assigns a probability, w, to each track, where w can take values between 0 and 1 and corresponds to the likelihood that the track originated from the vertex in question. The closer w to 0 the larger the probability that the track originated from the vertex. The number of degrees of freedom in the fit is defined as:

$$n_{dof} = -3 + 2 \sum_{i=1}^{\#\text{tracks}} w_i. \tag{4.1}$$

This variable is useful in selecting genuine proton-proton interactions due to its strong corre-

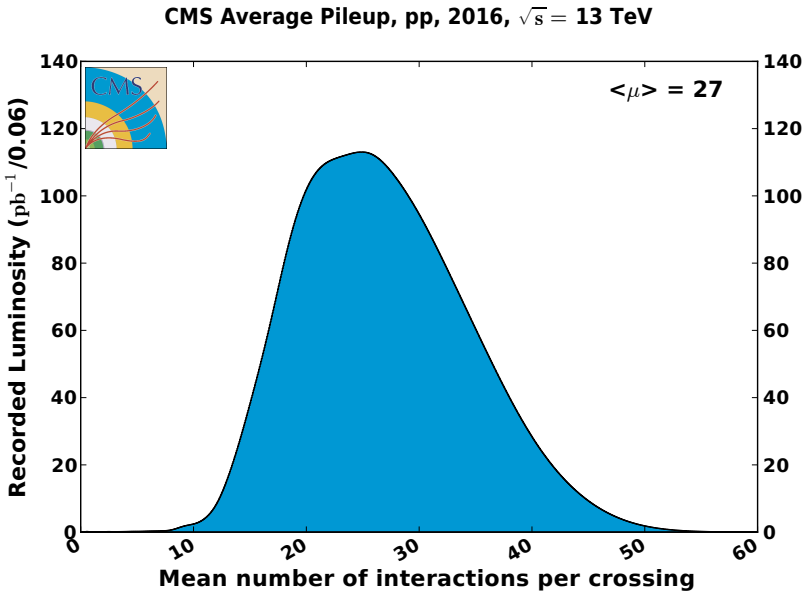

Figure 4.1: The mean number of interactions in a given bunch crossing as a function of recorded luminosity corresponding to the 2016 pp collision data of the CMS detector at 13 TeV [58]. The cross section for the inelastic scatterings is taken to be 80 mb.

lation with the number of tracks originated from the interaction region. The vertex position resolution and reconstruction efficiencies as measured in the early LHC data and the comparison to the simulated values are shown in Fig. 4.2. The primary vertex is then selected as the vertex with the largest quadratic sum of the track transverse momenta and the associated transverse missing energy, $\sum_i (p_{\mathrm{T}}^i)^2 + (p_{\mathrm{T}}^{\mathrm{miss}})^2$. All other vertices along the beamline are assumed to be minimum bias proton-proton interactions in the same bunch crossing. At the analysis level the primary vertex is required to have a minimum number of degrees of freedom of 4, be located within 24 cm in the longitudinal direction from the interaction point and have a radial distance smaller than 2 cm from the beamline.

Pileup

Particles arising from the pileup vertices can cause mismeasurements of the properties of hard scatter particles. It is therefore essential to remove the pileup contributions. The PF algorithm can be used to identify the charged particles associated with pileup vertices based on their tracks. The neutral particles, on the other hand, do not leave tracks and cannot be associated to a vertex. The contribution of these neutral particles can be measured in the simulation relative to the charged ones. These pileup-associated charged particles can then be removed from PF blocks and the associated neutral energy contribution can be used to correct the energy measurements of the physics objects.

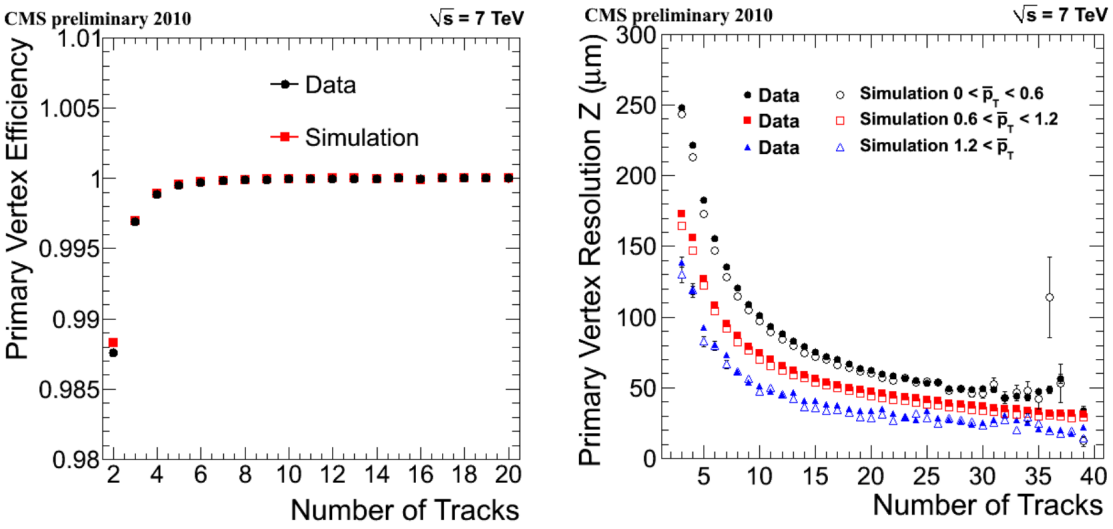

Figure 4.2: The efficiency of primary vertex (left) and the PV resolution in the z direction (right) as a function of the number of associated tracks [77].

Lepton isolation and impact parameter requirements

The absolute isolation (I_{abs}) of leptons is a measure of the total energy deposited in the vicinity of the lepton. This variable provides additional information regarding the source of the particle since leptons produced within jets are expected to have larger values of I_{abs} compared to the prompt leptons produced from the decay of vector bosons. In the PF algorithm the lepton isolation is defined by the sum of p_{T} of the charged hadrons, photons and neutral hadrons, i.e:

$$I_{\text{abs}} = \sum_{i}^{\text{charged hadron}} p_{\text{T}}^{i} + \sum_{j}^{\text{photons}} p_{\text{T}}^{j} + \sum_{k}^{\text{neutral hadron}} p_{\text{T}}^{k}, \tag{4.2}$$

where, in this analysis, each summation runs over the relevant PF candidates which are a distance $\Delta R = 0.3$ away from the lepton. In the first summation, only the charged particles associated to the primary vertex are used. The neutral pileup contribution to the isolation is estimated to be half of the sum of p_{T} of the charged hadron particles originating from pileup vertices, and is subtracted from the I_{abs}. The factor of one-half is the approximate value for the fraction of neutral particles to charged hadrons and is estimated in simulated inelastic proton-proton collisions [78]. Since more energetic leptons, are more likely to be surrounded with additional activity, a useful quantity is the relative isolation which is defined as the ratio of the absolute isolation of the lepton to its p_{T}, $I_{\text{rel}} = \frac{I_{\text{abs}}}{p_{\text{T}}}$. In this analysis a combination of absolute and relative isolations is used for the selection of electrons and muons. This hybrid

isolation depends on the p_{T} of the lepton and is defined by:

$$\text{Hybrid Isolation Requirement} = \begin{cases} I_{\text{abs}} < 5\,\text{GeV}, & \text{for } p_{\mathrm{T}}(\ell) \leq 25\,\text{GeV} \\ I_{\text{rel}} < 0.2, & \text{for } p_{\mathrm{T}}(\ell) > 25\,\text{GeV} \end{cases} \tag{4.3}$$

This p_{T} dependence of the isolation requirement allows for a more uniform selection efficiency for the leptons.

In order to further ensure that the selected leptons have originated from the primary vertex, the following requirements on the longitudinal (d_z) and transverse (d_z) components of the lepton impact parameter are required:

$$\begin{aligned} |d_z| &< 0.1 \text{ cm} \\ |d_{xy}| &< 0.02 \text{ cm}, \end{aligned} \tag{4.4}$$

where the impact parameter for the lepton is defined as the point of the closest approach to the PV of the track associated with the lepton. The combined selection efficiencies of the lepton isolation and impact parameter requirements are measured in data and simulated samples and are shown in Fig. 5.7.

4.2 Muons

At the CMS detector the muon system allows for efficient identification of muons over the full geometrical acceptance of the detector. Moreover, the high precision momentum measurements of the inner tracker improve the reconstruction of the muons. The information from the muon system and the tracker can be used to construct three types of muons [78]:

- **standalone muon**: the track segments are built by clustering the hits in the DT or CSC chambers. The momenta and positions of these segments are then used as the seeds in a pattern recognition algorithm based on a Kalman-filter technique which uses all the information from the muon subdetectors in order to reconstruct the standalone-muon tracks.

- **global muon**: the standalone-muon tracks are matched to the inner tracks from the tracker system by comparing the parameters of the tracks after propagating them to a common plane. In case of a match, the global-muon track is built by performing a combined fit using the standalone- and inner-muon tracks. This algorithm is also

referred to as "outside-in" method.

- **tracker muon**: The inner tracks with a total momentum greater than 2.5 GeV and $p_{\mathrm{T}} > 0.5$ GeV are propagated to the muon system by taking into account effects such as the magnetic field, average energy losses, and multiple scattering in the detector material. If the extrapolated track is matched to any muon segment then the inner track becomes a tracker-muon track.

About 99% of the muons produced within the geometrical acceptance of the muon system are reconstructed as either tracker muons or global muons and very often both. The global and tracker muons have also a better momentum resolution and a lower contamination from cosmic muons. The global-muon reconstruction typically requires track segments from at least two muon detector planes which reduces the misidentification rate of the hadron shower remnants reaching the muon system (punch-through). However, muons with very low momenta, $p_{\mathrm{T}} < 10\,\mathrm{GeV}$, often cannot reach the outer layers of the muon system and therefore have a lower reconstruction efficiency than global muons. The tracker muons, on the other hand, usually only match to segments in the innermost layer of the muon system and therefore have larger punch-through contamination.

For muons with $p_{\mathrm{T}} < 200\,\mathrm{GeV}$ the momentum is obtained from the tracker which has a superior resolution in this range while for more energetic muons the global track fit is used. These reconstructed muons are then passed on to the PF algorithm which improves the identification performance of the muons by taking advantage of the additional information from ECAL, HCAL and HO. The PF algorithm applies a set of quality criteria on the properties of tracker and global muons (standalone muons are not used.)

In this algorithm misidentified punch-through hadrons are rejected by requiring isolated global muons, i.e. requiring the total p_{T} contribution of other PF candidates within a distance $\Delta R = 0.3$ of the muon to be at most 10% of the p_{T} of it muon itself. For a non-isolated global muon, additional selection requirements are applied using variables such as the number of hits per track, or the degree of matching between tracker and standalone muon tracks. Depending on the desired level of balance between efficiency and purity, different types of the muon identification (ID) criteria [78] are used by various CMS analyses.

In this analysis the *loose muon ID* which ensures that the selected PF muon is either a global or a tracker muon is used. This loose identification criterion has a high efficiency for identifying prompt muons from the PV while maintaining a relatively low misidentification rate for charged hadrons. The performance of the PF ID which the loose muon ID is largely based on is shown in 4.3.

The *medium muon ID* is designed to have a high efficiency for prompt muons and muons from heavy flavor decays. The medium muons have to satisfy additional requirements on

variables such as the level of compatibility between the tracker and the standalone-muon track, and the normalized χ^2 of the track fit. A kink-finding algorithm is also used to ensure that various sections of the inner track are compatible with each other and to help reduce the misidentification rate of the selected muons. The *tight muon ID* is designed to suppress the muons from in-flight decays, hadronic punch-throughs and cosmic sources. This is achieved by requiring the muon to be reconstructed as a tracker and global muon and to satisfy additional conditions on variables such as the number of inner tracker and pixel hits, the normalized χ^2 of the track fit, and the longitudinal and transverse components of the track impact parameter. The tight muons are required to have at least one muon-chamber hit included in their global-muon fit and are also ensured to be compatible with a PV based on the longitudinal and transverse components of the muon impact parameter. The *soft muon ID* is targeted towards low-p_{T} muons from decays of b hadrons and quarkonia. These muons are high purity tracker muons with at least one hit in the pixel detector and loose compatibility criteria with the PV.

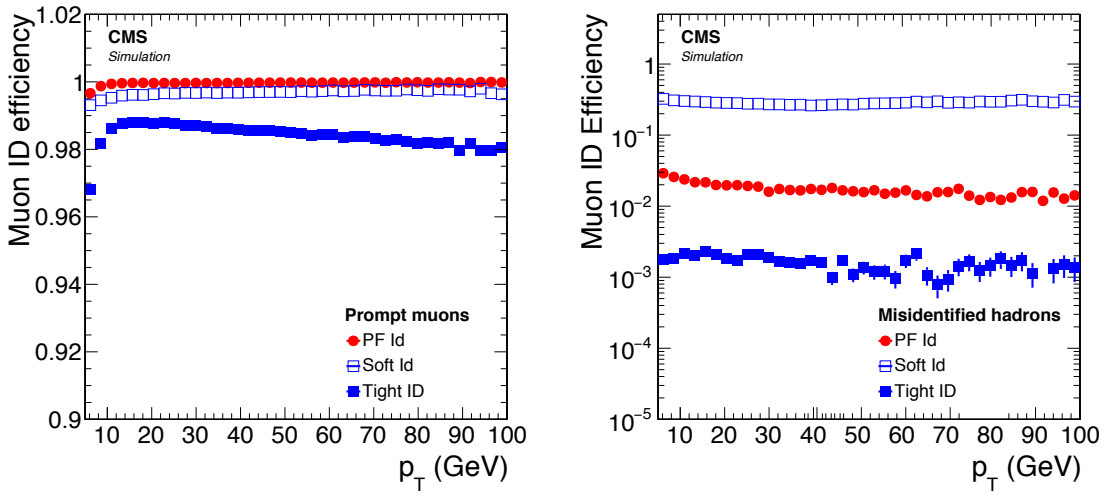

Figure 4.3: Efficiency (left) of the prompt muon identification and rate for misidentification (right) of hadrons as muons measured by the PF algorithm [69]. The soft and tight IDs refer to previous CMS muon IDs prior to the PF method.

4.3 Electrons and photons

The reconstruction of electrons at CMS takes advantage of both the inner tracks and the energy deposits in the ECAL system. Photons are reconstructed in a similar as electrons except without the tracker information [79].

Before reaching the ECAL, electrons may traverse up to two radiation lengths in the tracker material which, depending on their η, can result on average in 33%-86% of their energy to be radiated away by bremsstrahlung photons. Therefore to obtain an accurate

estimate of the electron energy it is essential to gather the energy of the radiated photons as well. Due to the different geometries of the ECAL system in the barrel and endcap region two separate methods, namely the "hybrid" and "multi-5x5" methods, are used respectively in order to form *superclusters* (SC) which include the clusters from the electron and the radiated photons. Both methods start with a seed crystal selected as the local maximum of energy depositions and then collect the energy of neighbouring crystals to form clusters, in a way that is optimized for the local geometry of detector. The neighbouring clusters are then coalesced into a SC if they pass the minimum transverse energy requirement of 0.1 GeV and 1 GeV in the barrel and endcaps respectively.

Reconstruction of electron tracks in the silicon detector requires a dedicated method which can deal with the radiative loss of electron energy. The bremsstrahlung of the electrons changes the curvature of electron trajectories and results in the loss of hits and therefore a poor estimation of track parameters. On the other hand, the electrons' large probability to radiate is used to differentiate them from charged hadrons.

For electrons with low energy loss, the KF approach can reconstruct the electron tracks in the tracker volume with the same efficiency as for muons. The trajectory of these well measured tracks can then be matched to PF clusters in the ECAL. For the tracks to be seeded to the next stage, the ratio of their matched PF cluster energy, E, to their track momentum, p must satisfy $r_{\text{cutoff}} < E/p < 3$, where r_{cutoff} is set to 0.65 (0.75) for electrons with $2 < p_{\text{T}} < 6\,\text{GeV}$ ($p_{\text{T}} \geq 6\,\text{GeV}$). In case of moderate radiative energy loss of electrons, the majority of track hits can still be collected by the iterative tracking, however typically yielding larger values of χ^2. Electrons emitting energetic photons can fail the above condition, since the pattern recognition algorithm cannot successfully deal with large changes in curvature of the electron trajectory. This results in a large number of hits being lost or a low quality fit with a very high χ^2. Therefore the tracks that failed the previous step are then fitted again with a Gaussian-sum filter (GSF) [80] which is capable of accommodating the radiation loss due to electrons. The GSF is a non-linear generalization of the KF and instead of assuming a Gaussian distribution of the energy loss uses a Gaussian mixture. In this method, the various Gaussian components are intended to quantify the different levels of bremsstrahlung energies and are weighted accordingly. The improved performance of this method compared to the KF approach is shown in Fig. 4.4. The GSF has larger computation requirements and in order to limit the processing time of the GSF fit in this stage, the fit is performed with 5 components. Finally, a boosted-decision-tree (BDT) classifier is used to select the tracker seeds based on the number of hits, χ^2 of GSF fit and its ratio to that of the KF fit, the geometrical and energy match of the PF cluster and the inner track.

The electron seeds selected by tracker- and ECAL- based approaches are then combined and processed by a more in depth GSF fit with 12 components. The resulting collection is

referred to as GSF tracks and is passed on to the PF algorithm. The use of tracker information enhances the seeding efficiency of electrons by almost a factor of 2, however this comes with the price of an increased probability for charged hadron to be seeded as electrons. This misidentification rate can be reduced by the PF algorithm using the additional information from other subdetectors, particularly the HCAL. The tracker information also allows for lowering the p_{T} reconstruction threshold of electrons from 4 GeV to 2 GeV. The seeding efficiency and misidentification rates of electrons are shown in Fig. 4.4.

The GSF tracks can become a seed for an electron candidate if their matched ECAL SC is linked to at at most two additional tracks. Photon candidates are reconstructed with a similar procedure as electrons, however their ECAL SC is required to have no link to a GSF track and have transverse energy $E_{\mathrm{T}} > 10\,\mathrm{GeV}$. To reduce the misidentification rate of charged hadrons as electrons, the deposited energy in the HCAL cells within distance $\Delta R < 0.15$ of the electron SC must be below 10% of the SC energy.

In order to ensure the optimal containment of the radiated electron energy, ECAL clusters and inner tracks may be additionally linked to the electron candidate. All ECAL clusters in the PF block linked to either the SC or one of the GSF track tangents are associated with the electron candidate. Inner tracks can be associated to the candidate if their momentum and their linked HCAL cluster energy are compatible with being an electron. Additionally, the tracks and ECAL clusters compatible with photon conversion signatures which are associated to the GSF track tangents are also linked to the candidate.

Several electron selection criteria corresponding to different levels of efficiency and misidentification rates have been designed using $\mathrm{Z} \to \mathrm{e}^{+}\mathrm{e}^{-}$ events. Due to the requirement of this analysis for low p_{T} leptons, the loosest criterion for electron identification (*Veto ID*) corresponding to 95% efficiency is chosen and its sequential selection is shown in Tab. 4.1.

Variable	requirement in barrel (endcap)	description
$\sigma_{i\eta i\eta}$	< 0.0115 (0.037)	Lateral extension of the shower along the η direction
$\Delta\eta_{in}$	< 0.00749 (0.00895)	Distance in η between the position of SC and inner track
$\lvert\Delta\phi_{in}\rvert$	< 0.228 (0.213)	Distance in ϕ between the position of SC and inner track
$\frac{H}{E}$	< 0.356 (0.211)	Ratio of energies measured in HCAL and ECAL
$\lvert\frac{1}{E} - \frac{1}{p}\rvert$	< 0.299	Absolute difference between the inverse ECAL energy inverse of track momentum of the electron.
N_{hit}^{miss}	≤ 2 (3)	Expected number of missing hits for the electron inner track

Table 4.1: List of the applied sequential selection for the identification of electrons in barrel and endcaps.

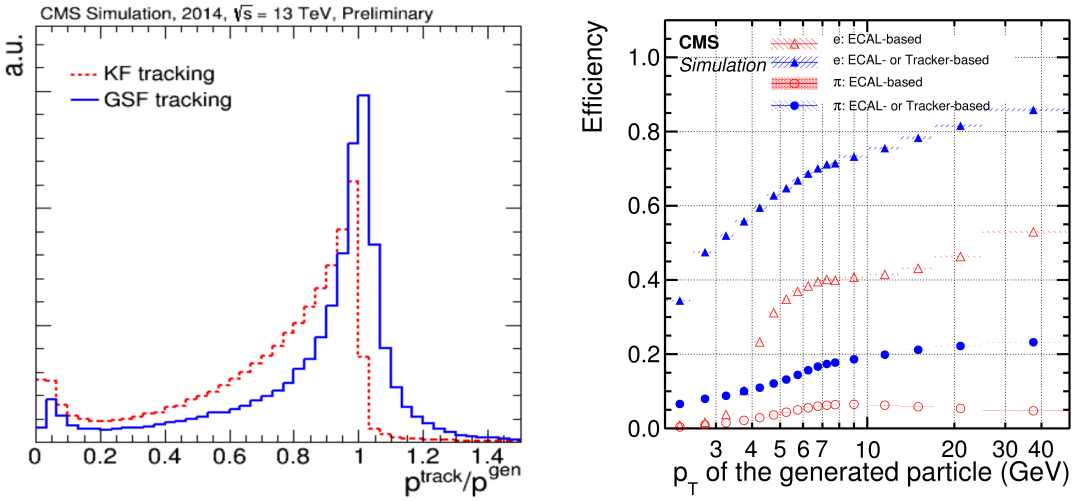

Figure 4.4: Left: comparison of momentum resolution of the reconstructed tracks using the GSF and KF algorithms with respected to the generated quantities [81]. Right: The electron seeding efficiency for electrons and pions as a function of p_{T} is shown for both the ECAL only and ECAL- or tracker-based approaches.

4.4 Jets

Jets are the most common observables for hadronic final states at particle physics experiments. Due to color-confinement of QCD, quarks and gluons produced inside the detector form color-singlet states in a process known as hadronization. These energetic color-neutral states can then radiate additional gluons which in turn create more quark-antiquark pairs. This creates a relatively narrow shower of particles referred to as a jet which can consist of charged hadrons (mostly $\pi^{\pm}$, $\mathrm{K}^{\pm}$, and protons), neutral hadrons (K^0 and neutrons), or non-isolated photons from π^0 decay. Electrons and muons can also be produced from the decay of charged hadrons (particularly b-flavored hadrons) within the jets. For typical jets, most of the energy is carried by charged hadrons ($\approx 60\%$), photons ($\approx 25\%$), and neutral hadrons to a smaller degree ($\approx 10\%$). The jet energy fractions due to the various components are shown in Fig. 4.5

The photons and neutral hadrons can be identified within the tracker acceptance by selecting ECAL and HCAL clusters which are not linked to an inner track. The precedence in ECAL is given to photons over neutral hadrons due to the fact that neutral hadrons typically only leave about 3% of the jet energy in the ECAL. The situation is more complicated outside the tracker acceptance ($|\eta| > 2.5$) since neutral and charged hadrons cannot be distinguished in this region. Moreover, the jet energy fraction of hadrons in the ECAL is similar to that of photons, therefore there is no justification for giving precedence to photons anymore. For this reason, ECAL clusters without a linked HCAL cluster are assumed to arise from photons, while ECAL clusters with such a link are considered as (neutral or charged) hadrons.

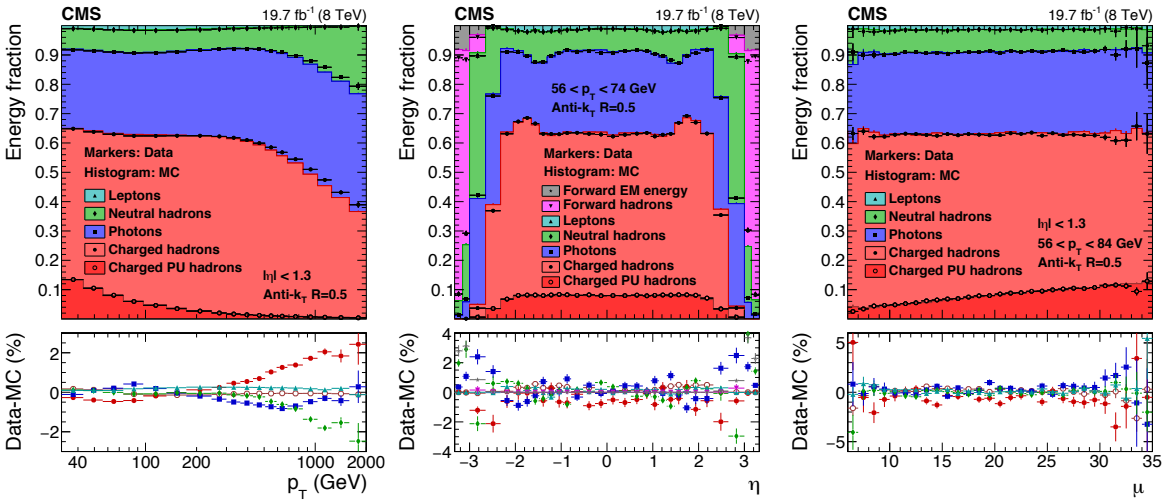

Figure 4.5: The observed and simulated jet energy compositions as a function of p_{T} (left), η (middle) and number of pileup interactions (right) [69]. The bottom panels show the difference between the observed and simulated compositions.

Jets (PF jets) are then reconstructed by clustering all PF particles using the anti-k_T algorithm [82] with a radius parameter $R = 0.4$. For the reconstruction of jets in the HLT, the calorimeter deposits (*Calo jets*) are used as the input of the clustering algorithm in order to reduce the latency. The PF jets perform significantly better than Calo jets in terms of energy and angular resolution as shown in Fig. 4.6.

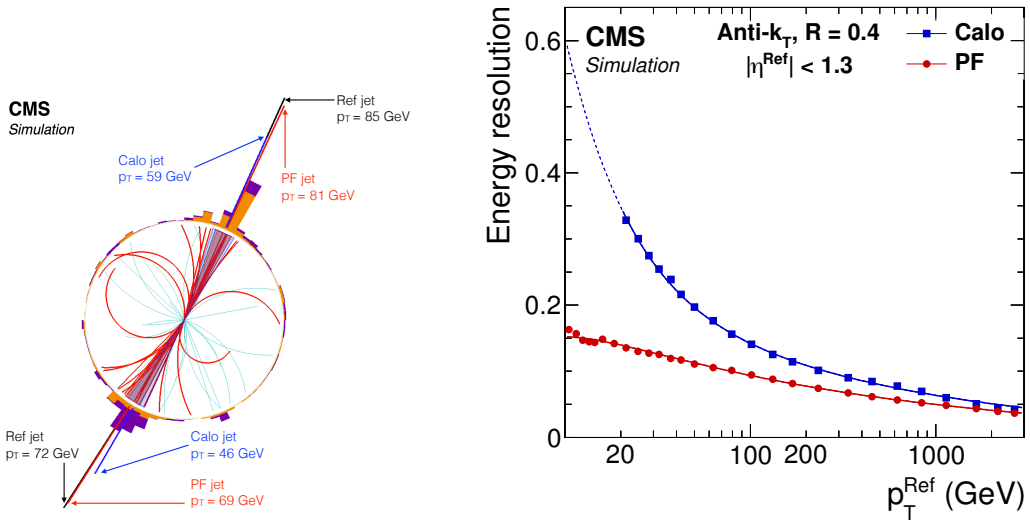

Figure 4.6: Left: an example of jet reconstruction in a simulated dijet event. The p_{T} of the of the PF jets are shown in red which can be compared to the p_{T} of the generated (Ref jet) and the calorimeter (Calo jet) shown in black and blue respectively. Right: comparison of the energy resolutions of the PF jet and Calo jet as a function of Ref jet p_{T} [69].

The clustering algorithm is based on the distance parameter d_{ij} between entities i and j

which can be either individual or a combination of particles and is defined as:

$$d_{ij} = \min(p_{Ti}^{-2}, p_{Tj}^{-2}) \frac{\Delta_{ij}^2}{R^2}, \tag{4.5}$$

$$d_{iB} = p_{Ti}^{-2} \tag{4.6}$$

where Δ_{ij} is the distance in the y-ϕ plane and d_{iB} is the distance between each entity and the beam. The algorithm proceeds by calculating the d_{ij} between all particle pairs and combines the two particles if they have the smallest distance. On the other hand if the smallest distance is d_{iB}, then the cluster i is selected as the final jet and removed from the event. The procedure is then repeated iteratively until there are no remaining clusters. The anti-k_T algorithm is free from infrared and collinear singularities and its jets are robust with respect to soft radiation and the smearing caused by pileup.

The *charged-hadron subtraction* (CHS) method is used to reduce the effect of pileup by removing the charged hadron tracks which are associated to a pileup vertex from the list of particles used in the clustering algorithm. The clustered jets used in this analysis are subject to additional set of requirements which correspond to the CMS *loose jet identification* [83]. The jets are required to have at least two constituents, with at least one of them being a charged PF candidate. The jet fraction energies due to neutral hadrons, photons, and electrons are required to be less than 0.99 for each of the contributions and the charged hadron contribution is required to be non-zero. These requirements reduce the probability to select badly reconstructed jets or jets originated from detector noise. The jets used in this analysis are required to satisfy $p_{\mathrm{T}} > 30\,\mathrm{GeV}$ and to be within the tracker coverage, i.e $|\eta| < 2.4$.

4.4.1 Jet Energy Corrections

Various factors can create differences between the energies of the clustered jets and the true parton energies. These include inhomogeneities in the detector response, imperfect geometrical acceptance of the detector and fluctuations in the hadronization or the underlying event. In order to correct for these effects a set of multiplicative corrections, known as jet energy corrections (JEC) are sequentially applied on the four-momentum, p_μ, according to the following equation [84]:

$$p_{\mu}^{\text{corr}} = \text{C}_{\text{offset}}(p_{\text{T}}^{\text{raw}}) \cdot \text{C}_{\text{MC}}(p'_{\text{T}}, \eta) \cdot \text{C}_{\text{rel}}(\eta) \cdot \text{C}_{\text{abs}}(p''_{\text{T}}) \cdot p_{\mu}^{\text{raw}}, \tag{4.7}$$

where the *raw* (*corr*) superscript represents the uncorrected (corrected) momentum, and C_{offset}, C_{MC}, C_{rel}, and C_{abs} represent offset, MC factor, relative and absolute corrections respectively. The offset correction is intended to remove the energy contributions due to the pileup particles. The pileup contribution due to charged particles is removed before clustering using the CHS method. The contribution due to neutral particles is removed by using the jet area method in which the average pileup energy contained within the effective area of the jet is removed from the p_{T} of the jet. The MC correction factor uses simulated events to obtain an energy calibration by comparing reconstructed jets with simulated jets. The relative correction factor is obtained in events with an azimuthally back-to-back dijet system in which conservation of momentum is exploited to measure inhomogeneities in the detector response. The absolute jet energy response is calibrated using γ/Z+jets events, where the clean leptonic signatures allow for the estimation of possible imbalances in the jet energy measurements. The total uncertainty of the corrections for central jet is around 5% for jets with $p_{\text{T}} = 20\,\text{GeV}$, and around 1% for jets with $p_{\text{T}} > 100\,\text{GeV}$ [85].

4.5 B-tagging

Identification of jets arising from b quarks (b-tagged jet, or b jet) can give important insights into the nature of hard scatter since the decay of top quark into b quarks is dominant source for these jets in SM. B jets can be identified by taking advantage of the relatively long lifetime ($c\tau \approx 450\,\mu\text{m}$) of the b quark which results in a secondary vertex (SV) shown in Fig. 4.7.

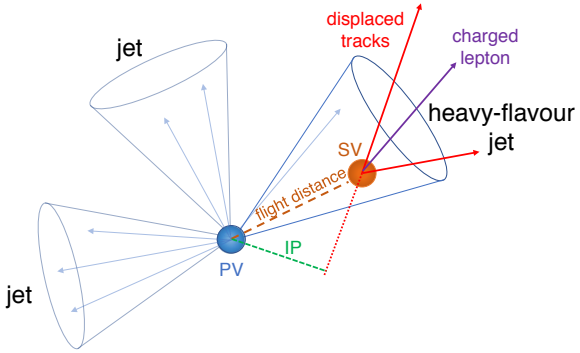

Figure 4.7: Illustration of a secondary vertex (SV) from a heavy flavored quark leading to a jet [86].

The b-tagged jets used in this analysis have been identified using the combined secondary

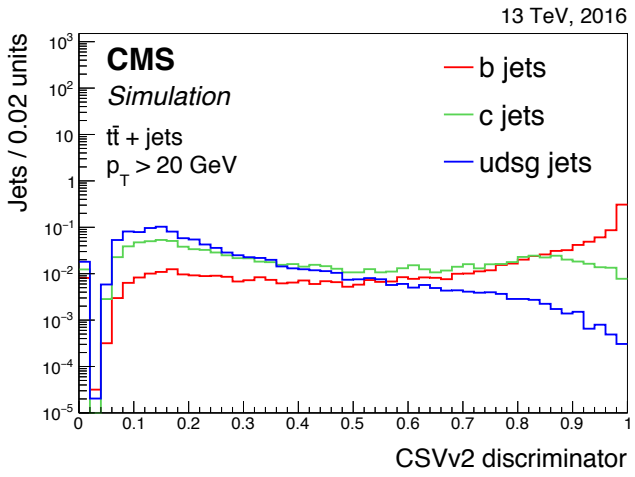

Figure 4.8: The distribution of the CSVv2 discriminant in a $t\bar{t}$ simulated sample for jets originating from b, c or light flavored quarks [86].

vertex (CSVv2) algorithm. In addition to the properties of the SV, this algorithm also uses the information of displaced tracks, the possibility of production of a muon or electron in the decay of the b hadron, and the p_T and η of the jets associated with SVs. It should be noted that identifying b jets based on the presence of electrons would not have been possible without the improved electron reconstruction efficiency brought by use of the tracker information. The secondary vertices are reconstructed using the inclusive vertex finding (IVF) algorithm based on inner tracks with $p_T > 0.8\,\text{GeV}$ and longitudinal impact parameter smaller than 0.3 cm. Tracks with sufficient displacement are used as the initial seed and are then clustered with other compatible tracks. The position of the SV is then estimated by performing the AVF on the tracks. The CSVv2 algorithm then assigns a discriminatory value to each jet using a neural network with one hidden layer [87]. The CSVv2 distribution for various heavy (bottom and charm) and light (up, down, strange and gluon) flavored jets is shown in Fig. 4.8. In this analysis jets with a CSVv2 value greater than 0.8484 are considered as b jets. This working point corresponds to an average efficiency of 65% for correctly identifying a b-tagged jet and a 1% probability to misidentify a light flavored jet as a b jet.

4.6 Missing transverse momentum

Due to their weakly interacting nature, neutrinos can escape all layers of the detector without leaving any trace. Additionally, possible exotic new weakly interacting particles such as the neutralinos or other dark matter candidates would also be invisible to the detector. The existence of such particles in an event may only be indirectly deduced by observing imbalances

in the momenta of the observed particles. Due to the lack of knowledge of the initial momenta of the colliding hadrons, in hadron colliders the momentum conservation can only be exploited in the transverse plane, therefore the relevant quantity is the *missing transverse momentum*, $\vec{p}_{\mathrm{T}}^{\,\mathrm{miss}}$. The majority of CMS analyses including the one presented in this thesis use the PF-$\vec{p}_{\mathrm{T}}^{\,\mathrm{miss}}$ calculated as the negative vectorial sum of all the PF candidates in such a way to balance the total transverse momentum of the event, i.e:

$$\vec{p}_{\mathrm{T}}^{\,\mathrm{miss}} = -\sum_{i}^{PF-candidates} \vec{p}_{\mathrm{T,i}}, \tag{4.8}$$

Mismeasurements of $\vec{p}_{\mathrm{T}}^{\,\mathrm{miss}}$ can be caused by various sources such as the nonlinearities in the detector response and the minimum energy and p_{T} thresholds of calorimeters and the tracker. This estimation is improved by propagating the jet corrections described in the previous section for the jets with $p_{\mathrm{T}} > 15\,\mathrm{GeV}$ in the calculation of $\vec{p}_{\mathrm{T}}^{\,\mathrm{miss}}$. This correction is referred to as the *type-I* correction. Additionally, only jets with at most 90% of their deposited energy in the ECAL are used in order to avoid double counting possible photons and electrons. To avoid overlaps with muons, the momentum of global and standalone muons which overlap with a jet is subtracted from the jet momentum, and the corresponding JEC for the modified jet p_{T} is used in the calculation of missing transverse energy.

The calculation of the $\vec{p}_{\mathrm{T}}^{\,\mathrm{miss}}$ relies highly on the accurate construction of all particles, and therefore the associated uncertainties depend on specific event topology and the scale and resolution uncertainties of the involved physics objects. The resolution of PF-$p_{\mathrm{T}}^{\mathrm{miss}}$ as a function of generated $p_{\mathrm{T}}^{\mathrm{miss}}$ is shown in Fig. 4.9.

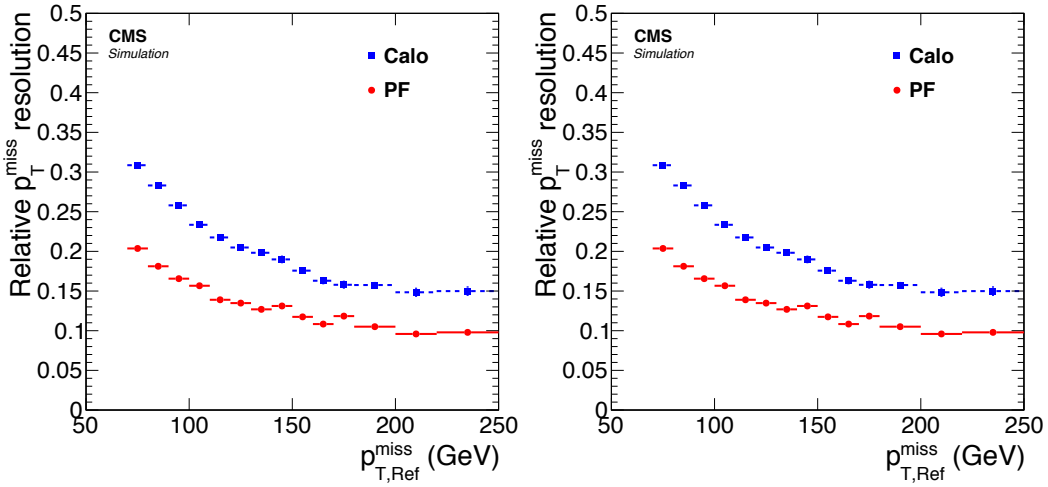

Figure 4.9: The relative resolution of the magnitude (left) and direction (right) $p_{\mathrm{T}}^{\mathrm{miss}}$ as a function of generated $p_{\mathrm{T}}^{\mathrm{miss}}$ ($p_{\mathrm{T,Ref}^{\mathrm{miss}}}$) for $p_{\mathrm{T}}^{\mathrm{miss}}$ calculated using PF (red) and calo (blue) quantities [69].

Search for supersymmetric partners of the top squark in models with compressed mass spectra at $\sqrt{s} = 13$ TeV

The analysis methods described in this thesis are designed according to the kinematical features of the signal models mentioned in Sec. 2.2.5. These SMS signal models consist of the pair production of the top squark decaying into a nearly degenerate LSP, a fermion pair and b quark via a direct four-body or chargino-mediated decay. The SMS diagrams corresponding to these signals are shown in Fig. 5.1. The distinctive feature of these signal scenarios is the low transverse momenta of the final state particles due to the small mass difference between the top squark and the LSP. The methods used in this document were developed based on the 8 TeV CMS search in similar kinematic regions [88] where only the muon channel was considered. A similar analysis with the addition of the electron channel was also performed on the partial 2016 CMS data [19]. Further optimization of the signal regions and improvements of the background validation and estimation methods were then implemented in the analysis of the full 2016 data of CMS as described in this thesis and a recent publication [18]. In the rest of this chapter the data, simulated background and signal samples, the correction factors for simulations, event filters for the data, signal and control regions, background estimation methods, systematical uncertainties affecting the analysis, the results and the statistical methods for interpretations are described in detail.

5.1 Data and simulated samples

In order test the background only and the background+signal hypotheses, it is necessary to have an accurate understanding of the SM background processes which contribute to final states resembling those of the signal. The background and signal processes are simulated using Monte Carlo (MC) event methods which not only generate the hard scatter from the

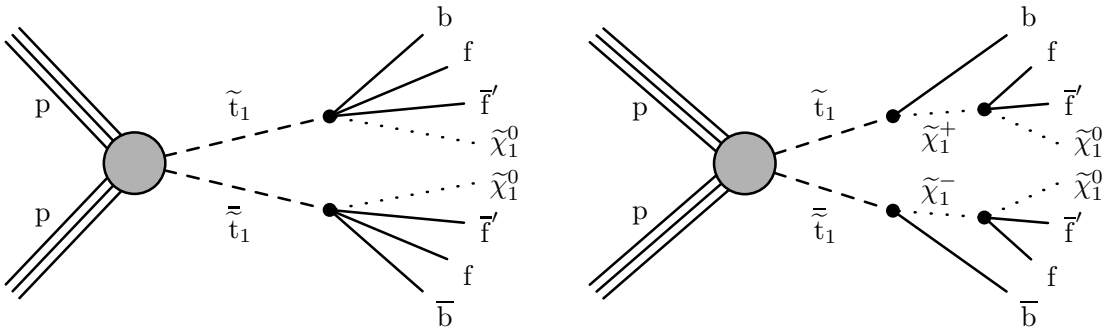

Figure 5.1: Simplified model diagrams corresponding to top squark pair production with a four-body decay (left) and a chargino-mediated decay (right) [18].

proton-proton collision but also simulate the detector response, geometry and the object reconstruction algorithms. An important input in the simulation of hadronic collision are the parton distribution functions (PDFs) which are used to sample the momenta of the incoming partons. PDFs are empirically determined functions which define the probability for a given parton to carry a certain fraction of proton momentum at a given factorization scale μ_F. The large momentum transfer in the hard scatter process implies that the partons are asymptotically free and therefore the computations can be performed within the realm of perturbative QCD. A schematic diagram of various components of simulating a proton-proton collision is shown in Fig. 5.2. For the MC samples in this thesis, various generators such as PYTHIA [89,90], POWHEG [91,92] and MADGRAPH5_aMC@NLO [93,94] are used for simulating the hard scatter as listed below:

- W+jets, $t\bar{t}$, Z/γ^* and QCD multijet processes are simulated at leading order (LO) with up to four extra partons using MADGRAPH5_aMC@NLO 2.3.3. In order to improve the statistical power of the simulated samples, the W+jets and Z/γ^* samples are produced in bins of H_T with boundaries ranging from 100 GeV to 2500 GeV, where the H_T is calculated using generator level quantities. For the $t\bar{t}$ sample the single- and di-leptonic components are produced separately.

- Production of single top quarks and the associated tW production are generated at next-to-leading order (NLO) with POWHEG v2.0 and POWHEG v1.0 respectively.

- Diboson processes are simulated at NLO for various production modes and final states using MADGRAPH5_aMC@NLO 2.3.3 or POWHEG v2.0.

- Production of top quark pairs in association with W, Z, or a gluon (collectively referred to as ttX) is simulated using MADGRAPH5_aMC@NLO.

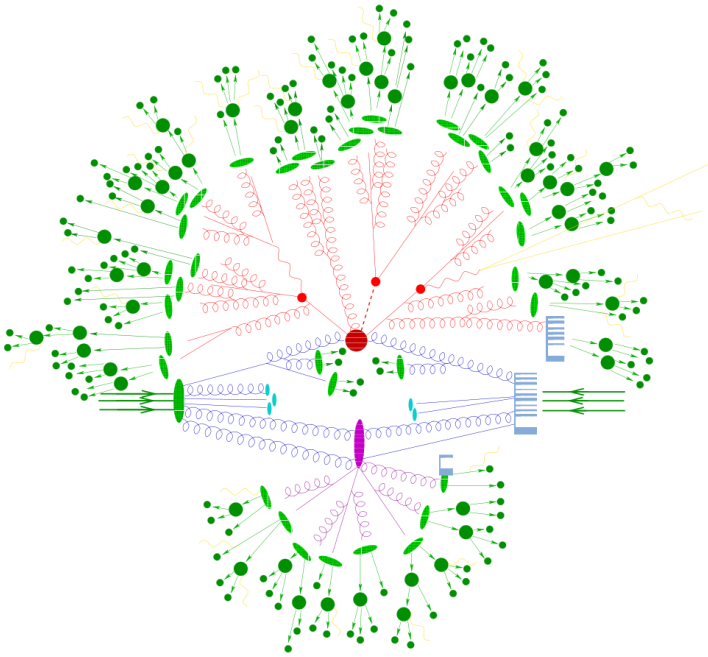

Figure 5.2: An illustration of the various components of a proton-proton collision as simulated by MC generators. The hard scattering process, typically calculated at a fixed order with a matrix element, is shown as the big red circle and the straight red lines and smaller red circles represent the resulting particles from the hard scatter and their subsequent decay. The violet blobs represent the interaction of other partons within the proton which may occur independently of the hard scatter (the underlying event). The initial- and final-state radiations are shown with the curly lines which result in the formation of hadrons in light green and finally producing the final state particles shown in dark green [98].

Depending on the order of the calculated matrix elements for each sample, the NLO or LO version of NNPDFv3 [95] parton distribution functions is used in a consistent manner. The NNPDFv3 is obtained from a global fit of the deep-inelastic and charm data from the HERA experiments and the Run 1 data of the ATLAS, CMS and LHCb experiments. The next step in simulation is the parton showering in which iterative methods are used to generate soft or collinear gluons from the scattering partons. Since these emissions may overlap in phase-space with the contributions from the matrix elements, possible double-counting is taken into about by utilizing an appropriate jet matching scheme [96]. As the partons radiate gluons, their energy scale decreases and eventually the parton interactions enter the non-perturbative regime. At this stage, the colored partons coalesce to form color-singlet states in a process known as hadronization. The parton showering and hadronization of the MC samples used in this analysis is performed using PYTHIA 8 with the CUETP8M1 tune [97].

At this stage the generated events with the hadronized parton showers are ready to go through the detector simulation. For this purpose GEANT4 [99] program is used to model the response of the CMS detector to the generated particles and their interactions with the

detector material. This step in the simulation which is referred to as FullSim is the most CPU and time consuming step of the MC production process and is generally used for the production of SM processes. Once the detector hits are simulated, the event reconstruction is performed with the same algorithms as those in data.

The pair production of top squarks with the addition of up to two extra partons as ISR is generated at LO using MadGraph5_aMC@NLO 2.3.3 and is then passed on to pythia 8.2.12 where the decay of the top squark is performed and is followed by parton shower and hadronization. The Breit-Wigner shape of the W boson mass is taken into account in the simulation of the top squark decay. The lifetime of the top squark is assumed to be zero and the polarization effects are neglected. For the simulation of signal samples, the CMS FastSim method [100] is employed in which the detector response is parametrized to obtain detector hits which then go through a very similar event reconstruction as data and the FullSim. The FastSim method significantly reduces the computing time for the generation of the signal which makes it possible to scan a wide range in the stop-LSP mass plane. The signal samples are generated for stop masses of $250 \leq m_{\tilde{t}} \leq 800\,\text{GeV}$ in steps of 25 GeV and LSP masses satisfying $10 \leq \Delta m \leq 80\,\text{GeV}$ in 10 GeV steps. For the case of the chargino-mediated SMS, the chargino mass is assumed to be half way between the stop and LSP masses for simplicity.

The stop pair production cross sections are calculated at NLO using the next-to-leading logarithmic (NLL) corrections [54]. The cross sections depend only on the mass of the top squark. For instance, in proton-proton collisions with a center-of-mass energy of 13 TeV, pair-produced top squarks with masses of 300 GeV and 500 GeV have cross sections of about 8.5 pb and 0.5 pb, respectively. In order to improve the number of useful simulated signal events used in the analysis, a filter at generation level is applied during the production which requires the events to satisfy $p_{\text{T}}^{\text{miss}} > 80\,\text{GeV}$ and $H_{\text{T}} > 160\,\text{GeV}$, where the variables are calculated using generator-level information. The efficiency of this filter for different stop and LSP masses ranges between 20% to 50% depending on the mass configuration. The filter efficiency for the chargino-mediated and four-body scenarios are very similar and the latter is shown in Fig. 5.3.

Data

The data sample used in this analysis was collected at the CMS detector in the 2016 proton-proton run of the LHC at a center of mass energy of 13 TeV. The collected data correspond to an integrated luminosity of $35.9\,\text{fb}^{-1}$ and the uncertainty in the measured luminosity is calculated to be 2.5% using the pixel cluster counting method [101]. The considered events in the analysis are certified to ensure that all subdetectors were functional when the event was recorded. The main dataset used in the analysis is collected based on $p_{\text{T}}^{\text{miss}}$ triggers and

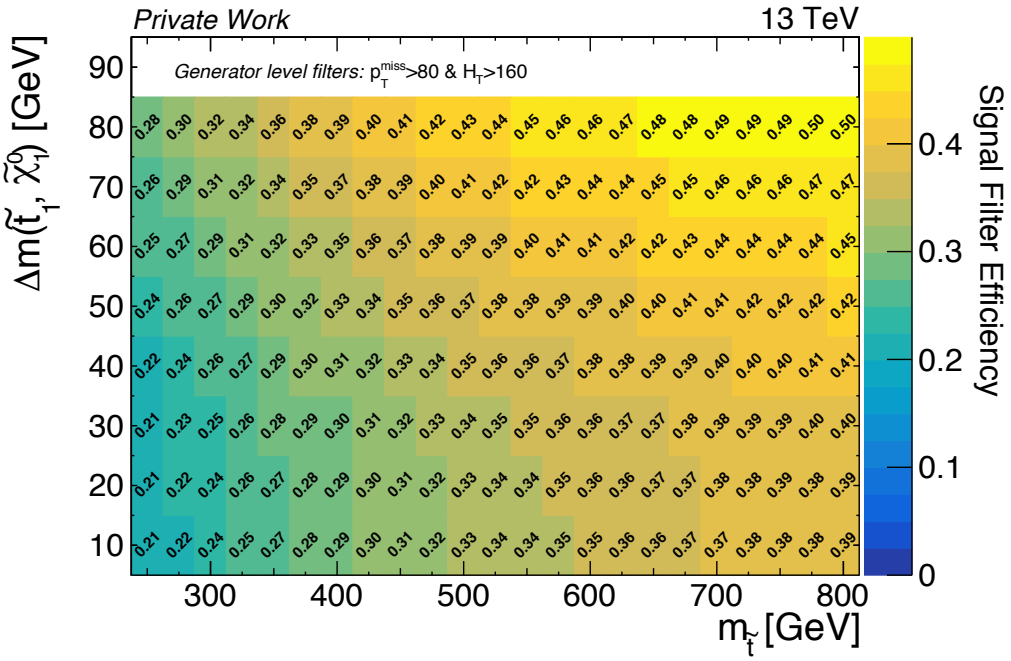

Figure 5.3: Efficiency of the generator-level filter applied in the simulation of four-body signal model.

is referred to as the `MET` primary dataset. Additionally, the `SingleMuon` and `SingleElectron` primary datasets collected based on muon and electron triggers with thresholds of 24 GeV and 27 GeV respectively were used for various measurements as described in the rest of this chapter. The datasets are also split based on their recorded time period which may have different operating conditions as such as beam intensity.

More specifically, the trigger paths used in this analysis are based on $p_{\mathrm{T}}^{\mathrm{miss}}$ and $H_{\mathrm{T}}^{\mathrm{miss}}$ quantities calculated at the trigger level, where $H_{\mathrm{T}}^{\mathrm{miss}} = |\sum_i^{jets} \vec{p}_{\mathrm{T,i}}|$. The corresponding trigger paths are labeled as `HLT_PFMETX_PFMHTX_IDTight`, where "`X`" is the common $p_{\mathrm{T}}^{\mathrm{miss}}$ and $H_{\mathrm{T}}^{\mathrm{miss}}$ threshold which ranges between 90 and 120 GeV in this analysis. With the increasing instantaneous luminosity during data taking periods, the trigger thresholds must also be increased in order to compensate for the rising trigger rates. In this analysis events are selected if any of the $p_{\mathrm{T}}^{\mathrm{miss}}$ triggers within the mentioned range is fired which is equivalent to taking the logical "or" of the triggers. The triggers have intrinsic inefficiencies which are mostly caused by the simplified event reconstruction at L1T compared to that in the offline analysis. In order to estimate the offline efficiency of the $p_{\mathrm{T}}^{\mathrm{miss}}$ trigger in the `MET` dataset, the `SingleElectron` dataset is used. The two datasets are collected based on different sets of uncorrelated triggers (they are orthogonal) which allows for an unbiased estimation of the trigger efficiency. This efficiency is calculated using events with an offline selection of $p_{\mathrm{T}}(\ell) > 30$ GeV, leading jet p_{T} >100 GeV and H_{T} >200 GeV. The trigger efficiency is calculated according to equation 5.1 and is shown in Fig. 5.4 as function of the offline $p_{\mathrm{T}}^{\mathrm{miss}}$. The trigger efficiency is measured to

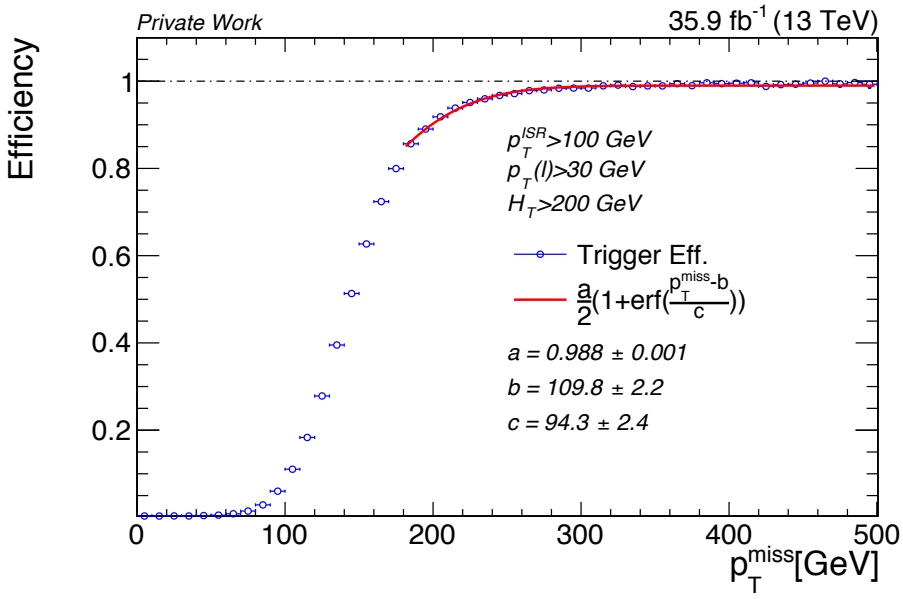

Figure 5.4: The measured efficiency of the $p_{\mathrm{T}}^{\mathrm{miss}}$ trigger in the selected region and the parameterized function fitted in the plateau region.

be about 99% for $p_{\mathrm{T}}^{\mathrm{miss}}$ >300 GeV but the relatively slow trigger turn-on results in the drop of the efficiency to around 90% for $p_{\mathrm{T}}^{\mathrm{miss}}$ =200 GeV. In order to take into account this effect in the MC samples, an error function is used to parameterize the trigger efficiency (shown in Fig. 5.4) and is applied on both signal and background simulated samples.

$$\epsilon = \frac{\text{number of events passing the probed trigger \& offline selection}}{\text{number of events passing the offline selection}} \tag{5.1}$$

5.1.1 Event cleaning filters

During the data taking some events may be contaminated by detector or reconstruction effects which can result in anomalous events with large amounts of $p_{\mathrm{T}}^{\mathrm{miss}}$ [102]. In the detector, these events can be caused for example by dead cells in the ECAL, spurious energy deposits due to noise or beam halo particles. In order to suppress these events in the data, a set of algorithms (referred to as filters) was developed during the Run 1 of the LHC and has been modified and extended for the Run 2 data taking according to the detector upgrades and data taking conditions. These $p_{\mathrm{T}}^{\mathrm{miss}}$ filters include:

- **HBHE noise filter**
  This set of algorithms identifies and removes sources of noise from the HCAL by either removing the energy spikes from the event reconstruction or rejecting the event com-

pletely. Additionally, combined topological information of HCAL, ECAL and tracks is used to identify isolated anomalous activities in the HCAL.

- **ECAL filters**
  An observed source of spurious $p_{\mathrm{T}}^{\mathrm{miss}}$ during Run 2 has been anomalous pulses produced at specific ECAL endcap supercrystals. The readout from these crystals is suppressed and the corresponding deposited energies are not used in the reconstruction of events.

- **Beam halo filter**
  The collision of protons with the collimators and residual gas in the LHC can result in the production of so called beam halo particles. The muons produced from the decay and absorption of these particle can enter the detector from outside, interact with the calorimeters, and hence result in large values of reconstructed $p_{\mathrm{T}}^{\mathrm{miss}}$ in the event. The beam halo filter uses the information of the muon CSCs and the calorimeters to detect events compatible with the collinear signature of this effect.

- **Bad muon and bad charged hadron filters**
  Events where a low quality track has a large contribution to the calculation of $p_{\mathrm{T}}^{\mathrm{miss}}$ are removed from the dataset if the track is identified as a misreconstructed muon or a charged hadron with $p_{\mathrm{T}} > 100\,\mathrm{GeV}$. These filters are applied to data and simulation since they can both be impacted by this reconstruction effect.

The application of these $p_{\mathrm{T}}^{\mathrm{miss}}$ filters significantly improves the agreement between data and MC, particularly in the tail of the $p_{\mathrm{T}}^{\mathrm{miss}}$ distribution as shown in Fig. 5.5. In this analysis, about 3% of the events are affected by these $p_{\mathrm{T}}^{\mathrm{miss}}$ filters after the preselection requirements are applied.

5.1.2 Correction factors for simulation

Various correction factors are applied to the MC samples in order to improve the modeling of the simulation with respect to observations. Some of these correction factors include experimental and detector issues, for instance the pileup distribution in data, which are not known during the MC production and must be accounted for a posteriori. Other theoretical factors, such as the ISR multiplicity, may be difficult to model properly and are corrected for based on dedicated studies.

Pileup correction

Since the exact value for the average number of pileup interactions in the data is not known before the full dataset is collected, the simulated samples are generated with a pileup profile

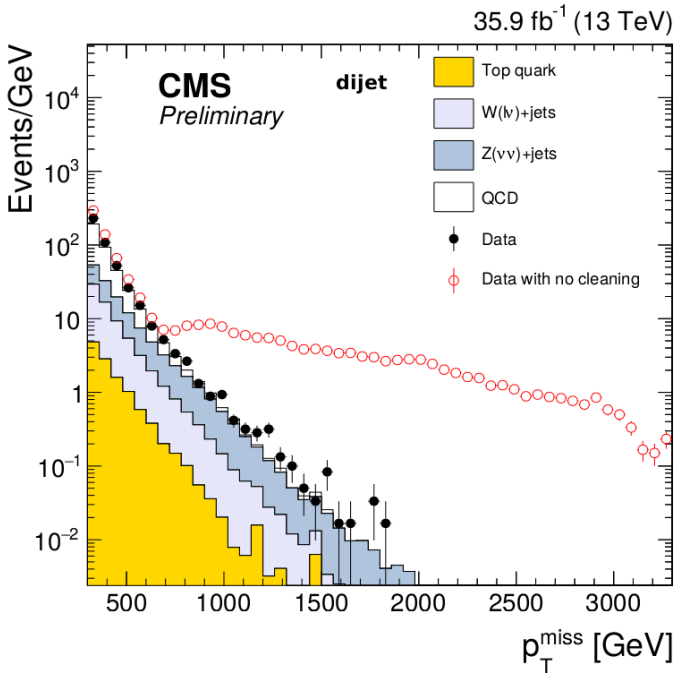

Figure 5.5: The $p_{\mathrm{T}}^{\mathrm{miss}}$ distribution in dijet events including the simulation (filled histograms) and the data with (filled markers) and without (open markers) cleaning algorithms applied [102].

which may not match the observed one. The pileup distribution in simulation is then corrected as a function of the number of interactions according to the observed pileup distribution. The observed number of interactions per bunch crossing is calculated as instantaneous luminosity times the cross section of the inelastic pp scattering, measured to be $69.20 \pm 3.46\,\mathrm{mb}$ [103]. The area normalized pileup distributions in data and simulation are shown in Fig. 5.6 and the ratio of the two is used to correct the simulation.

ISR modeling correction

The properties of ISRs in simulated samples have been notoriously difficult to model. In particular, the ISR jet multiplicity (N_j^{ISR}) and the p_{T} spectrum of the ISR jets ($p_{\mathrm{T}}^{\mathrm{ISR}}$) in simulated samples have been shown to exhibit discrepancies with respect to the observed quantities. In this analysis, in particular, the ISR modeling of $\mathrm{t\bar{t}}$ and W+jets samples is corrected for. For $\mathrm{t\bar{t}}$ events, the correction factors are obtained as a function of N_j^{ISR} in a region with two leptons and two b-tagged jets by comparing the ISR multiplicity distributions of data and simulation [104]. This correction is also applied on the signal sample since the pair production of top squarks is expected to be affected by similar mismodeling as the top pair production. These correction factors range between 0.92 for $N_j^{\mathrm{ISR}} = 1$ to 0.51 for $N_j^{\mathrm{ISR}} \geq 6$. For W+jets events, the p_{T} of the boson is reconstructed using generator level quantities and is used as a proxy for the $p_{\mathrm{T}}^{\mathrm{ISR}}$. The correction factors are obtained by comparing data and MC modeling of the p_{T} of the Z boson in dedicated samples [105]. These electroweak

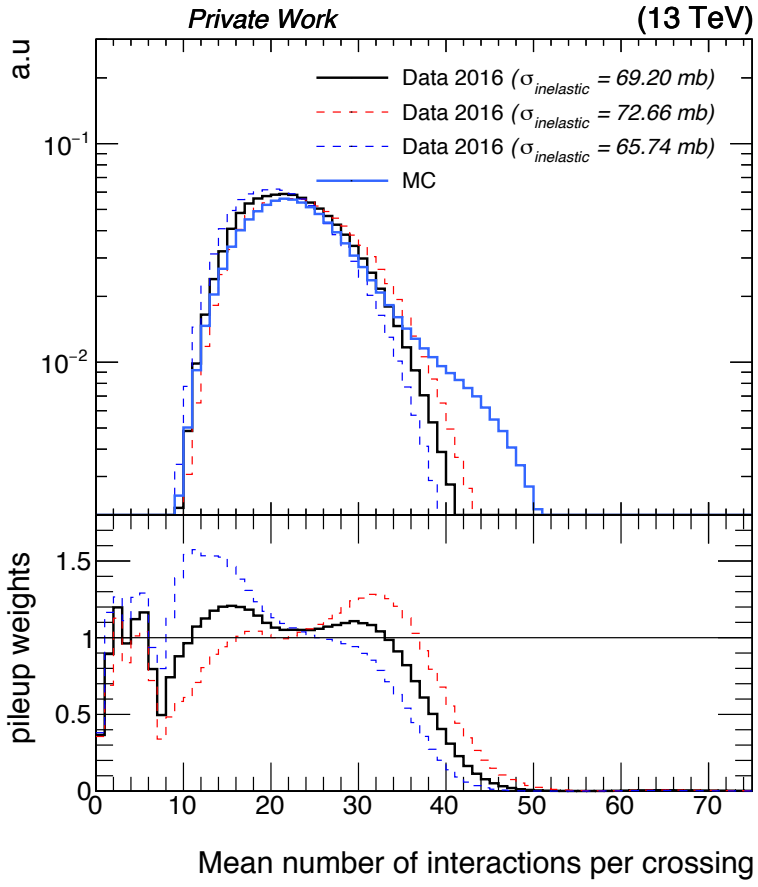

Figure 5.6: Area normalized pileup distribution in simulation and data are shown with solid blue and black lines. The dashed lines represent the $\pm 1\sigma$ variations in the measured inelastic cross sections. The bottom pad shows the ratio of the observed to simulated pileup distributions.

correction factors range between 1.18 for $100 < p_{\mathrm{T}}^{\mathrm{ISR}} < 150\,\mathrm{GeV}$ to 0.78 for $p_{\mathrm{T}}^{\mathrm{ISR}} > 600\,\mathrm{GeV}$. An additional cross-check was performed in a W+jets enriched sample where the correction factors were measured to be compatible with the ones mentioned above. These ISR correction factors are accompanied by an additional sample dependent factor in order to ensure that the cross section of the process stays constant before and after the correction is applied.

Lepton selection efficiency

The efficiencies for lepton selection and reconstruction are measured by applying a tag-and-probe method [106] on $\mathrm{Z} \to \ell^+\ell^-$ samples in both data and simulation. In this method, one lepton, referred to as the "tag," is required to satisfy a tight selection criterion and a second lepton, called the "probe," is selected based on the specific criterion which is under investigation. In order to select leptons compatible with having originated from a Z boson, they are required to have an invariant mass in the range of 60-120 GeV. A falling exponential is used to fit the background component of the invariant mass distribution and a double-Gaussian distribution is used to extract the signal component. The fit is performed for leptons which pass and fail the probe selection and the ratio of signal components of the two fits is used as the measure of the efficiency. The procedure is repeated in data and simulation and in various p_{T} and η bins for electrons and muons separately. The efficiencies are measured for the identification (left in Fig. 5.7) and the combined isolation and impact parameter selections (right in Fig. 5.7). For the identification efficiencies, the muon (electron) probes are based on tracker muons (GSF tracks) and for the combined isolation and impact parameter efficiencies, the muon (electron) probes satisfy Loose ID (Veto ID). The lepton scale factors are obtained as the ratio of the efficiencies in data and simulation and are applied to the simulated samples in order to take into account the residual data-simulation differences.

B-tag scale factors

The efficiencies of b-tagging algorithms in data and simulation have been compared for various topologies and are used to obtain data-to-simulation scale factors (SF) as a function of p_{T}, η and the flavor of the tagged jets. As described in Sec. 5.2 this analysis only uses the multiplicity of b jets and does not rely on other properties of the b jets. Therefore, instead of using the SFs to correct the properties of individual b-tagged jets, they are used in combination with the simulated efficiencies of b-tagged jets to calculate events weights corresponding to probabilities for each event to contribute to a specific N_{b} category. The b tagging efficiencies for heavy and light flavored jets in various η regions are measured in simulated samples. The efficiencies measured in a $\mathrm{t\bar{t}}$ sample are shown in Fig. 5.8 after applying selections similar to the ones described in Sec. 5.2. This implies that each event may contribute to various b-tag multiplicity regions which can improve the statistical power of the simulated samples.

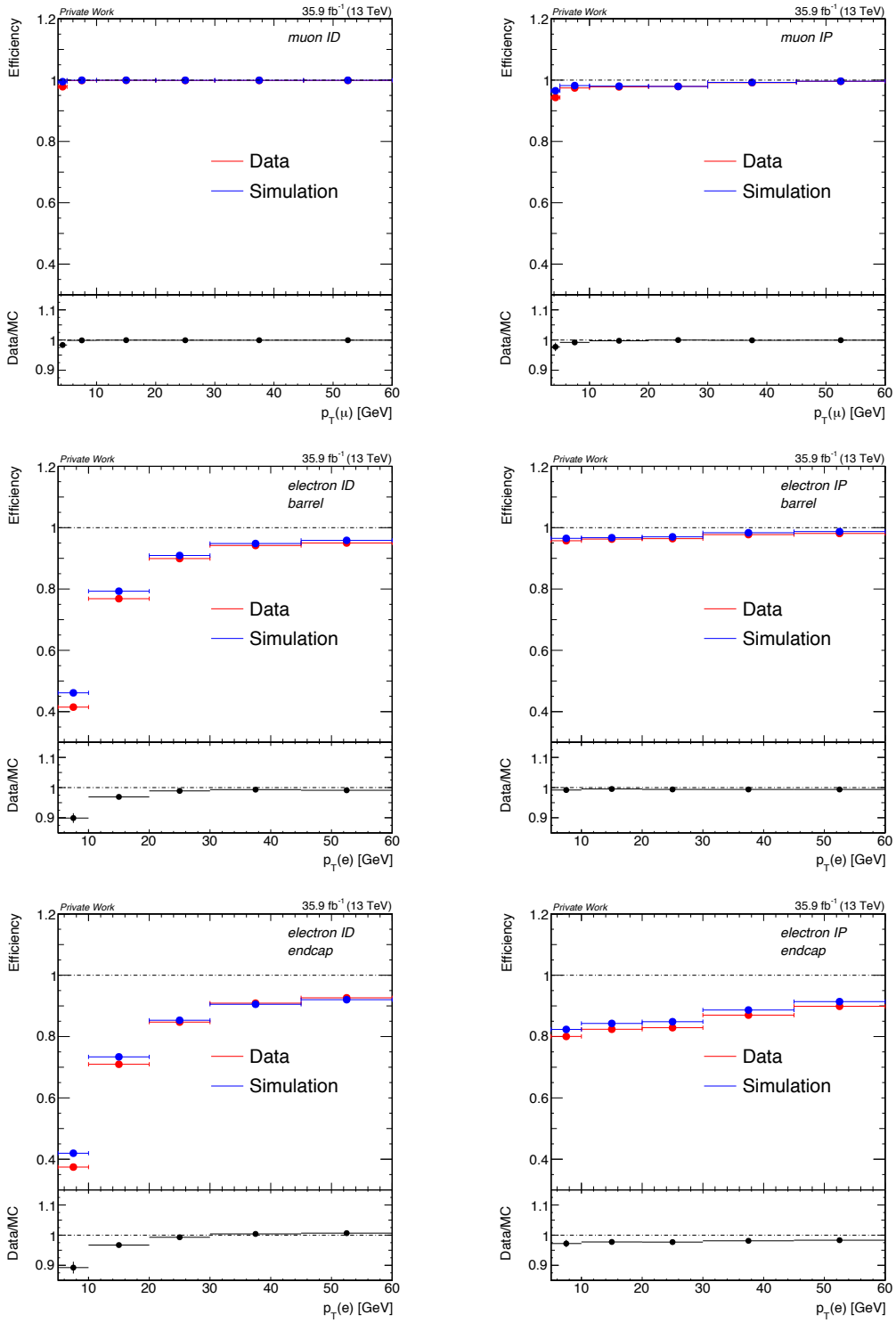

Figure 5.7: Identification (left) and combined impact parameter and isolation selection (right) efficiencies are shown for muons (top), electrons in the barrel region (middle) and electrons in the endcap region (bottom). The bottom pad of each plot shows the ratio of efficiencies in the data and simulated samples and represents the correction factor used for the corresponding leptons [107].

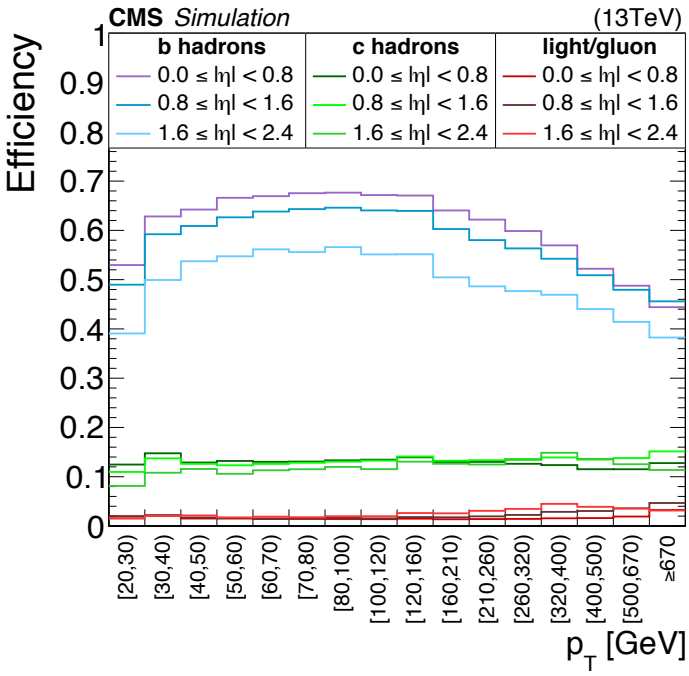

Figure 5.8: B tagging efficiencies for various jet flavors in different η regions are shown as measured in a simulated $\mathrm{t\bar{t}}$ sample [108].

The sum of event weights for different b-tag multiplicities must add up to 1. The corrected probability for the ith jet to be b-tagged (P_i) is then given by the product of SF for the jet and the calculated MC b-tag efficiency (ϵ_i):

$$P_i = SF_i \cdot \epsilon_i. \tag{5.2}$$

The event weight, i.e. the probability of the event to be reconstructed with n b-tagged jets (N_b) is then calculated using:

$$w(N_\mathrm{b} = n) = \sum_{i_0} \cdots \sum_{i_n} \left[P_{i_0} \cdots P_{i_n} \prod_k (1 - P_k) \right], \text{ with } i_\alpha > i_{\alpha-1} \text{ and } k \notin \{i_0 \cdots i_n\}, \tag{5.3}$$

where the sums and product are run over all the jets being considered for b tagging. In this analysis the b-tagging event weights are calculated for jets with $p_\mathrm{T} > 30\,\mathrm{GeV}$, soft jets (jets with $30 \leq p_\mathrm{T} < 60\,\mathrm{GeV}$) and hard jets (jets with $p_\mathrm{T} > 60\,\mathrm{GeV}$), resulting in b-tag multiplicities N_b, $N_\mathrm{b}^\mathrm{soft}$, $N_\mathrm{b}^\mathrm{hard}$ respectively.

5.2 Event Selection

The search described in this thesis is targeted towards pair production of top squarks accompanied by a nearly degenerate neutralino as the LSP as described in Sec. 2.2.5. The decay products of the signal from each top squark include a b quark, a neutralino and a fermion pair arising from an offshell W boson. Since neutralinos would be able to escape the detector without leaving a trace, requiring large amounts of transverse missing energy, $p_{\mathrm{T}}^{\mathrm{miss}}$, as a way of inferring the presence of the LSP is a typical feature of R-parity conserving SUSY searches. The hadronic channel, although more probable, is much more affected by the multijet final backgrounds prevalent at the LHC than the leptonic channel of the signal. For this reason, this analysis focuses on the cleaner signature with a single lepton.

One of the main challenges for searches in the compressed region is that the small amount of available energy for the final state particles results in low p_{T} (soft) leptons and jets which often fall below the trigger and reconstruction thresholds. Moreover, since relatively light neutralinos are still not fully excluded in the compressed region, the $p_{\mathrm{T}}^{\mathrm{miss}}$ of compressed signals are not as large as they are for typical SUSY signatures. This problem can be slightly mitigated by taking advantage of events in which the initial state partons emit radiation. In such events, the decay products would recoil against the ISR and gain an extra boost with respect to the laboratory frame. The massive neutralinos in particular benefit the most from the p_{T} boost which leads to larger $p_{\mathrm{T}}^{\mathrm{miss}}$ in the event while the leptons and jets remain relatively soft. However, since the initial state radiations are created in higher order processes, selecting an ISR has the adverse feature of having a low acceptance. The selected events for this analysis are then required to have at least one jet with $p_{\mathrm{T}} > 100\,\mathrm{GeV}$ as a proxy for an ISR jet. The assumption that an energetic jet is from ISR is justified by the fact that the signal jets from the decay products would be typically very soft.

The general strategy for new physics searches at the LHC is to select events according to the specific kinematical features of the signal model. Since new physics models have various parameters (the particles masses in the case of an SMS) it is often preferable to design the search in a way to maintain sensitivity to a wide range of signal parameters. The analysis regions used in this search are chosen based on their kinematic properties and are separated into *signal regions* (SRs) and *control regions* (CRs). The signal regions are chosen in a way to emphasize the kinematical features of the signal model and the control regions are regions with small contributions from the signal. In order to verify the background estimation methods a set of validation regions (VRs) is also selected in regions where the signal is not expected to have noticeable effects. The orthogonality of the analysis regions (SRs, CRs, and VRs) is ensured by distinct kinematic requirements on variables such as $p_{\mathrm{T}}(\ell)$, N_{b} and $p_{\mathrm{T}}^{\mathrm{miss}}$ and is described further in this chapter. The observed data in the background dominated control

regions is then utilized to estimate the contribution of SM processes in the SRs. Taking into account the relevant uncertainties for signal and background processes, the compatibility of the observed data in the SRs with the background-only and the signal+background hypotheses is tested using a likelihood ratio method.

5.2.1 Background Processes

As mentioned in Sec. 2.2.5, the signal final states investigated in this analysis include a soft isolated lepton, an energetic ISR jet, moderate missing energy and possible presence of soft b-tagged jets. Although selecting events with one lepton significantly reduces the dominant SM background at the LHC which are multijet QCD events, there still exist various SM processes with the mentioned final states which need to be taken into account. The main sources of backgrounds are the events which contain a leptonically decaying W boson. The W boson has roughly 25% probability of decaying into an electron or a muon accompanied by one or more neutrinos. Therefore the production of a W boson in association with a jet (W+jets), as shown in Fig. 5.9, can result in events which have very similar final states as the signal, particularly in events with no b-tagged jets. Kinematic properties of the final states, such as shapes of M_{T}, $p_{\mathrm{T}}^{\mathrm{miss}}$, and $p_{\mathrm{T}}(\ell)$ distributions, must then be exploited in order to discriminate these events from possible signal events. Another large cross section SM process which includes a leptonically decaying W boson is pair production of top quarks ($\mathrm{t\bar{t}}$) and to a much smaller degree the single top production. The top quark decays almost exclusively as $t \to \mathrm{W}b$ which makes the contribution of $\mathrm{t\bar{t}}$ more prominent in events with at least one b-tagged jet. In addition to the contribution from neutrinos, the missing energy in $\mathrm{t\bar{t}}$ events can also be induced by mismeasurements in the jet energies (fake-$p_{\mathrm{T}}^{\mathrm{miss}}$). The W+jets and $\mathrm{t\bar{t}}$ processes are the main backgrounds in this analysis and their estimation procedure is described in Sec. 5.3.1. Production of top quarks in association with a boson ($\mathrm{t\bar{t}W}$, $\mathrm{t\bar{t}Z}$, $\mathrm{t\bar{t}}\gamma$) collectively referred to as $\mathrm{t\bar{t}X}$ can also mimic the signal signature, however these processes have relatively small cross sections and therefore contribute to a much smaller degree. Moreover, Drell-Yan (DY) and diboson (VV) events are also a contributing SM background with prompt leptons. In addition to prompt leptons produced from the decay of bosons, misidentified (fake) and nonprompt leptons may also pass the selection criteria of the analyses. The fake and nonprompt leptons in this analysis are treated in a similar way and therefore the two terms are also used interchangeably in this document. The nonprompt leptons can arise from sources such as the semileptonic decays of c or b quarks and decay of light mesons. Unidentified photon conversions, jets with large contributions in the ECAL are also contributing factors for fake electrons. Punch-through particles from energetic showers entering the muon chambers can also result in misreconstructed muons. In this analysis electrons and muons arising

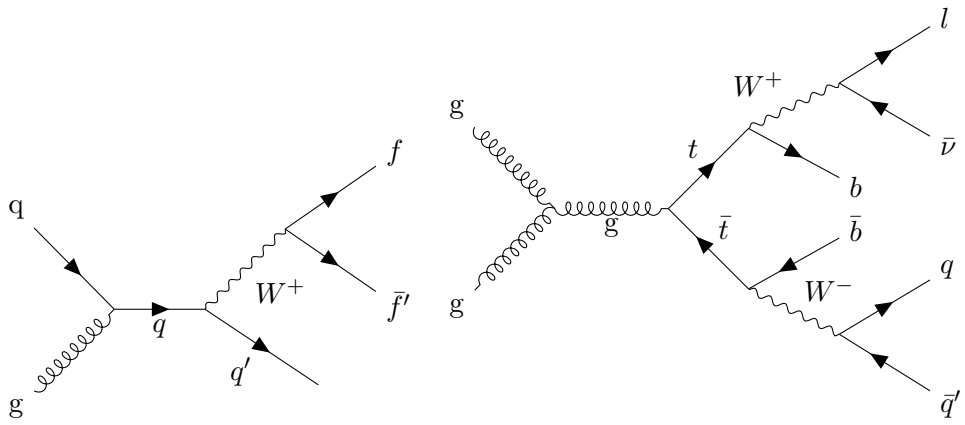

Figure 5.9: Examples of Feynman diagrams for the dominant background processes: the production of a W boson in association with jets (W+jets) on the left and the pair production of top quarks ($t\bar{t}$) on the right.

from the decay of τ leptons are considered as prompt. These nonprompt sources of leptons generally have much smaller probabilities than the prompt sources. However, the nonprompt contribution of leptons becomes non-negligible due to the large cross section of multijet inducing processes. Accompanied by the fact that mismeasurements in jet energies can lead to large amounts of fake $p_{\mathrm{T}}^{\mathrm{miss}}$, these processes can be misreconstructed with similar topologies as the signal and therefore enter the search regions. Another contributing SM background with nonprompt sources of leptons is the production of Z bosons in association with jets followed by the invisible decay of the Z boson ($\mathrm{Z} \to \nu\nu$+jets) which can have relatively large contributions in the signal regions where the dominant backgrounds are suppressed. Moreover, a small percentage of events in which a prompt lepton (mostly in $t\bar{t}$ and W events) is lost (due to lack of isolation or geometrical acceptance) and a nonprompt lepton is reconstructed can also contribute to the nonprompt backgrounds. All backgrounds contributing to nonprompt sources of leptons are treated together in this analysis and the methods used for estimating their contributions in the signal and control regions are described in Sec. 5.3.2.

5.2.2 Preselection

After requiring events with a single lepton, moderate $p_{\mathrm{T}}^{\mathrm{miss}}$, and an ISR jet, the dominant SM processes which can mimic the signal topology are the jet associated production of W bosons and top pairs (referred to as W+jets and $t\bar{t}$ events here on). These backgrounds include isolated leptons with a wide range of transverse momenta and also genuine $p_{\mathrm{T}}^{\mathrm{miss}}$ due to the presence of neutrinos. These processes have cross sections which are 3-5 orders of magnitude larger than the cross section for pair production of stops with mass of 500 GeV. Distinguishing these backgrounds from signal events is made more difficult by the fact that

the low lepton p_{T} region is largely dominated by these backgrounds. The W+jets events can be slightly discriminated against by requiring $H_{\mathrm{T}} > 300\,\mathrm{GeV}$ since the signal is expected to have a larger amount of hadronic activity than this SM process. To reduce the $\mathrm{t\bar{t}}$ background which often includes several energetic jets, events with more than two jets are vetoed if the third jet has $p_{\mathrm{T}} > 60\,\mathrm{GeV}$. Events with two or more jets get a significant contribution from QCD induced multijet processes. Such dijet topologies typically have back-to-back jets and can be suppressed by requiring $\Delta\phi(j_1, j_2) < 2.5$ radians, where j_1 and j_2 refer to leading and subleading jets respectively. To select the desired single-lepton topology in this search, events with at least one muon or electron with p_{T} above 3.5 and 5 GeV, respectively, are selected. Events with a hadronically decaying τ lepton, or a second electron or muon with $p_{\mathrm{T}} > 20\,\mathrm{GeV}$ are vetoed. From here on the term lepton is used to refer to only electrons and muons. At this level of selection (preselection), the W+jets and $\mathrm{t\bar{t}}$ events make up approximately 75% and 25% of the SM backgrounds respectively.

An important discriminatory variable used in this analysis is the transverse mass M_{T} which takes advantage of correlations between lepton momentum and $p_{\mathrm{T}}^{\mathrm{miss}}$ and is defined as:

$$M_{\mathrm{T}} \equiv \sqrt{2p_T^{\mathrm{miss}} p_{\mathrm{T}}(\ell)(1 - \cos(\Delta\phi(\vec{\ell}, \vec{p}_{\mathrm{T}}^{\mathrm{miss}})))}. \tag{5.4}$$

The M_{T} can be thought of as the projection of the invariant mass constructed by the lepton momentum $p_{\mathrm{T}}(\ell)$, and missing transverse momentum. In the case of W boson background events, the $p_{\mathrm{T}}^{\mathrm{miss}}$ is due to neutrinos which are created along with a lepton and therefore the transverse mass distribution has an endpoint around the mass of the W boson. The M_{T} regions above this kinematic endpoint are then to a large degree depleted from the W boson background events. In the case of the signal, however, $p_{\mathrm{T}}^{\mathrm{miss}}$ represents the vectorial sum of the neutralino momenta which is uncorrelated with the lepton p_{T}, resulting in a more uniform M_{T} distribution.

5.2.3 Signal Regions

At the preselection level described above, the SM processes dominate the benchmark signal models by a factor of 10^3-10^4. In order to gain sensitivity to the signal model, further suppression of the dominant backgrounds is made by exploiting the kinematical properties of the signal. Due to the kinematical constraints imposed by Δm, the leptons produced in the decay of the top squark tend to be much softer than those created in SM processes. Therefore the region satisfying $p_{\mathrm{T}}(\ell) \leq 30\,\mathrm{GeV}$ is selected for all SRs. The kinematical features of the signal are strongly dependant on the Δm, and in order to maintain sensitivity to a wide range

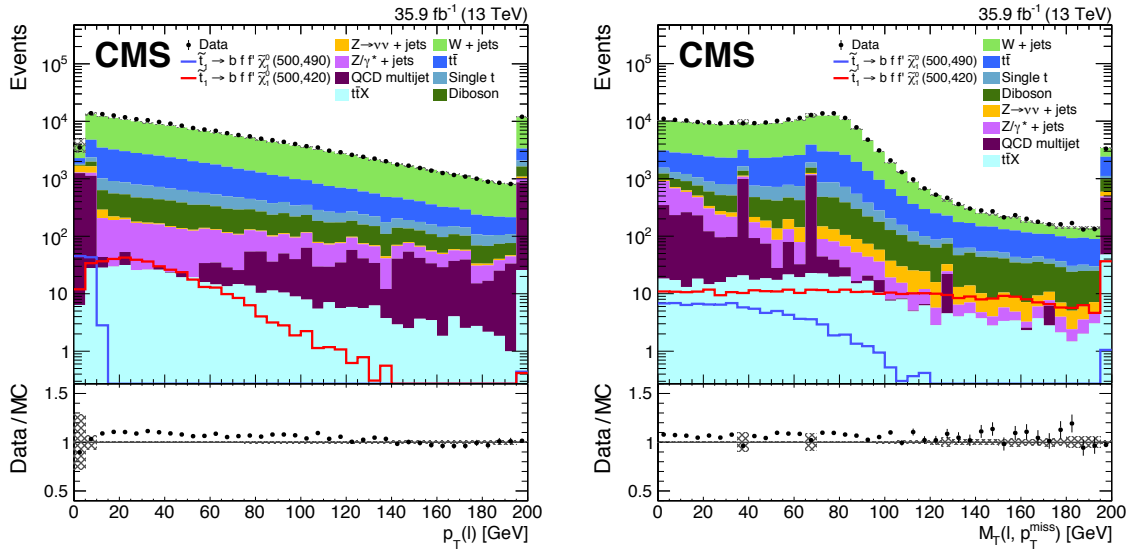

Figure 5.10: Distributions of $p_{\mathrm{T}}(\ell)$ (left) and M_{T} (right) are shown for events satisfying the described preselection [18].

of mass gaps, SRs are divided into two main regions, namely, SR1 and SR2, which roughly target small and large mass splittings respectively. The main distinguishing feature between the two signal regions is their b-tagging requirement which is described further below.

The missing transverse energy in signal and background processes is highly correlated with H_{T}, and $p_{\mathrm{T}}^{\mathrm{ISR}}$ as seen in Fig. 5.11. It can be seen that this correlation is much more prominent in the signal process and therefore these variables can be exploited to gain discrimination with respect to the backgrounds. In order to take advantage of these correlations two variables C_{T1} and C_{T2} are defined as:

$$C_{\mathrm{T1}} \equiv \min(p_{\mathrm{T}}^{\mathrm{miss}}, H_{\mathrm{T}} - 100\,\mathrm{GeV}), \tag{5.5}$$

$$C_{\mathrm{T2}} \equiv \min(p_{\mathrm{T}}^{\mathrm{miss}}, p_{\mathrm{T}}^{\mathrm{ISR}} - 25\,\mathrm{GeV}), \tag{5.6}$$

where the numerical values in the definitions have been optimized to maximize sensitivity to signal. In this search C_{T1} (C_{T2}) is used in the definition and categorization of SR1(SR2). The SR2 region has a larger contribution of $\mathrm{t\bar{t}}$ processes, and the use of $p_{\mathrm{T}}^{\mathrm{ISR}}$ in C_{T2} is motivated by its larger discriminatory power against $\mathrm{t\bar{t}}$ compared to C_{T1}.

Both SR1 and SR2 are divided into subregions according to M_{T}, $p_{\mathrm{T}}(\ell)$, and the corresponding C_{T} variable, according to the following:

- M_{T}: SRs are divided into three M_{T} regions by taking into account the peak of the M_{T} distribution around the W boson mass. These subregions are defined by $M_{\mathrm{T}} <$

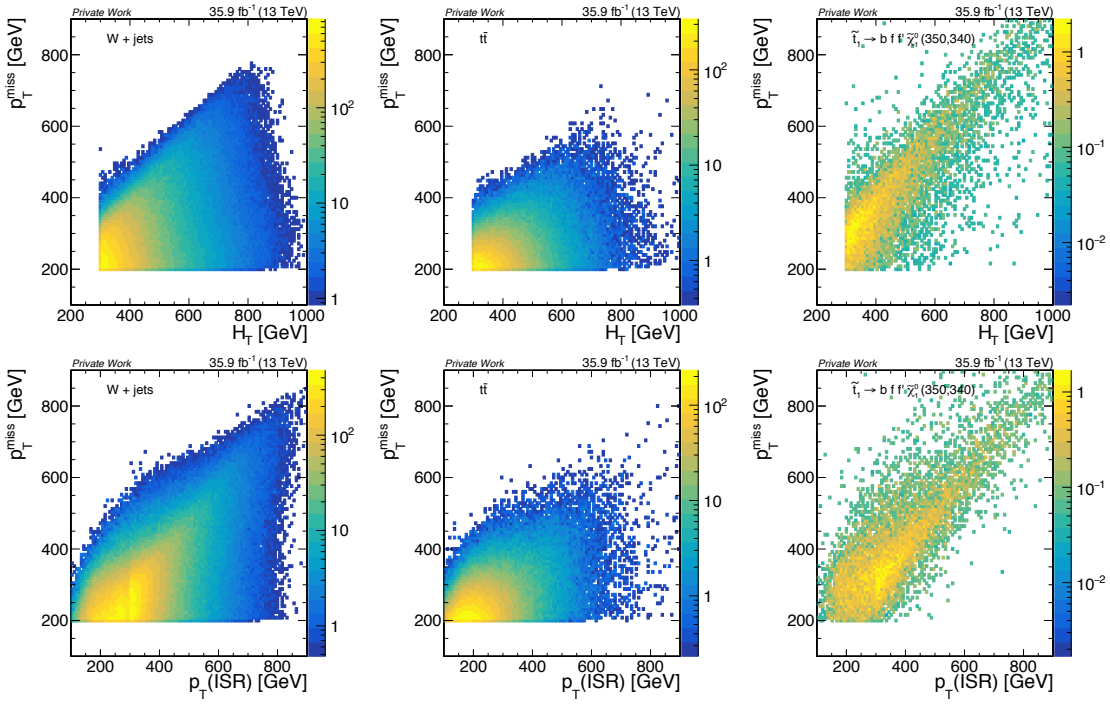

Figure 5.11: 2D distributions of $p_{\mathrm{T}}^{\mathrm{miss}}$ vs. H_{T} (top) and vs. $p_{\mathrm{T}}^{\mathrm{ISR}}$ (bottom) are shown for the W+jets (left), $\mathrm{t\bar{t}}$ (middle) and four-body signal model (right).

60 GeV, $60 < M_{\mathrm{T}} < 95$ GeV, and $M_{\mathrm{T}} > 95$ GeV and are labeled by letters, *a*, *b*, and *c* respectively.

- $p_{\mathrm{T}}(\ell)$: In order to take advantage of shape differences in the $p_{\mathrm{T}}(\ell)$ distributions of signal versus background and also to keep sensitivity to various Δm's which can have drastically different $p_{\mathrm{T}}(\ell)$ shapes, the SRs are subdivided into 3-4 regions based on $p_{\mathrm{T}}(\ell)$. Each of the three M_{T} bins is categorized (labeled) by $5 < p_{\mathrm{T}}(\ell) < 12$ GeV (L), $12 < p_{\mathrm{T}}(\ell) < 20$ GeV (M), $20 < p_{\mathrm{T}}(\ell) < 30$ GeV (H). Additionally, the two lower M_{T} regions (M_{T}^{a} and M_{T}^{b}) which benefit from larger number of events include an extra subregion dedicated to very soft muons defined by $3.5 < p_{\mathrm{T}}(\mu) < 5$ GeV (VL). The VL category is not implemented in the high M_{T} region (M_{T}^{c}) due to lack of events in this region and also the fact that such events would mostly manifest themselves in the presence of extremely large amounts of $p_{\mathrm{T}}^{\mathrm{miss}}$ which would also be highly susceptible to detector noise.

- $C_{\mathbf{Ti}}$: Each SR is also divided based on the corresponding C_{T} variable into two regions defined (labeled) as $300 < C_{\mathrm{T}} < 400$ GeV (X), and $C_{\mathrm{T}} > 400$ GeV (Y).

In SR1, events with a b jet satisfying $p_{\mathrm{T}}^{\mathrm{b\,jet}} > 30$ GeV are rejected, due to the fact that for very low mass splittings, e.g $\Delta m < 40$ GeV, the b jets from the stop decay tend to lack sufficient energy to be reconstructed properly. This requirement further reduces the contri-

Preselection:	
$p_{\mathrm{T}}^{\mathrm{miss}} > 200\,\mathrm{GeV}$	
$H_{\mathrm{T}} > 300\,\mathrm{GeV}$	
$N_{\mathrm{jet}}^{\mathrm{hard}} \leq 2$	
$\Delta\phi(\mathrm{hard\ jets}) < 2.5\mathrm{rad}$	
$N_\mu(p_{\mathrm{T}} > 3.5\,\mathrm{GeV}) + N_e(p_{\mathrm{T}} > 5\,\mathrm{GeV}) \geq 1$	
$N_\ell(p_{\mathrm{T}} > 20\,\mathrm{GeV}) = 1$	
$N_\tau(p_{\mathrm{T}} > 20\,\mathrm{GeV}) = 0$	
SR1 and CR1:	SR2 and CR2:
$N_b^{soft} = 0$	$N_b^{soft} \geq 1$
$N_b^{hard} = 0$	$N_b^{hard} = 0$
$\lvert\eta(\ell)\rvert < 1.5$	$C_{\mathrm{T2}} > 300\,\mathrm{GeV}$
$C_{\mathrm{T1}} > 300\,\mathrm{GeV}$	

Table 5.1: Common requirements for the preselection, signal and control regions. The SRs and CRs are distinguished by their requirements on the lepton p_{T}: $p_{\mathrm{T}}(\ell) \leq 30\,\mathrm{GeV}$ and $p_{\mathrm{T}}(\ell) > 30\,\mathrm{GeV}$, respectively.

bution of the $\mathrm{t\bar{t}}$ background in SR1. The H_{T} and $p_{\mathrm{T}}^{\mathrm{miss}}$ criteria are simultaneously tightened in SR1 by requiring $C_{\mathrm{T1}} > 300\,\mathrm{GeV}$. The dominating background in SR1, particularly in the M_{T}^a and M_{T}^b regions, is the W+jets process while in the M_{T}^c region other processes such as $\mathrm{Z} \to \nu\nu$ and DY become more important. At the LHC, positively charged W bosons are more likely to be produced than negatively charged ones while the pair production of top squarks (similar to pair production of top quarks) is by definition charge symmetric. Therefore, in order to reduce the W+jets contribution in M_{T}^a and M_{T}^b the selected lepton is required to have negative charge. The leptons are also required to satisfy $|\eta(\ell)| < 1.5$.

In SR2, events are required to have at least one soft b jet ($p_{\mathrm{T}}^{\mathrm{b\,jet}} > 30\,\mathrm{GeV}$) but events with a hard b jet ($p_{\mathrm{T}}^{\mathrm{b\,jet}} > 60\,\mathrm{GeV}$) are vetoed. This requirement on the number of b-tagged jets improves the sensitivity on signal scenarios with larger Δm, while maintaining a manageable contribution from $\mathrm{t\bar{t}}$ events. In SR2, the C_{T2} variable is required to be larger than 300 GeV which is equal to a simultaneous requirement of $p_{\mathrm{T}}^{\mathrm{miss}} > 300\,\mathrm{GeV}$ and $p_{\mathrm{T}}^{\mathrm{ISR}} > 325\,\mathrm{GeV}$. The higher $p_{\mathrm{T}}^{\mathrm{ISR}}$ requirement in SR2 compared to SR1 was shown to be more effective in reducing the contribution due to $\mathrm{t\bar{t}}$ events.

With the final binning of the signal regions in M_{T}, $p_{\mathrm{T}}(\ell)$ and C_{T}, a total of 44 signal regions are created with the full description of subregions detailed in Tab. 5.1 and Tab. 5.2. The sequential efficiency of the signal region requirements is shown in Fig. 5.12 for benchmark mass points of both signal scenarios.

SR label	C_{T} [GeV]	M_{T} [GeV]	$p_{\mathrm{T}}(\ell)$ [GeV]	CR label
SRVLaX	300-400	<60	*3.5-5	CRaX
SRLaX			5-12	
SRMaX			12-20	
SRHaX			20-30	
SRVLbX		60-95	*3.5-5	CRbX
SRLbX			5-12	
SRMbX			12-20	
SRHbX			20-30	
SRLcX		>95	5-12	CRcX
SRMcX			12-20	
SRHcX			20-30	
SRVLaY	>400	<60	*3.5-5	CRaY
SRLaY			5-12	
SRMaY			12-20	
SRHaY			20-30	
SRVLbY		60-95	*3.5-5	CRbY
SRLbY			5-12	
SRMbY			12-20	
SRHbY			20-30	
SRLcY		>95	5-12	CRcY
SRMcY			12-20	
SRHcY			20-30	

Table 5.2: Definition of signal region labels as applied to SR1, SR2, CR1 and CR2. The common selection criteria among subregions are defined in Tab. 5.1. The * indicates that the p_{T} requirement applies to muons only.

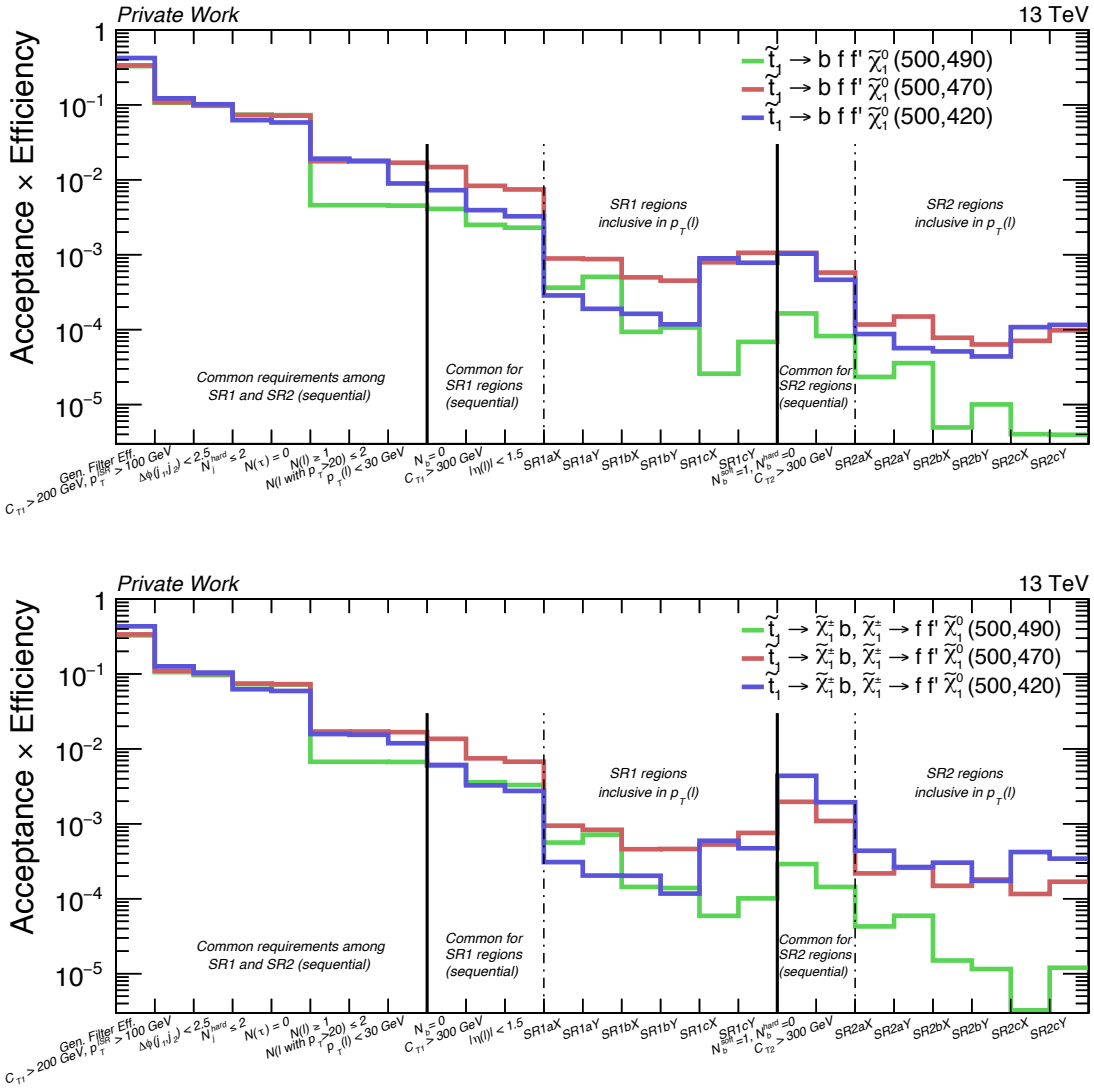

Figure 5.12: Acceptance-times-efficiency of the requirements used in defining the signal regions is shown for the four-body scenario (top) and the chargino-mediated scenario (bottom).

5.3 Background Estimation Methods

5.3.1 Estimation of main backgrounds

The normalization of the prompt-lepton component of W+jets and $t\bar{t}$ processes in the SRs is obtained simultaneously from data in dedicated CRs. The CRs are defined by reversing the $p_T(\ell)$ requirement of the SR to $p_T(\ell) > 30\,\text{GeV}$. As a consequence, each CR is shared by 3-4 SRs with a common M_T, C_T, and b-tag requirement. The W+jets and $t\bar{t}$ events comprise more than ~80% of background events in most signal and control regions. The CR1 and SR1

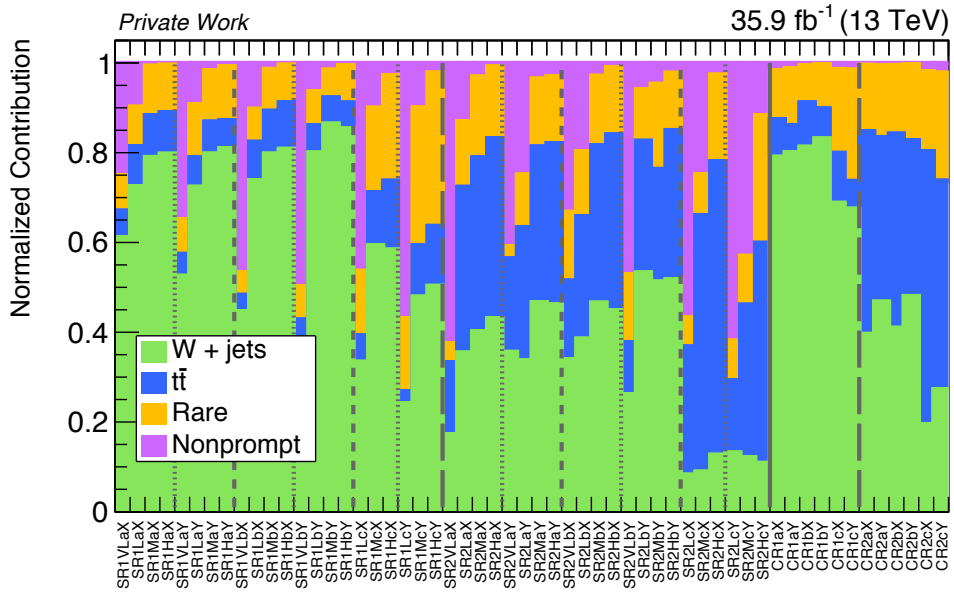

Figure 5.13: Composition of the backgrounds in the control regions.

are dominated by W+jets while similar contributions of W+jets and $t\bar{t}$ are observed in SR2 and CR2 categories. The contribution of rare backgrounds is typically around 10% but it can be as large as 30% in a few high-M_T high-C_T regions. The contribution of nonprompt leptons in most regions is below 1%, however in very low $p_T(\ell)$ regions, particularly, regions with $3.5 < p_T(\mu) < 5\,\text{GeV}$, their contribution can be as large as 50%. The relative contribution of the backgrounds in each of the signal and control regions is shown in Fig. 5.13.

Since $p_T(\ell)$ distributions of W+jets and $t\bar{t}$ are highly correlated, their normalization is obtained simultaneously in the CR. In the earlier versions of the analysis [19, 88], the global normalization of $t\bar{t}$ was obtained in a separate b-tagged enriched region and extrapolated to the rest of CRs and SRs. However, it was shown that having combined or separate scale factors for these backgrounds yield compatible total background estimates. Therefore, in this version of the analysis, the combined scale factor method was chosen which has the advantage of making the b-tagged enriched region available for use as a validation region as described in Sec. 5.3.3.

The scale factors for correcting the normalization of the W+jets and $t\bar{t}$ processes in each SR are obtained in the corresponding CR. More precisely, the scale factor in each region is obtained by taking the ratio of the observed number of events, after subtracting the non-prompt and rare contributions, to the total number of W+jets and $t\bar{t}$ simulated events. The nonprompt contribution subtracted from data is estimated from data in separate regions as described in Sec. 5.3.2. The method used to obtain the scale factor TF can be summarized

Table 5.3: Observed yields and simulated background contributions to CRs normalized to an integrated luminosity of 35.9 fb^{-1}. The corresponding scale factors for W+jets and $\text{t}\bar{\text{t}}$ are shown in the last column. The nonprompt contributions are estimated from data. Only statistical uncertainties are shown here.

Region	W+jets	$\text{t}\bar{\text{t}}$	Nonprompt	Rare	Total SM	Observed	Scale factor
CR1aX	2133±20	226.6±3.5	44.5±6.4	293.2±5.9	2698±22	2945	1.10±0.03
CR1aY	878.3±8.6	65.8±1.9	13.3±3.6	139.4±4.1	1097±10	1197	1.11±0.04
CR1bX	1107±15	134.5±2.7	7.8±2.7	112.1±4.1	1361±16	1462	1.08±0.03
CR1bY	438.2±6.4	35.1±1.4	1.6±1.6	51.9±2.9	526.8±7.3	502	0.95±0.05
CR1cX	642±11	103.8±2.3	12.7±3.0	174.3±5.5	932±13	1051	1.16±0.05
CR1cY	278.3±8.3	25.5±1.2	6.2±2.2	102.2±4.3	412.2±9.6	432	1.07±0.08
CR2aX	171.7±2.5	195.6±3.3	1.9±1.9	64.2±1.9	433.4±4.9	451	1.05±0.06
CR2aY	74.5±1.0	58.4±1.7	0.8±0.8	25.6±1.1	159.3±2.4	145	0.89±0.09
CR2bX	104.9±2.0	110.8±2.5	1.2±1.2	39.2±1.6	256.1±3.8	226	0.86±0.07
CR2bY	42.6±0.8	30.8±1.3	0.3±0.3	15.0±0.9	88.6±1.8	79	0.87±0.12
CR2cX	17.3±0.8	53.8±1.7	1.7±1.2	15.7±1.0	88.4±2.4	106	1.25±0.15
CR2cY	7.5±0.8	12.8±0.8	0.6±0.6	6.6±0.7	27.5±1.5	29	1.07±0.28

by the following equation:

$$\text{TF}_{\text{CR}} = \frac{N_{\text{CR}}^{observed} - N_{\text{CR}}(\text{nonprompt}) - N_{\text{CR}}^{\text{MC}}(\text{rare})}{N_{\text{CR}}^{\text{MC}}(\text{W+jets}) + N_{\text{CR}}^{\text{MC}}(\text{t}\bar{\text{t}})}, \tag{5.7}$$

where N and TF are the number of events and the scale factor of the indicated processes in a SR or CR. The superscript MC indicates that the number of events is obtained from simulated events. The final estimate of the main backgrounds in the SR, $N_{\text{SR}}^{pred.}$, is obtained by correcting the normalization of the simulation in the SR using the scale factor:

$$N_{\text{SR}}^{pred.}(\text{W+jets or t}\bar{\text{t}}) = \text{TF}_{CR} \times N_{\text{SR}}^{MC}(\text{W+jets or t}\bar{\text{t}}) \tag{5.8}$$

The observed number of events and the background contributions used to obtain the scale factors are shown in Tab. 5.3. The measured scale factors range between 0.86 and 1.25.

5.3.2 Estimation of nonprompt backgrounds

The contribution of nonprompt lepton backgrounds in signal and control regions is estimated from data in regions orthogonal to both signal and control regions using the so-called *tight-to-loose* method [109, 110].

This method is based on defining data application regions orthogonal to each of the main analysis regions (the SRs and CRs) by selecting events with leptons which pass a *loose* set of isolation and impact parameter requirements but not the nominal (*tight*) ones. The application regions, based on these *loose-not-tight* leptons have the exact kinematic requirements as their corresponding analysis region except for the tight lepton requirements. Nonprompt events in the application region are then reweighted by the factor, $\frac{\epsilon_{TL}}{1-\epsilon_{TL}}$, where the *tight-to-loose* ratio, ϵ_{TL}, is the probability for a nonprompt lepton passing the loose selection to also pass the tight criteria. The loose lepton criterion is defined by relaxing the isolation of leptons to $I_{\text{abs}} < 20\,\text{GeV}$ for $p_{\text{T}}(\ell) < 25\,\text{GeV}$ and $I_{\text{rel}} < 0.8$ for $p_{\text{T}}(\ell) > 25\,\text{GeV}$ in addition to relaxing the impact parameter requirements to $|d_{xy}| < 0.1\,\text{cm}$ and $|d_z| < 0.5\,\text{cm}$.

A separate region, referred to as *measurement region*, enriched by nonprompt leptons is used for measuring the tight-to-loose ratio as a function of lepton p_{T} ad η. This measurement region uses the `JetHT` primary dataset of CMS and is based on HLT triggers with requirements of $H_{\text{T}} > 800\,\text{GeV}$ and $p_{\text{T}}(j) > 450\,\text{GeV}$. At the offline level, these trigger requirements are matched by selecting events with $H_{\text{T}} > 900\,\text{GeV}$. In order to reduce the contribution of prompt leptons, the measurement region is also required to satisfy $p_{\text{T}}^{\text{miss}} < 40\,\text{GeV}$ and $M_{\text{T}} < 30\,\text{GeV}$, where M_{T} is calculated using the leading loose lepton.

The tight-to-loose ratios for electrons and muons are measured separately for each flavor in order to account for their distinct sources. The high p_{T} muons in the measurement region get a large contribution from the prompt sources as seen in Fig. 5.14 (middle-left and middle-right). A more suitable measurement region for these muons is constructed in a low H_{T} region by using the `SingleMuon` dataset with a HLT muon p_{T} threshold of 50 GeV, where no isolation criterion is applied on the muon. In addition to the M_{T} and $p_{\text{T}}^{\text{miss}}$ requirements of the nominal measurement region, the alternative measurement region is required to satisfy $p_{\text{T}}^{\text{ISR}} > 100\,\text{GeV}$. The muon p_{T} distributions for the tight and loose selection criteria are shown in Fig. 5.14. The measured tight-to-loose ratios for electrons and muons are shown in Fig. 5.15 as a function of p_{T} and for $|\eta|$ values smaller and larger than 1.5. These values are then used to reweight the observed numbers of events in the application regions after subtracting the prompt contribution estimated by simulation. It can be seen that for muons in the forward η region and $p_{\text{T}} > 200\,\text{GeV}$, the uncertainties for the tight-to-loose ratio is very large. This is due to the fact that this region is dominated by prompt leptons which results in very large uncertainties after subtracting the prompt contribution from the observed number of events. This region, however, is only a small contributing factor in the nonprompt estimation of the CR2 (compared to the central η and lower $p_{\text{T}}(\ell)$ contributions) and therefore has a negligible effect on the final estimation. In some cases where the prompt contribution in the application region is large, the subtraction of the prompt contribution can result in a negative value for the nonprompt estimation. In such cases a maximum likelihood fit (MLF) is used to constrain

the nonprompt contribution in the signal region. The values obtained from the MLF and the simple prompt subtraction methods in these regions are shown in Fig. 5.16.

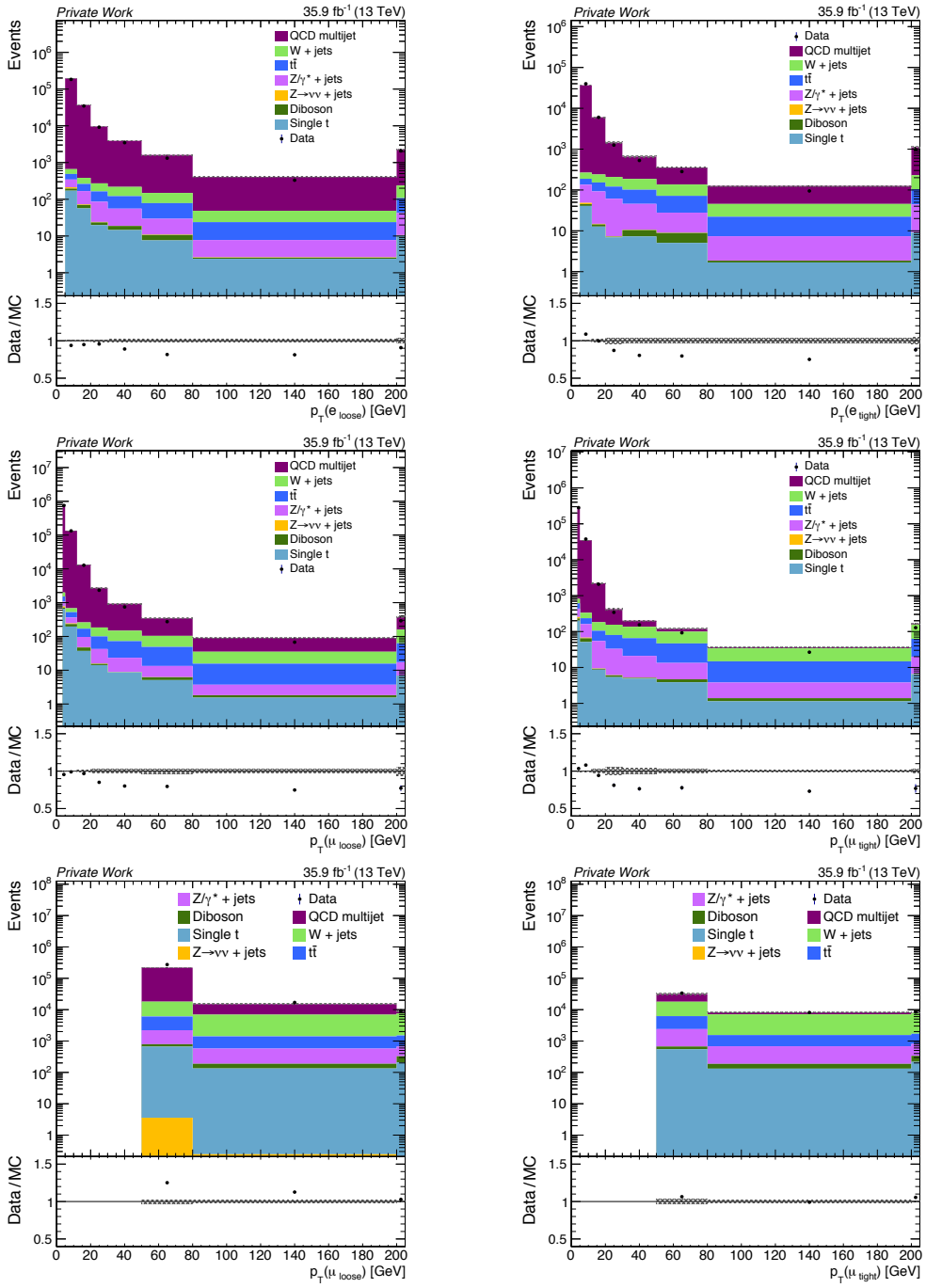

Figure 5.14: p_{T} distributions of leptons passing the loose (left) and tight (right) selection criteria are shown in the main measurement region for electrons (top) and muons (middle) and in the low H_{T} measurement region for muons (bottom) [110].

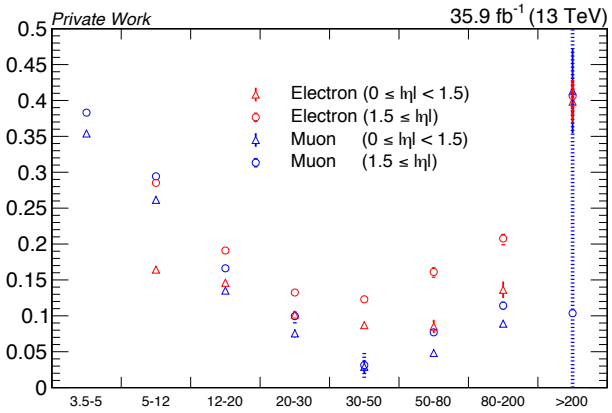

Figure 5.15: Tight-to-loose factors measured in data for electrons and muons.

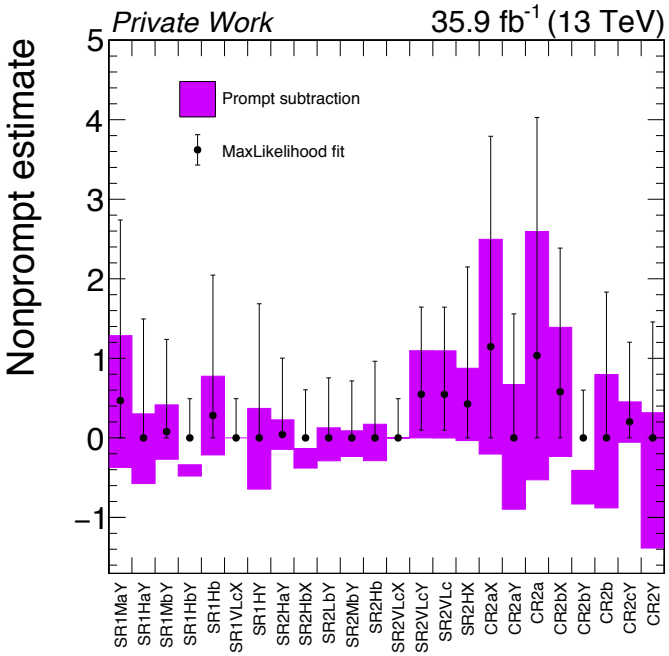

Figure 5.16: The comparison of the nonprompt background estimates based on the simple prompt subtraction and the maximum likelihood fit.

5.3.3 Validation of background estimation methods

In order to verify the background estimation methods used in this analysis, the full estimation procedure is performed in separate validation regions. These validation regions are designed in a way to be kinematically similar to the main analysis regions without overlapping with signal and control regions of the nominal analysis.

The nonprompt backgrounds in the VR are estimated from corresponding application regions in a similar way as described in Sec. 5.3.2. The systematic uncertainties described

in Sec. 5.4 are also fully taken into account. The contribution of the prompt backgrounds in the "signal region" part of the VR is estimated by fitting the normalization of the prompt backgrounds in the "control region" part of the VR. The kinematic relationship between these validation regions and the nominal analysis regions is shown in Fig. 5.17.

More specifically the first set of validation regions, labeled by (VW), are defined by lowering the C_{T} requirements in the main analysis regions to $200 < C_{\mathrm{T}} < 300\,\mathrm{GeV}$, where C_{T} refers to C_{T1} and C_{T2} in SR1 and SR2 respectively. The VW validation regions have similar background compositions as the main analysis SRs and CRs as seen in Fig. 5.18. This VR is kinematically neighboring $C_{\mathrm{T}}(X)$ regions and therefore can provide a robust test for these regions. Another set of validation regions, labelled by VB, is defined by replacing the b-tag requirements of the analysis regions with $N_{\mathrm{b}}^{\mathrm{hard}} \geq 1$. The VB regions provide a test of the background estimation methods in the full range of C_{T}, M_{T} and $p_{\mathrm{T}}(\ell)$ categories as shown in Fig. 5.19 (top). Due to smaller number of events in VB, the validation is also performed by combining the $p_{\mathrm{T}}(\ell)$ bins and is shown in Fig. 5.19 (bottom). The predictions in all validation regions are compatible with the observed number of events within the uncertainties as seen in Fig. 5.18 and Fig. 5.19.

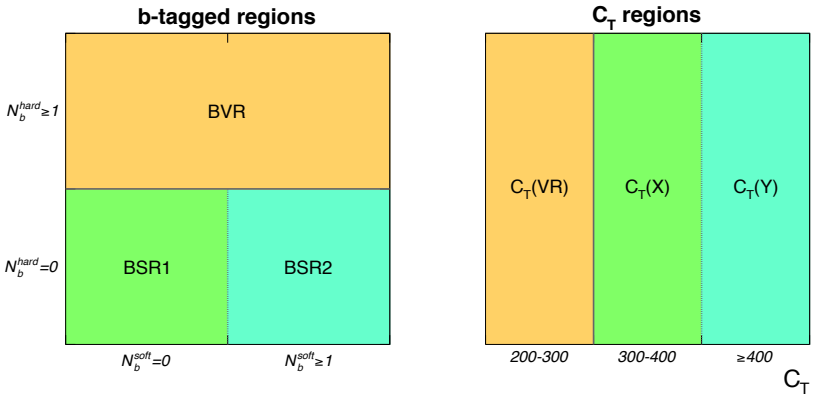

Figure 5.17: Schematic diagrams showing the relationship of validation, signal and control regions in terms of C_{T}, $N_{\mathrm{b}}^{\mathrm{soft}}$ and $N_{\mathrm{b}}^{\mathrm{hard}}$.

5.4 Systematic Uncertainties

5.4.1 Systematic uncertainties on the background estimation

As described in Sec. 5.3.1 the normalization of the main backgrounds in the signal regions is obtained from high lepton p_{T} control regions. This method implies that the predicted values of these backgrounds in the signal regions is only sensitive to the differences of uncertainties

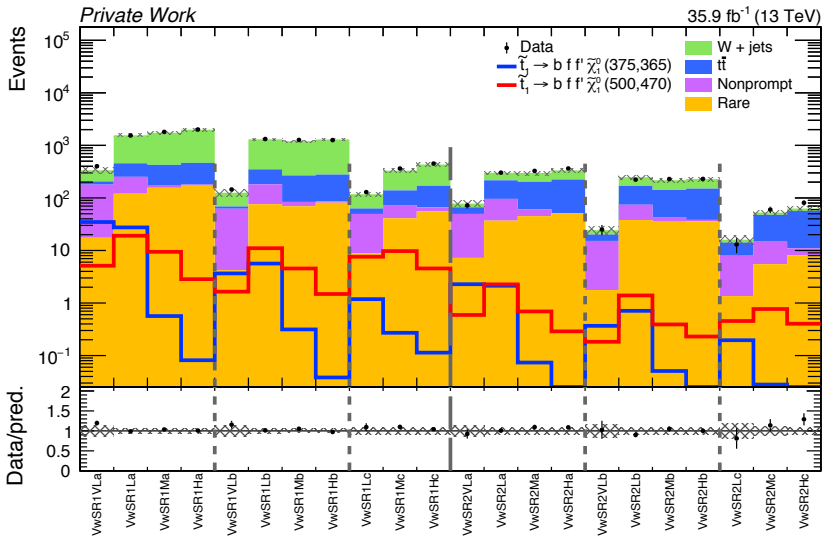

Figure 5.18: Validation of the background estimation method in the VW region ($200 < C_{\mathrm{T}} < 300\,\mathrm{GeV}$) is shown. The black dots represent the observed number of events with their statistical uncertainties, and the shaded areas are the combined systematic and statistical uncertainties of the prediction.

between SR and CR and not their absolute values. In other words, any effect changing the main backgrounds yields in a SR and the corresponding CR by the same factor would not have affect the final results.

W+jets and $\mathrm{t\bar{t}}$ lepton p_{T} shape differences

The normalization of the prompt contribution of W+jets and $\mathrm{t\bar{t}}$ backgrounds in the signal regions is estimated simultaneously from the high $p_{\mathrm{T}}(\ell)$ control regions and may therefore depend on the residual differences in the $p_{\mathrm{T}}(\ell)$ shapes of these backgrounds (Fig. 5.20). These differences are more dominant in large M_{T} regions where the $\mathrm{t\bar{t}}$ events are dominated by the dilepton decays of the top pair system. A conservative 20% upper limit for the variation in the cross section ratio of W+jets and $\mathrm{t\bar{t}}$ processes is assumed. The uncertainty due to residual differences in the $p_{\mathrm{T}}(\ell)$ shapes of W+jets and $\mathrm{t\bar{t}}$ is then estimated by propagating this variation in the scale factors used for obtaining the normalization of these backgrounds in the signal regions. These uncertainties are less than 1% in most regions but in some regions they can be as large as 2.2%.

Cross section uncertainty for rare SM processes

The contribution of the rare SM backgrounds in the signal and control regions of the analysis are typically small and have been estimated using simulation. A conservative cross section uncertainty of 50% has been set for these backgrounds.

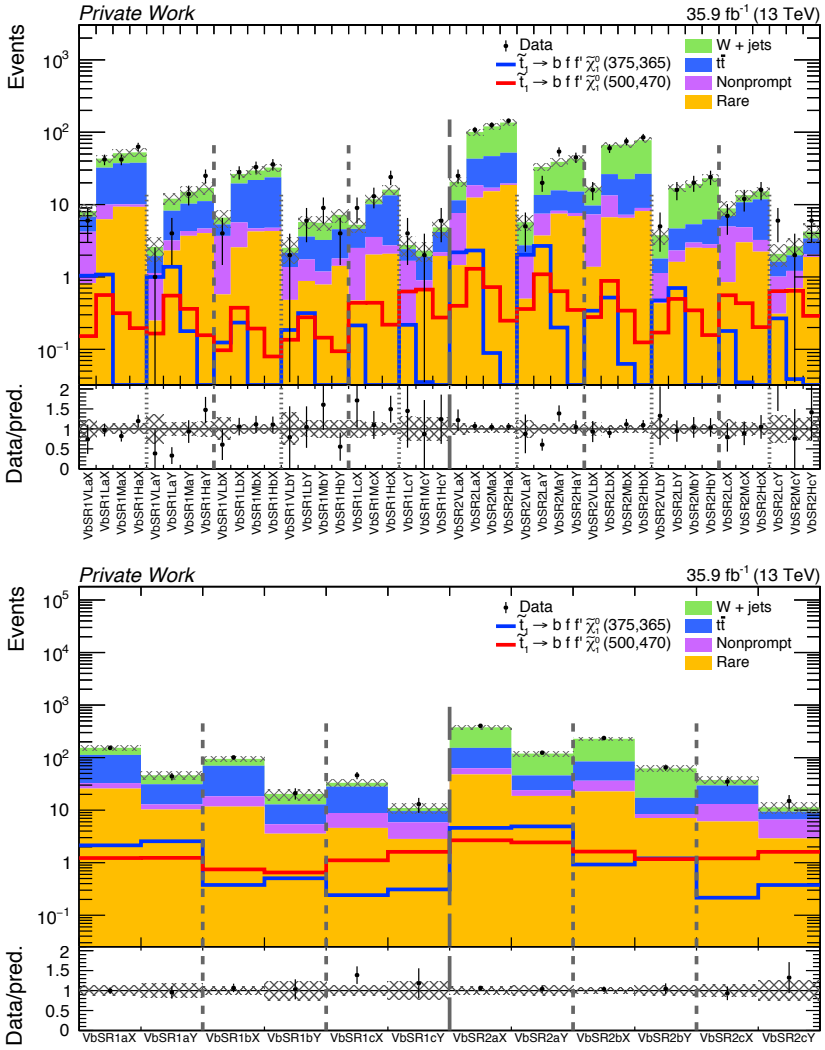

Figure 5.19: Validation of the background estimation method in the VB region ($N_{\mathrm{b}}^{\mathrm{hard}} \geq 1$) is shown in full (top) and with combined $p_{\mathrm{T}}(\ell)$ bins (bottom). The black dots represent the observed number of events with their statistical uncertainties, and the shaded areas are the combined systematic and statistical uncertainties of the prediction.

Uncertainties affecting the nonprompt background estimation

The estimated contributions of the nonprompt backgrounds in the signal and control regions are subject to additional uncertainties. For example, the measured tight-to-loose ratios may depend on the flavor of jets which the nonprompt leptons are associated to. In order to evaluate the dependence of ϵ_{TL}on the presence of b flavored jets, the tight-to-loose ratios are measured in separate samples enriched and depleted in b-tagged jets. This flavor dependence has a 20-50% effect on the values of ϵ_{TL}. Moreover, the consistency of the methods is checked by performing the nonprompt estimation using only simulated samples. The level of

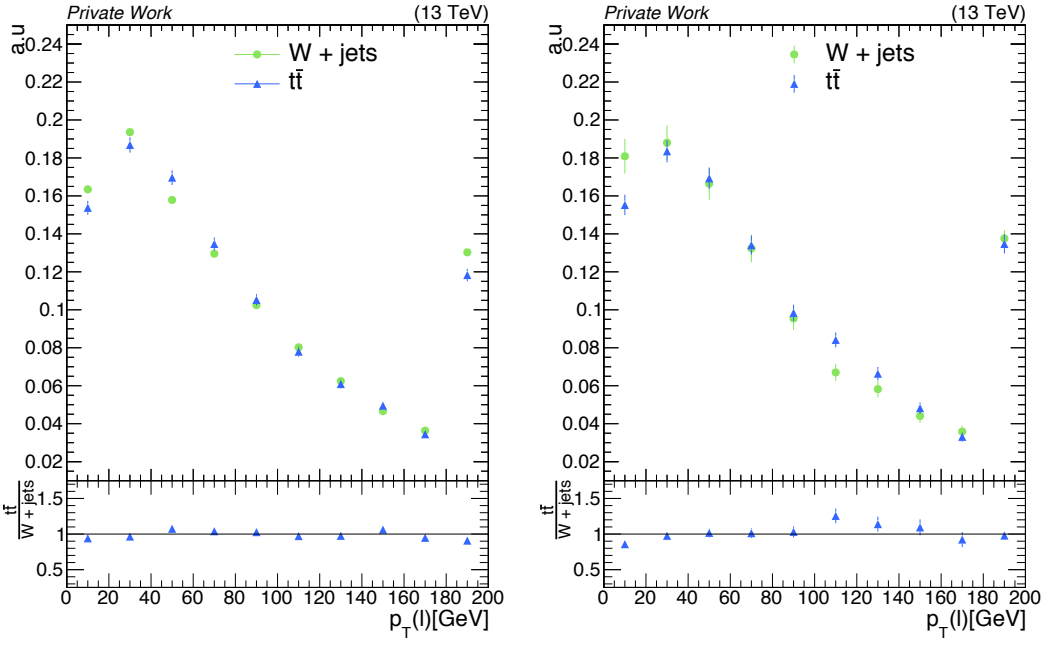

Figure 5.20: Comparison of the area normalized lepton p_{T} distributions of W+jets and $\mathrm{t\bar{t}}$ processes in SR1 (left) and SR2 (right).

agreement between the estimated and MC values in each region is considered as an additional source of systematic uncertainty. The effect of this non-closure uncertainty on the nonprompt background was seen to be negligible in many regions, however, in some regions the effect was observed to be as large as 200%. The regions with such a large non-closure uncertainties are typically highly dominated by prompt backgrounds, and therefore, the uncertainty on the nonprompt estimation has only very small effect on the total background estimation.

5.4.2 Common systematic uncertainties affecting background and signal simulated samples

ISR multiplicity

The correction factors applied on the simulated W+jets, $\mathrm{t\bar{t}}$ and signal samples are subject to additional uncertainties. For the $\mathrm{t\bar{t}}$ and signal samples the systematic uncertainty is taken as half of the correction factor while for W+jets the full size of the correction is taken as the systematic uncertainty. The uncertainty of the ISR corrections in W+jets ($\mathrm{t\bar{t}}$) sample with respect to the total background is 4.4-10.2% (less than 1%) in the signal regions. For the signal samples this uncertainty ranges between 5-7%.

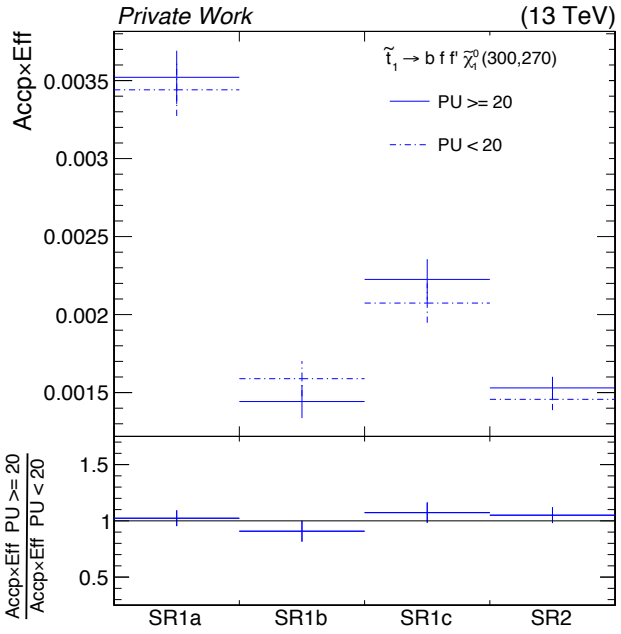

Figure 5.21: Comparison of the acceptance-times-efficiency for a four-body signal sample with $(m_{\tilde{t}},m_{\tilde{\chi}_1^0}) = (300,270)$ GeV after splitting the sample into events with smaller or greater than 20 interactions.

Pileup

The uncertainty due to the differences in pileup distributions of data and simulated samples is taken into account. The PU distribution in background samples is adjusted to match that of the one in data as described in Sec. 5.1.2. The corrected PU distribution in these samples is then varied within the uncertainties of the expected inelastic collision cross section (measured to be 5% [103]) resulting in total uncertainties ranging between 0.1% and 2%. Unlike the background samples, the signal samples were produced with a much lower average number of PU vertices, reducing the justification to simply correct for their PU distributions. However, the signal samples were checked to be insensitive to PU by splitting the test signal samples according to the number of interactions in the event and comparing the acceptance-times-efficiency of the two samples. An example of such a comparison is shown in Fig. 5.21 for splitting the sample into events with smaller or greater than 20 interactions. An uncertainty of 1% due to the PU distribution of the signal was estimated by comparing the normalized efficiencies of the split samples across all SRs.

JES and JER

The systematic uncertainties due to mismeasurements of jet energy scales (JES) in all simulated samples are calculated by varying the JECs (as described in Sec. 4.4.1) within one standard deviation. Additionally, the uncertainties due to jet energy resolution (JER) dif-

ferences between data and simulated samples are estimated by smearing the simulated jet momenta based on a Gaussian distribution with $p_{\mathrm{T}}(j)$ and $\eta(j)$ dependent width. The jet energies for each JES and JER variation are then used to calculate $p_{\mathrm{T}}^{\mathrm{miss}}$ and all other related quantities such as N_j,H_{T}, M_{T}, C_{T1} and C_{T2}. The corresponding JES systematic uncertainties for the background samples are estimated to be up to 2.1% and range between 3-4% for the signal samples.

b-tag efficiency and mistag probability

Since this analysis relies on the number of b-tagged jets for the categorization of signal regions, variations in the b-tag efficiency and mistag probabilities could shift events between signal regions. The uncertainties on the signal and background yields due to these effects is estimated by varying the b-tag scale factors (see Sec. 5.1.2) within uncertainties. The variations of the b-tag scale factors are evaluated separately for the light and heavy flavored jets. For the signal samples, additional correction factors which take into account differences in b-tagging between FastSim and FullSim are also varied within their uncertainties. The b-tagging uncertainties for the background processes are less than 1% in most regions while for signal this uncertainty can be as large as 3%.

Trigger efficiency

Possible biases in the trigger efficiency measurements (Fig. 5.4) are expected to be very small. An uncertainty of 1% is applied on signal and background estimations in the signal regions.

Lepton efficiency

The efficiency of the identification and isolation criteria for the leptons used in this analysis is measured in both data and MC samples as described in Sec. 5.1.2. The estimation of the main backgrounds in the signal regions is only affected by the differences between the lepton scale factors in the signal and control regions. In addition to the statistical uncertainties of the scale factors as seen in Fig. 5.7 which are applied to both signal and background processes, a flat uncertainty of 1% is applied on the background samples in order to account for the residual differences between the low and high $p_{\mathrm{T}}(\ell)$ scale factors. The signal sample is also subject to additional uncertainties due to the differences between the FastSim and full detector simulation. An additional 2% systematic uncertainty on the signal samples is applied in order to cover possible biases in FastSim scale factors and other effects the main backgrounds are insensitive to.

5.4.3 Systematic uncertainties on the signal prediction

Renormalization and factorization scales

The proper treatment of the infrared and ultraviolet divergences in cross section calculations requires introducing arbitrary scales referred to as factorization and renormalization scales. Including all perturbative orders in the cross section calculation must remove all dependencies on such arbitrary scales. On the other hand, the level of dependence of a fixed order calculation on these scales can give insights to the importance of the higher order terms which are ignored. In order to estimate the uncertainty due to this effect, the renormalization and factorization scales are each varied by different combinations of factors of 0.5, 1, and 2 while avoiding unphysical anti-correlated combinations. The envelope of the yields corresponding to the 8 possible combinations of these scales is used to estimate the uncertainty of the renormalization and factorization scales which is typically between 2-3% for the signal process.

Luminosity uncertainty

The integrated luminosity of the proton-proton beams colliding at the CMS during 2016 data taking was measured to be $35.9\,\mathrm{fb}^{-1}$ with an uncertainty of 2.5%. This uncertainty is applied to the signal yields in the SRs. The normalizations of the nonprompt backgrounds and the prompt component of W+jets and $\mathrm{t\bar{t}}$ events are obtained from data and therefore are not sensitive to the luminosity measurement. For the rare processes, the conservative uncertainty for their cross section is expected to also cover this effect.

Missing transverse energy modeling in FastSim

The FastSim modeling of the transverse missing energy is subject to additional corrections and uncertainties. The signal yields in analysis regions are estimated by averaging the yields obtained based on the reconstructed $p_{\mathrm{T}}^{\mathrm{miss}}$ and the generated $p_{\mathrm{T}}^{\mathrm{miss}}$. Half of the difference between the two quantities is then applied as the systematic uncertainty.

5.5 Results

The background estimation methods described in Sec. 5.3.1 for the prompt backgrounds and in Sec. 5.3.2 for the nonprompt backgrounds, accompanied with the simulation of rare processes is used to predict the expected number of background events in the signal regions. The scale factors for normalization of the prompt backgrounds in the SRs is obtained by performing a simultaneous maximum-likelihood (ML) fit in the control regions (CR-only). In other words, the free floating normalization of these backgrounds is linked between the SRs and CRs and its

Table 5.4: Typical ranges for the relative systematic uncertainties (in %) of the background and signal prediction in the main SRs. The background uncertainties are with respect to the total SM prediction.

Systematic uncertainty	Background SR1	Background SR2	Signal
Renormalization & factorization scales	n/a	n/a	2–3
Pileup	0.1–1.8	0.1–2.0	1
JES	1.2–2.1	0.1–1.4	3–4
JER	0.1–0.5	0.1–1.1	0–1
b-tagging	0.1	0.1–1.0	1–3
Trigger	0.0–0.1	0.0–0.1	1
Lepton efficiency	1.0–1.8	1.0–1.5	3
ISR ($t\bar{t}$ and signal)	0.1–0.5	0.1–0.8	5–7
ISR (W+jets)	4.5–10.2	1.9–4.4	n/a
$p_{\mathrm{T}}^{\mathrm{miss}}$ modelling (FastSim)	n/a	n/a	2–3
Relative yields W+jets/$t\bar{t}$	0.1–1.6	0.1–2.2	n/a
Nonprompt	1.0–4.6	1.0–9.5	n/a

value in the SRs is fixed by the CR-only fit. The observed number of events and the predicted SM contributions in each of the 44 signal regions are shown in Fig. 5.22. The observed number of events in the signal regions show no significant deviations from the predictions based on the background-only hypothesis. A detailed table with the individual contribution of the backgrounds and their uncertainties is shown in Fig. 5.5. The pull is defined by $\frac{N_{pred.}-N_{obs.}}{\sigma}$, where $N_{obs.}$, and $N_{pred.}$ are the observed and predicted number of events respectively and σ is the total uncertainty. The distribution of pulls and their values in each SR is shown in Fig. 5.23. The distribution of pulls for a random set of unbiased observations is expected to be a Gaussian with mean of 0 and width of 1, therefore deviations from these values could be indicative of the presence of various forms of biases. Despite the relatively small number of bins, and the fact that the measured pull values are not fully uncorrelated (due to SRs sharing common CRs), the distribution of the pulls is compatible with an unbiased pull distribution.

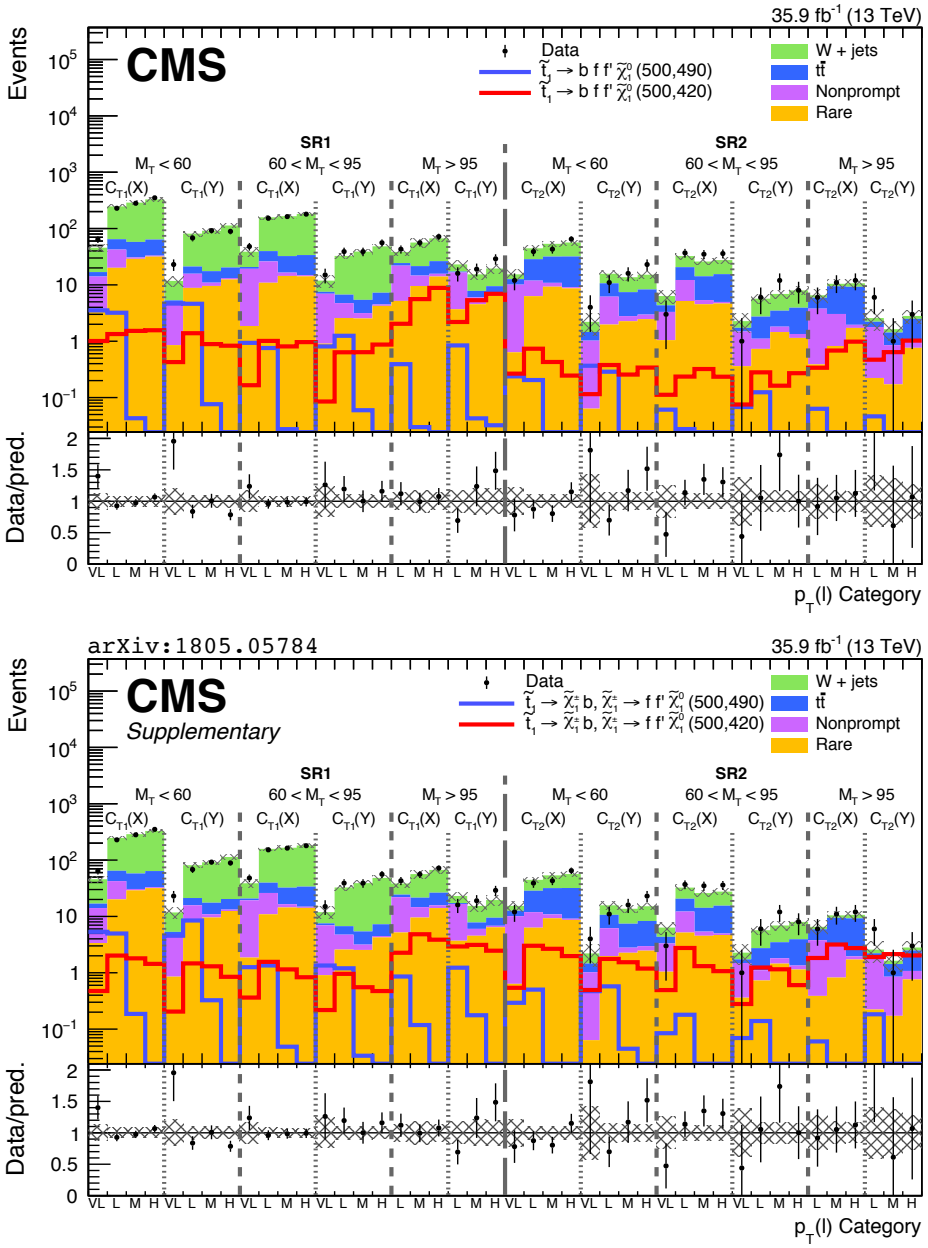

Figure 5.22: The expected background yields (filled histograms) and the observed (black dots) number of events in the analysis signal regions as defined in Tab. 5.2. The vertical lines and the shaded areas indicate the statistical uncertainty in data and the total uncertainty of the background predictions respectively [18]. The expected yields of the four-body and the chargino-mediated scenarios are shown on the top and bottom figures respectively.

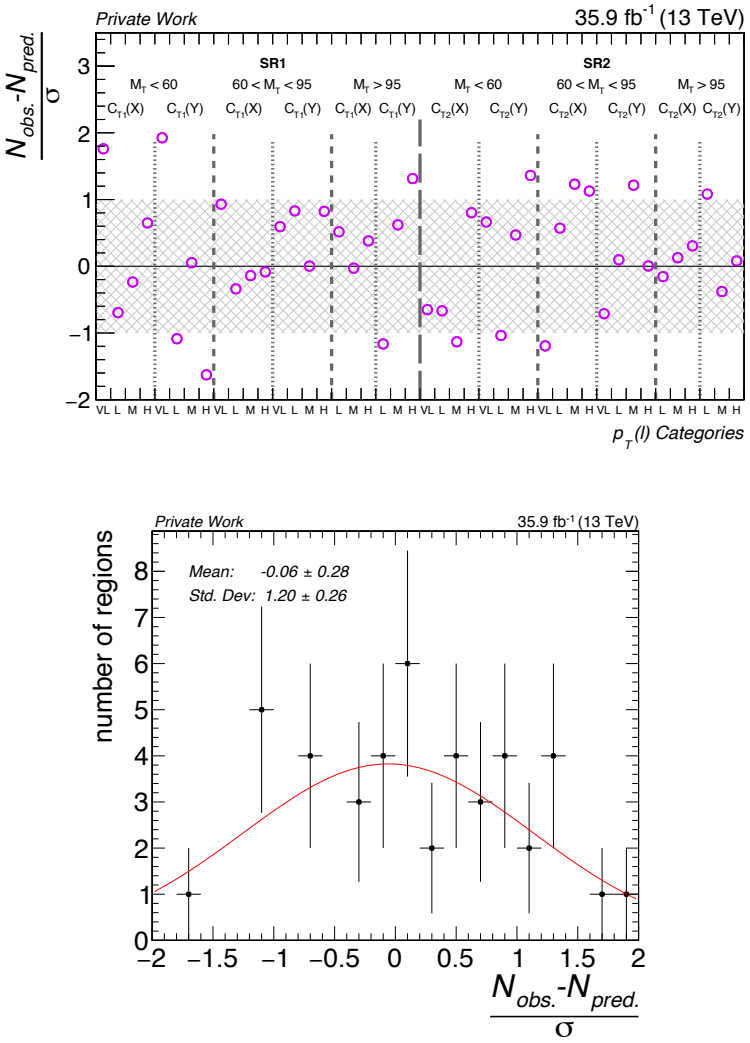

Figure 5.23: The top figure shows the the deviations of the predicted number of events with respect to the observed ones normalized to the total uncertainty (pulls) in each region. The bottom figure shows the distribution of the pulls.

Table 5.5: Summary of expected background and observed data yields in the signal regions. The uncertainties on the background prediction include the statistical and systematic sources.

Region	W+jets	$t\bar{t}$	Nonprompt	Rare	Total SM	Data
SR1VLaX	28.8±3.4	2.80±0.55	10.7±4.4	3.4±1.8	45.7±5.9	64
SR1LaX	182±14	22.4±3.6	22.2±8.7	20.1±9.7	247±21	229
SR1MaX	230±18	27.2±4.2	1.7±2.7	29±14	288±26	281
SR1HaX	265±20	30.8±4.8	1.3±2.4	32±15	329±28	351
SR1VLaY	6.44±0.97	0.60±0.21	3.9±2.1	0.85±0.56	11.8±2.4	23
SR1LaY	60.0±5.7	5.4±1.4	6.9±3.4	8.8±4.4	81.2±8.4	68
SR1MaY	73.7±6.7	6.6±1.6	1.4±2.8	9.6±4.7	91.3±9.2	92
SR1HaY	92.9±8.5	7.2±1.7	0.7±1.8	12.5±6.1	113±11	89
SR1VLbX	18.0±2.3	1.48±0.35	17.4±5.9	1.9±1.0	38.8±6.5	48
SR1LbX	118.4±9.1	13.7±2.2	15.2±6.0	10.9±5.6	158±13	152
SR1MbX	133.2±9.7	15.9±2.5	2.1±2.2	14.4±7.3	166±14	163
SR1HbX	148±10	18.9±2.9	0.7±1.1	14.2±6.9	182±14	180
SR1VLbY	4.37±0.80	0.57±0.19	6.1±2.6	0.91±0.61	11.9±2.8	15
SR1LbY	25.9±2.8	1.97±0.53	2.2±1.2	2.6±1.5	32.6±3.6	39
SR1MbY	33.6±3.5	2.26±0.62	0.6±1.2	2.5±1.4	39.0±4.1	39
SR1HbY	41.0±4.0	2.77±0.72	0.25±0.53	4.2±2.2	48.3±4.8	56
SR1LcX	14.0±2.3	2.46±0.59	16.7±3.9	5.2±2.8	38.4±5.5	43
SR1McX	34.8±8.5	6.9±1.4	5.1±1.8	9.6±4.9	56±11	56
SR1HcX	40.5±5.5	10.6±2.2	1.66±0.69	14.1±6.9	67±10	72
SR1LcY	5.8±1.3	0.64±0.25	12.9±3.2	3.7±2.1	23.1±4.1	16
SR1McY	7.5±1.5	1.81±0.63	1.47±0.78	4.5±2.6	15.4±3.3	19
SR1HcY	10.0±1.9	2.67±0.87	0.41±0.27	6.4±3.3	19.5±4.1	29
SR2VLaX	2.74±0.43	2.54±0.50	9.5±3.2	0.64±0.36	15.4±3.3	12
SR2LaX	16.0±1.7	16.7±2.2	5.6±2.0	6.3±3.0	44.6±4.9	39
SR2MaX	21.7±2.3	21.0±2.6	1.57±0.97	9.3±4.4	53.5±6.0	43
SR2HaX	24.6±2.6	22.8±2.9	0.44±0.49	8.7±4.1	56.5±6.2	65
SR2VLaY	0.75±0.17	0.44±0.17	0.96±0.90	0.064±0.041	2.21±0.94	4
SR2LaY	5.09±0.83	4.48±0.98	4.2±1.7	1.98±0.96	15.8±2.5	11
SR2MaY	6.2±1.0	4.64±0.96	0.53±0.53	2.3±1.1	13.7±2.0	16
SR2HaY	6.8±1.1	5.3±1.1	0.50±0.62	2.5±1.2	15.2±2.2	23
SR2VLbX	1.99±0.38	1.03±0.27	2.3±1.4	1.05±0.58	6.3±1.6	3
SR2LbX	11.9±1.7	8.4±1.3	7.0±2.2	5.2±2.5	32.5±4.3	37
SR2MbX	11.7±1.6	8.8±1.4	0.84±0.55	4.5±2.2	26.0±3.5	35
SR2HbX	12.0±1.7	10.5±1.6	0.30±0.38	4.7±2.2	27.6±3.7	36
SR2VLbY	0.55±0.15	0.24±0.10	1.13±0.80	0.36±0.26	2.27±0.87	1
SR2LbY	2.96±0.59	1.63±0.47	0.38±0.41	0.73±0.38	5.7±1.1	6
SR2MbY	3.42±0.68	1.67±0.47	0.36±0.4	1.45±0.73	6.9±1.3	12
SR2HbY	4.05±0.81	2.59±0.68	0.20±0.21	1.15±0.57	8.0±1.4	8
SR2LcX	0.62±0.22	2.1±0.5	3.4±1.7	0.39±0.26	6.5±1.8	6
SR2McX	1.00±0.29	6.4±1.2	2.2±1.3	0.82±0.45	10.5±1.9	11
SR2HcX	1.41±0.43	7.3±1.3	0.23±0.21	1.72±0.99	10.7±1.8	12
SR2LcY	0.36±0.27	0.44±0.21	1.56±0.97	0.22±0.18	2.6±1.1	6
SR2McY	0.207±0.080	0.58±0.25	0.68±0.52	0.17±0.12	1.64±0.62	1
SR2HcY	0.31±0.12	1.42±0.52	0.31±0.24	0.76±0.48	2.81±0.79	3

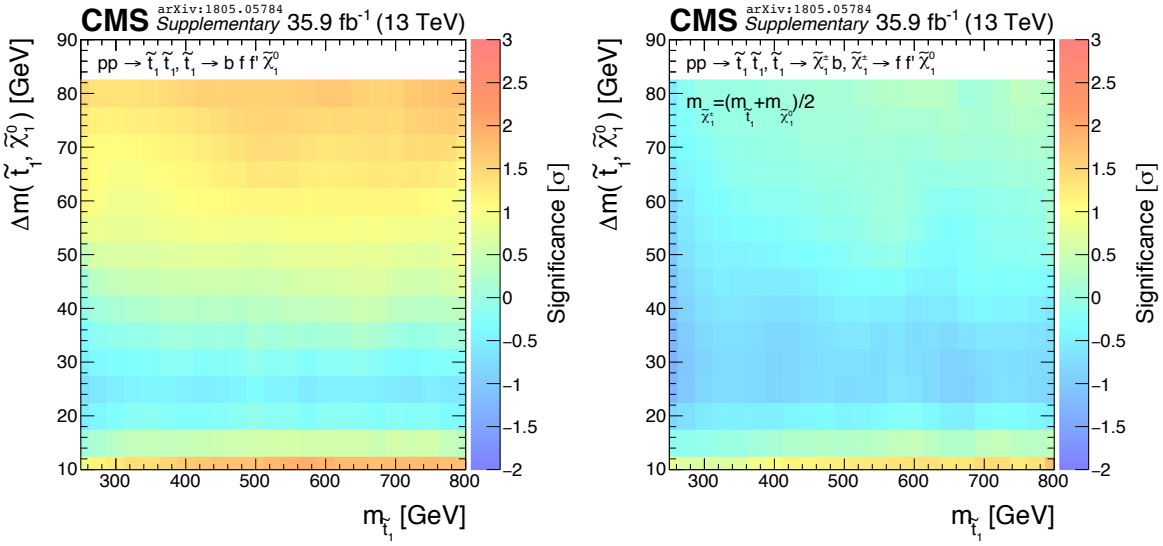

Figure 5.24: The observed significance for the four-body and chargino-mediated scenarios.

5.6 Statistical Interpretations

5.6.1 Statistical Methods

Given the compatibility of the observed and predicted values shown in Sec. 5.5, the results of the analysis are used to set constraints on the SMS parameter space, specifically the $m_{\tilde{t}}$-$m_{\tilde{\chi}_1^0}$ mass plane. Upper limits are set at 95% confidence level (CL) on the production of top squarks assuming 100% branching ratios for the four-body and chargino-mediated scenarios separately. The statistical methods used in this analysis is based on a modified frequentist approach (CLs method) [111, 112] which has been widely used by both ATLAS and CMS Collaborations. The parameter of interest is the *signal strength modifier* r, which is a multiplicative factor for the SUSY signal cross section. Various sources for systematic uncertainties affecting the background and signal processes, as described in Sec. 5.4, are taken into account by associating each source with a nuisance parameter, θ_i. The systematic uncertainties in this analysis are modeled by log-normal probability distribution functions (pdfs) of the form:

$$\rho(\tilde{\theta}|\theta) = \frac{1}{\sqrt{2\pi}\ \theta\ \ln\kappa} \exp\Big(-\frac{(\ln\theta/\tilde{\theta})^2}{2(\ln\kappa)^2}\Big) \tag{5.9}$$

where $\tilde{\theta}$ is the nominal value for the corresponding nuisance parameter, and κ is the parameter characterizing the width of the distribution. The log-normal distribution, unlike its normal counterpart, has the useful property of vanishing at zero which makes it a suitable pdf for positive definite observables such as cross sections and selection efficiencies. The signal and

background yields can then be written as a function of the nuisance parameters as $r \cdot s(\theta_i)$ and $b(\theta_i)$ respectively. The background-only and background+signal hypotheses are then characterized by $r = 0$ and $r > 0$ respectively. For a given observation (n) the likelihood function can be written in terms of the signal strength, r, and a nuisance parameter, θ, as:

$$\mathcal{L}(n|r,\theta) = Pois\big(n|r \cdot s(\theta) + b(\theta)\big) \cdot \rho(\tilde{\theta}|\theta). \tag{5.10}$$

More explicitly, the full likelihood function given the observations (data) across all signal and control regions and including all nuisance parameters can be written as:

$$\mathcal{L}(\text{data}|r,\theta) = \prod_{j}^{\text{SRs+CRs}} Pois\big(n_j|r \cdot s_j(\theta) + b_j(\theta)\big) \cdot \prod_{i}^{\text{nuisances}} \rho(\tilde{\theta}_i|\theta_i). \tag{5.11}$$

The compatibility of the data with the background-only and background+signal hypotheses is quantified using a test statistic. The test statistic condenses the full information of the search, including the observed number of events, the expected numbers of background and signal events and the associated uncertainties into one number which can be used to test the hypothesis.

In this analysis, along with majority of LHC experiments, a one-sided test statistic, $\tilde{q}_r$, based on the profile likelihood test statistic [111] is used:

$$\tilde{q}_r = -2\ \ln\left(\frac{\mathcal{L}(data|r,\hat{\theta}(r))}{\mathcal{L}(data|\hat{r},\hat{\theta})}\right), \quad 0 \leq \hat{r} \leq r, \tag{5.12}$$

where, $\hat{\theta}(r)$ is the value of the nuisance parameter which maximizes the likelihood for a given signal strength modifier r, and $\hat{r}$ and $\hat{\theta}$ are the values which maximize the likelihood globally. The constraint $0 \leq \hat{r} \leq r$ is imposed in order to avoid negative signal strengths and to ensure a one-sided confidence interval without excluding r values smaller than its best fit value. From Eq. 5.12 it can be noticed that $\tilde{q}_r$ values close to zero indicate the compatibility of the data for the given r value. Pseudo-data are generated using Monte Carlo methods according to Eq. 5.11 for the background-only and background+signal hypotheses and are then used to calculate their corresponding test statistics. The comparison of the observed test statistic with that of the background-only and background+signal hypothesis can then be used to set limits on the signal strength modifier.

The probability that the background+signal test statistic is at least as large as the ob-

served one is referred to as CL_{s+b} and is defined by:

$$\mathrm{CL}_{s+b} = \int_{\tilde{q}_r^{\mathrm{obs}}}^{\mathrm{inf}} f(\tilde{q}_r|r,\hat{\theta}_r)\mathrm{d}\tilde{q}_r. \tag{5.13}$$

where the pdf, $f(\tilde{q}_r|r,\hat{\theta}_r)$, is constructed by generating toy Monte Carlo pseudo-data using fixed nuisance parameter values obtained by fitting to data. The disadvantage of using this confidence interval is that in cases with a downward fluctuation of data, weak signals which the search should not be sensitive to, may be excluded. To protect against this feature, a modified frequentist CL_s criterion is defined based on the ratio of CL_{s+b} and CL_b:

$$\mathrm{CL}_s = \frac{\mathrm{CL}_{s+b}}{\mathrm{CL}_b}, \tag{5.14}$$

where the confidence level for the background-only hypothesis, CL_b is obtained in a similar way as CL_{s+b} but by using the appropriate test statistic in Eq. 5.13 and setting $r = 0$. Then a given r is said to be excluded at confidence level (1-α) if $\mathrm{CL}_s < \alpha$. Most searches typically choose the 95% confidence level ($\alpha = 0.05$) for setting upper limits. The 95% CL upper limit on r for a given signal strength is set by varying the signal strength modifier until $\mathrm{CL}_s = 0.05$ is reached. In the case of SUSY signals, since the cross section of the signals are fixed by the theory, the upper limit on the signal strength can then be translated to an upper limit on the cross section.

As described in the previous paragraph the calculation of the upper limits for each signal point can be quite CPU intensive. For a hypothesis test with relatively large number of bins and nuisance parameters this can become increasingly more time consuming. However, one major advantage of the profile-likelihood test statistic is that in the case of large data samples, the behavior of the CL_{s+b} and CL_b follow known analytical equations described in [111]. Instead of relying on large number of toy MC pseudo-datasets, this method takes advantage of an Asimov dataset, single representative dataset with its observed quantities exactly matching the predicted values. This asymptotic limit approximation approach removes the need for performing multiple MC trials and is therefore often the preferred method for calculating limits.

The profile likelihood ratio can also be used for quantifying a possible excess of observed number of events compared to the predicted values. In this case the test statistic is constructed

by setting $r = 0$ in Eq. 5.12 i.e:

$$\tilde{q}_r = -2 \ln\left(\frac{\mathcal{L}(data|0, \hat{\theta}(0))}{\mathcal{L}(data|\hat{r}, \hat{\theta})}\right), \tag{5.15}$$

Before attributing any excesses in observations to a possible signal scenario, the probability for upward fluctuations in background must be taken into account. The probability that the observed excess may caused by an upward fluctuation in the background-only hypothesis can be evaluated using the p-value:

$$p_0 = \int_{q_0^{obs}}^{\infty} f(q_0|0, \hat{\theta}_0) dq_0. \tag{5.16}$$

This p-value can be converted into a significance Z using a one-sided Gaussian tail, i.e.:

$$p = \int_{Z}^{\infty} \frac{1}{\sqrt{2\pi}} \exp(-x^2/2) dx, \tag{5.17}$$

which would yield a significance of 3σ (5σ) for a p-value of $1.35 \cdot 10^{-3}$ ($2.86 \cdot 10^{-7}$). Evaluating Eq.5.16, particularly for cases with a small p-value (large significance), can require a very large number of toy trials and therefore become computationally impractical. However, the asymptotic behavior of q_0 also provides a reliable approximation of the significance and it is much more practical to use the asymptotic approach for quantifying observed excesses.

The background-only hypothesis can also be tested without a specific signal model in mind. This test is called goodness-of-fit (GOF) test and is a useful check for consistency in case of no significant excesses. In this analysis, a GOF test based on a saturated algorithm is used in order to quantify the robustness of the background estimation method in the validation regions. Additionally, in order to ensure that the performance of the VRs would not be compromised in case of presence of signal, the GOF test is also performed after "injecting" signal events into the observed number of events. The summary of GOF tests for the nominal analysis regions and the validation regions are shown in Fig. 5.25 and Fig. 5.26, respectively.

5.6.2 Upper limits on the production of the top squark

The expected number of signal of events in each SR and CR is estimated using the full range of $m_{\tilde{t}}$-$m_{\tilde{\chi}_1^0}$ simulated signal samples. The 95% CL upper limits on the production of top squarks are set by assuming a 100% branching fraction for each model and by using the asymptotic

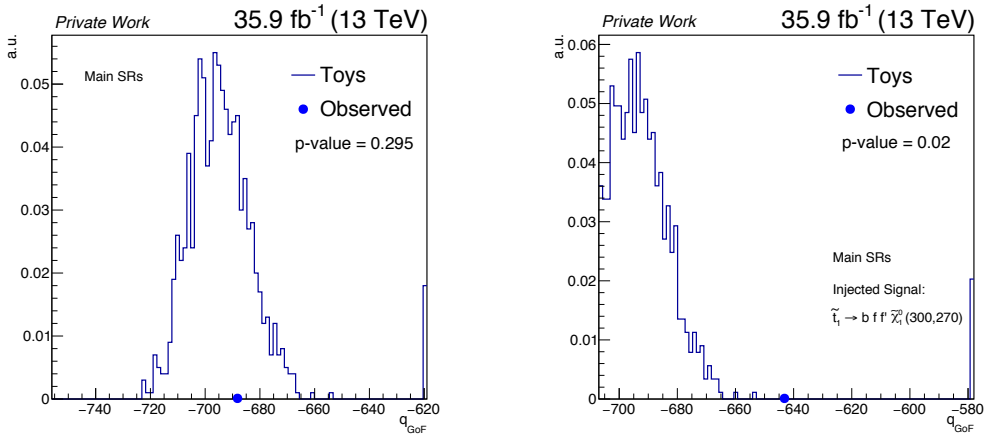

Figure 5.25: The goodness-of-fit test performed in the main regions. The plots on the left show the GOF test performed with the observed data and the plots on the right show the GOF test performed with the indicated signal added to the observed data in order to emulate the effect of presence of signal on the analysis.

CL_s criterion as described in the previous section. The colored maps in Fig. 5.27 show the 95% CL upper limit on the signal cross section for the four-body and the chargino-mediated models. The contour lines represent the observed and expected excluded mass limits which correspond to the point where the observed or expected signal strength-modifier r is equal to 1. The limits are shown in the $m_{\tilde{t}}$-Δm plane for better viewing.

The sensitivity of the signal points with smaller values of Δm ($\Delta m \lesssim 20\,\text{GeV}$) mostly relies on the very low $p_{\text{T}}(\ell)$ region of SR1 while signals with larger Δm ($\Delta m \gtrsim 50\,\text{GeV}$) benefit from the b-tag requirement of SR2 and larger C_{T} and M_{T} requirements. The search reaches its maximum sensitivity for signals with $20 \lesssim DM \lesssim 40\,\text{GeV}$ as signals in this Δm range can benefit from the kinematic properties of the full range of SRs. The excluded mass regions for the two signals have similar shapes due to the similar kinematics of the two scenarios. However, in the case of larger values of Δm, the excluded mass limits in the chargino-mediated scenario are stronger than the four-body case. This effect can be attributed to the topological features of the chargino-mediated scenario which allows for more energetic b-jets, leading to larger signal efficiencies in the SR2 categories.

5.7 Combination of soft single lepton (1ℓ) results with the all-hadronic (0ℓ) channel

In order to take full advantage of the available results of the CMS experiment in various final states, the results of this analysis have been statistically combined with those of the all-hadronic (0ℓ) channel [113] involving the same SMS topologies. The all-hadronic analysis

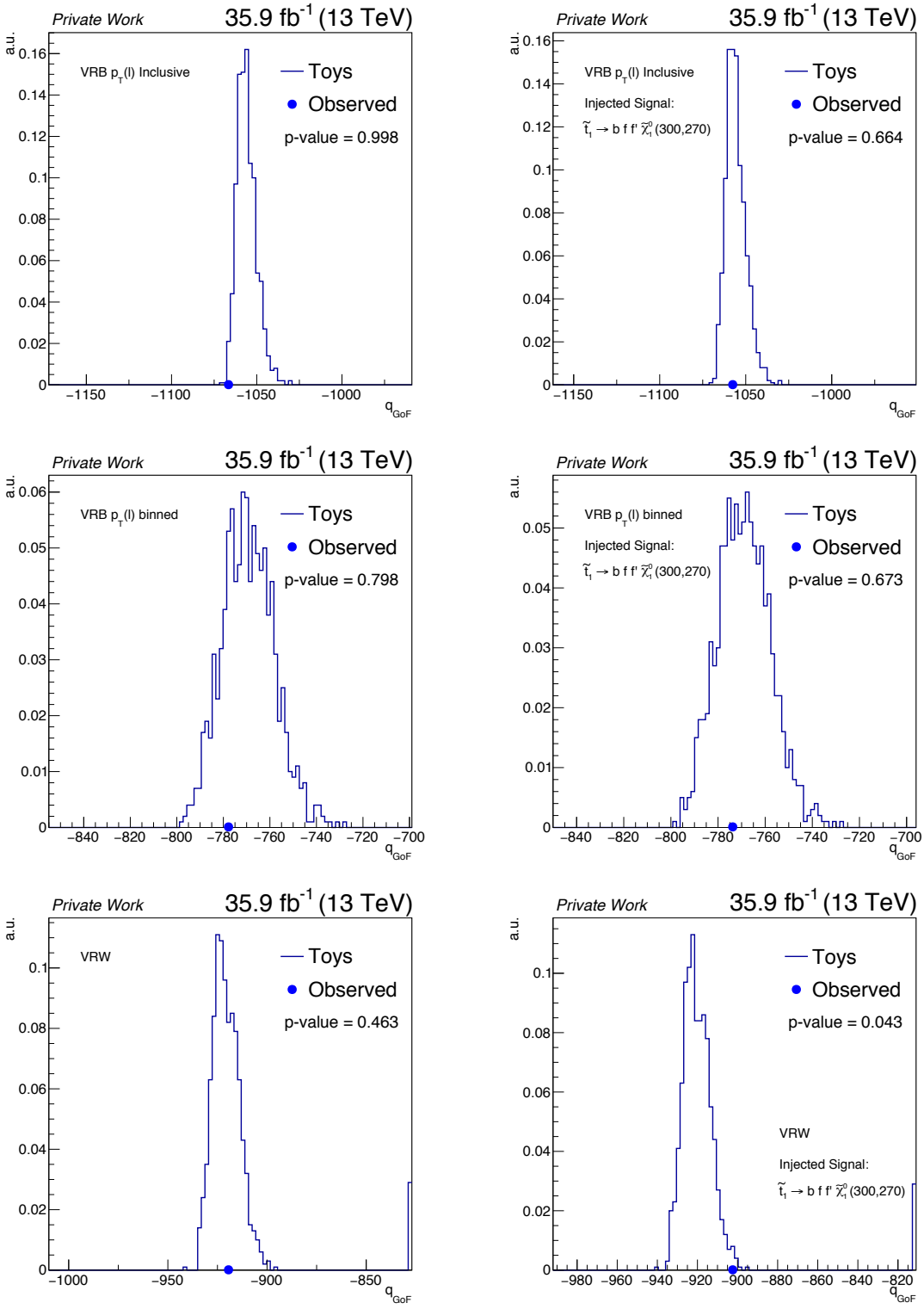

Figure 5.26: The goodness-of-fit test performed in the validation regions: VRB inclusive in $p_{\mathrm{T}}(\ell)$ (top), VRB binned in $p_{\mathrm{T}}(\ell)$ (middle), VRW (bottom). The plots on the left show the GOF test performed with the observed data and the plots on the right show the GOF test performed with the indicated signal added to the observed data in order to emulate the effect of presence of signal on the validation methods.

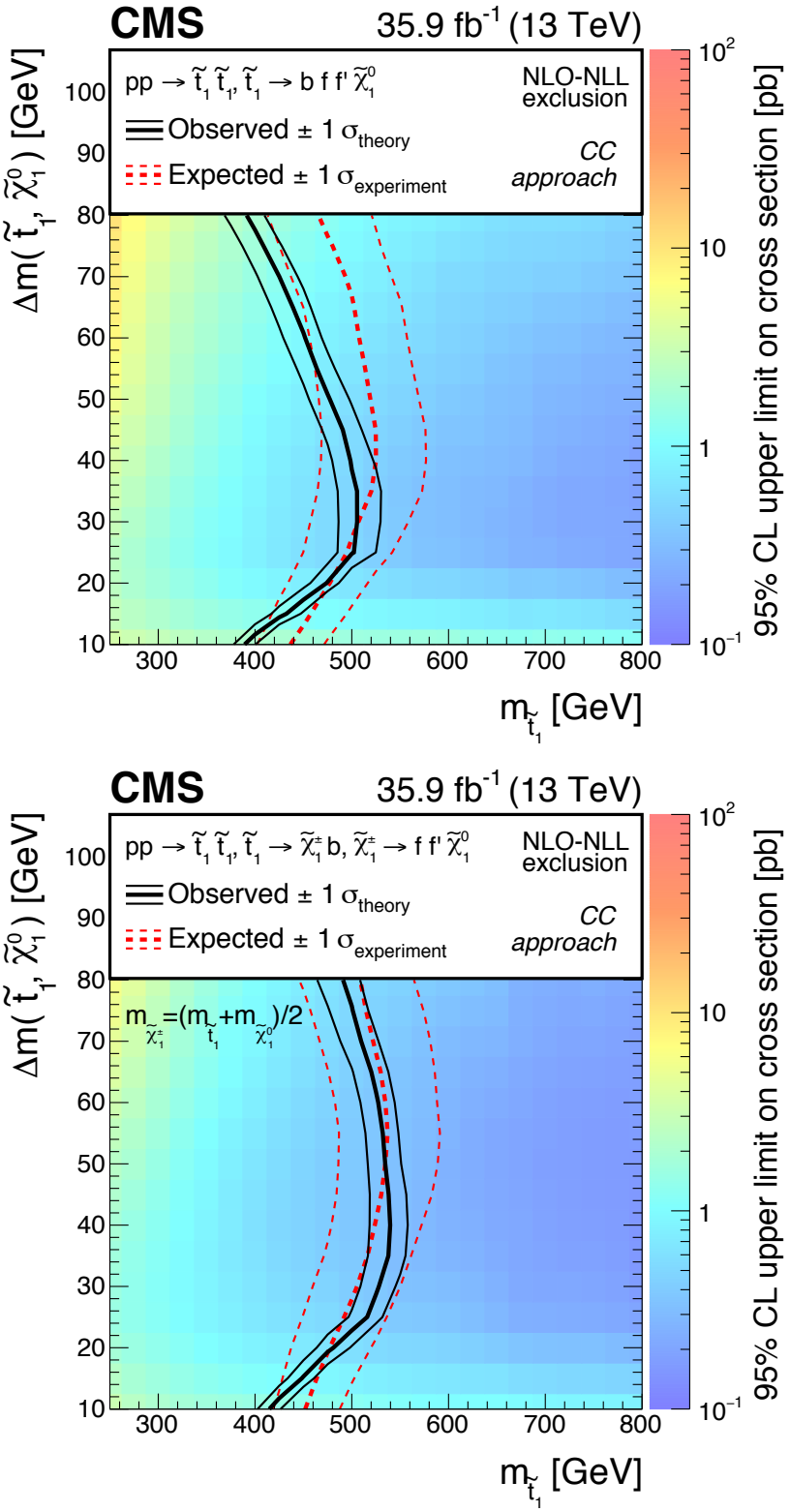

Figure 5.27: Exclusion limits at 95% CL for the four-body decay (left) and chargino-mediated (right) decay of the top squark on the $m_{\tilde{t}}$-Δm ($m_{\tilde{t}}$,$m_{\tilde{\chi}_1^0}$) plane. The color shading represents the observed cross-section limits. The uncertainty of the observed exclusion limit is derived based on the expected uncertainty of the top squark pair production cross section [18].

is an inclusive search for the pair production of top squarks in all-jet final states with search regions kinematically orthogonal to single leptonic regions used in the analysis described in this thesis. However, due to slight variations in the selection criteria (particularly identification and isolation) of the leptons in the two analyses, small overlaps between the two searches can exist. For instance, events selected by the *1ℓ* analysis may fail the lepton veto of the *0ℓ* search. Moreover, the *0ℓ* analysis also relies on single lepton control regions in order to estimate the contribution of events with a prompt lepton in which the lepton is not properly reconstructed or identified (lost-lepton background). These lost-lepton control regions can also have kinematical overlaps with the *1ℓ* regions. Since these control regions have been included in the calculation of the upper cross section limits for in the *0ℓ* analysis, the effects of their possible overlaps with the *1ℓ* regions must be investigated. The data events passing the selection criteria of the two analyses have been used in order to quantify the level of overlap between the two searches. The relative overlaps between the two analyses, defined by the number of overlapping data events normalized to the average size of the *0ℓ* and *1ℓ* regions, are shown in Appendix A.2.It can be seen that this relative overlap is below a few percent in most cases. In order to make sure the correlations between the two analyses are negligible, multiple checks were made by performing the combination after removing individual regions with larger overlaps from the combination which showed no impact on the combined results. Moreover, the correlations between the common systematic uncertainties affecting the two analyses are taken into account. The combined limits of the *0ℓ* and *1ℓ* channels are shown in Fig. 5.28 for the four-body and chargino-mediated scenarios. The combined results extend the expected $m_{\tilde{t}}$ exclusion limits by up to 50 GeV and improve the cross-section upper limits by 20%-30% in the four-body scenario.

0ℓ Region	Number of events in overlapping *0ℓ* regions	*1ℓ* Region	Number of events in overlapping *1ℓ* regions	$N_{\text{overlap}}^{0\ell\text{-}1\ell}$	Figure for relative overlap
CR	15603	SR	1975	309	Fig. A.5
CR	14185	CR	8625	641	Fig. A.6
SR	6728	SR	856	31	Fig. A.7
SR	149	CR	451	1	Fig. A.8

Table 5.6: Summary of number of overlapping events between the *0ℓ* and *1ℓ* SRs and CRs.

5.8 Summary of CMS SUSY results

The 2016 data collected at CMS have been studied by numerous complementary analyses to search for various SMS scenarios 5.29. The results obtained in the search described in this

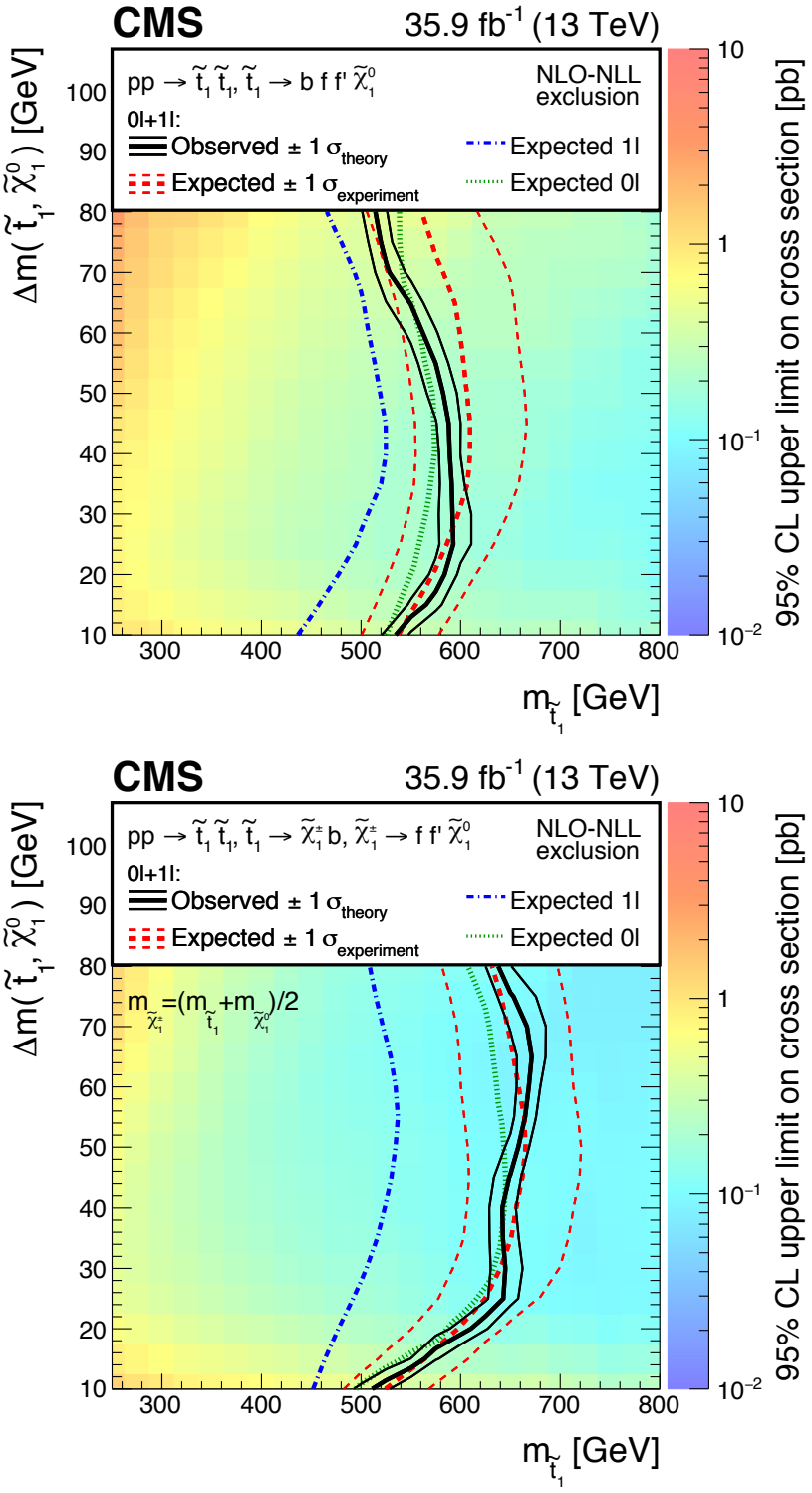

Figure 5.28: Combined limits at 95% CL between the single-lepton (1ℓ) and all-hadronic (0ℓ) searches for the four-body decay (left) and the chargino-mediated decay (right) of the top squark in the $m_{\tilde{t}}$-Δm ($m_{\tilde{t}}$,$m_{\tilde{\chi}_1^0}$) plane. The colour shading corresponds to the observed limit on the cross section. The solid black (dashed red) lines show the observed (expected) mass limits, derived using the expected top squark pair production cross section. The thick lines represent the central values and the thin lines the variations due to the theoretical (experimental) uncertainties. The dot-dashed blue and dotted green lines show the individual expected mass limits for the 1ℓ and 0ℓ searches, respectively [18].

thesis provide the most stringent limits on the top squark mass in the compressed region as seen in Fig. 5.30. Other decay scenarios of the top squark, for example in less compressed regions, have also been investigated by several other CMS analyses. A selected few of these CMS analyses involving the direct decay and chargino-mediated decays of the top squark are shown in Fig. 5.31.

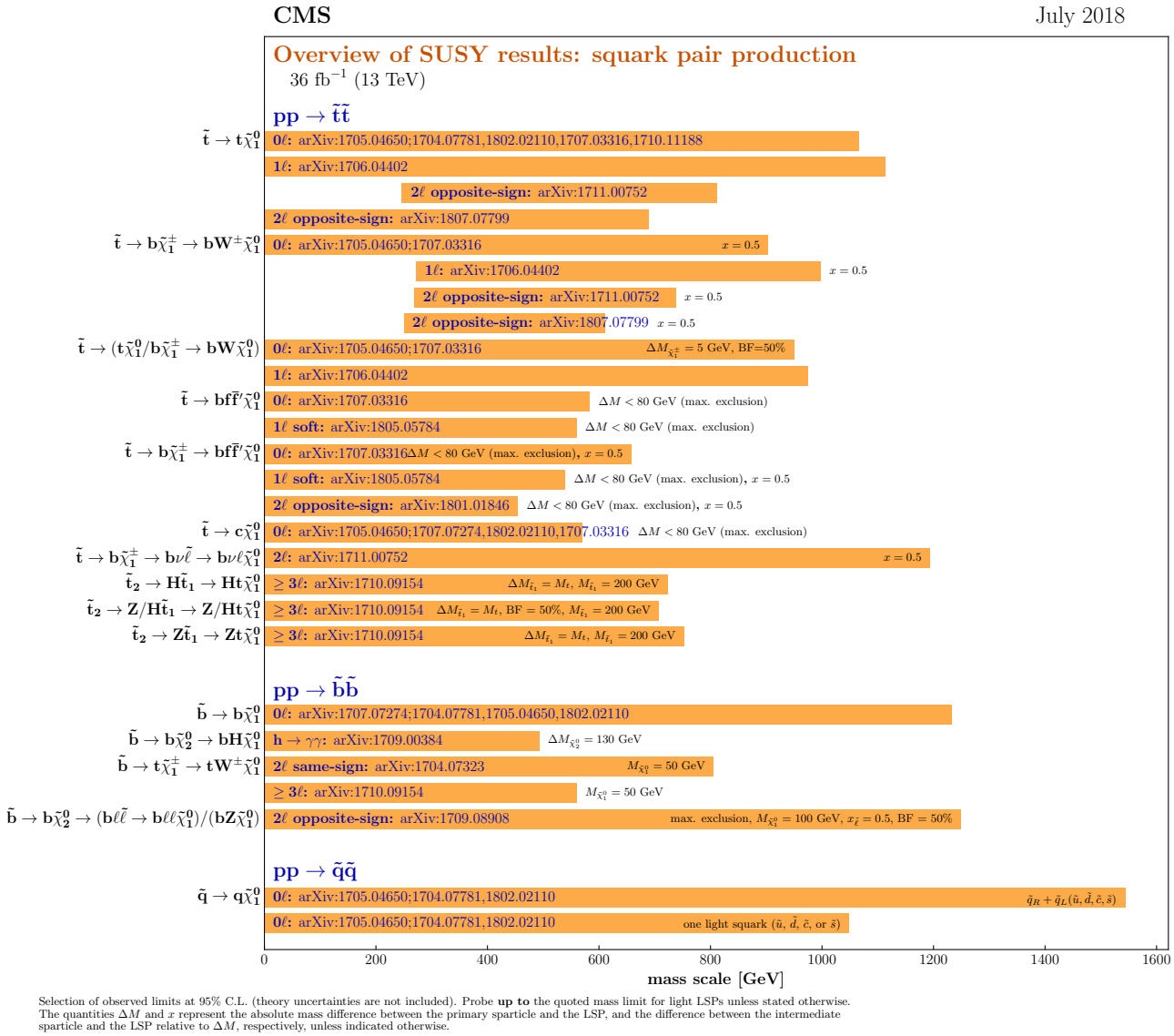

Figure 5.29: Summary of the best exclusion limits (as of July 2018) on squark masses in various SMS scenarios obtained by CMS SUSY searches [114].

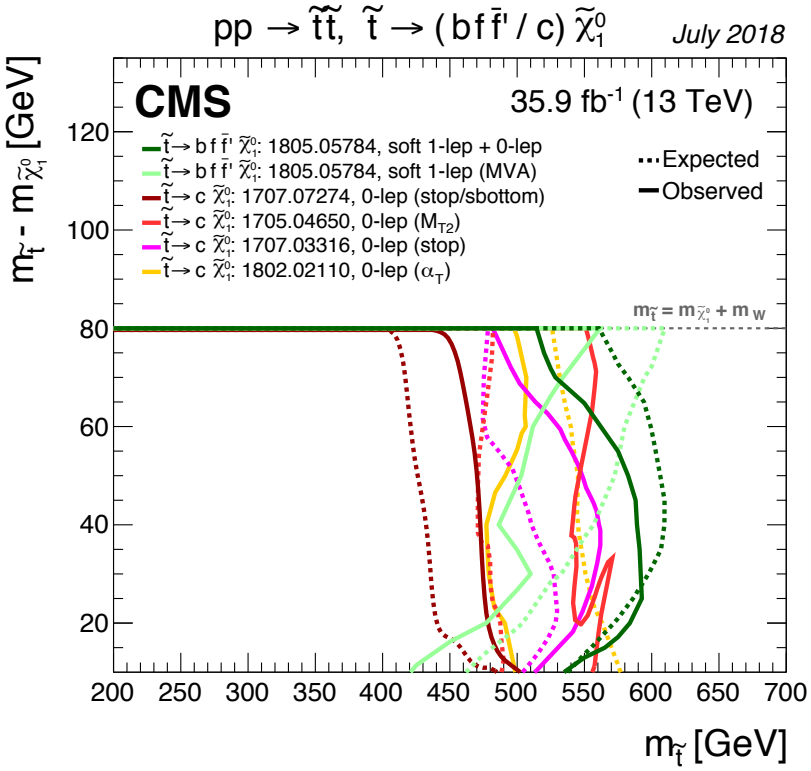

Figure 5.30: Observed and expected mass limits of various CMS SUSY searches sensitive to the four-body and FCNC decays of the top squark in the compressed region [114].

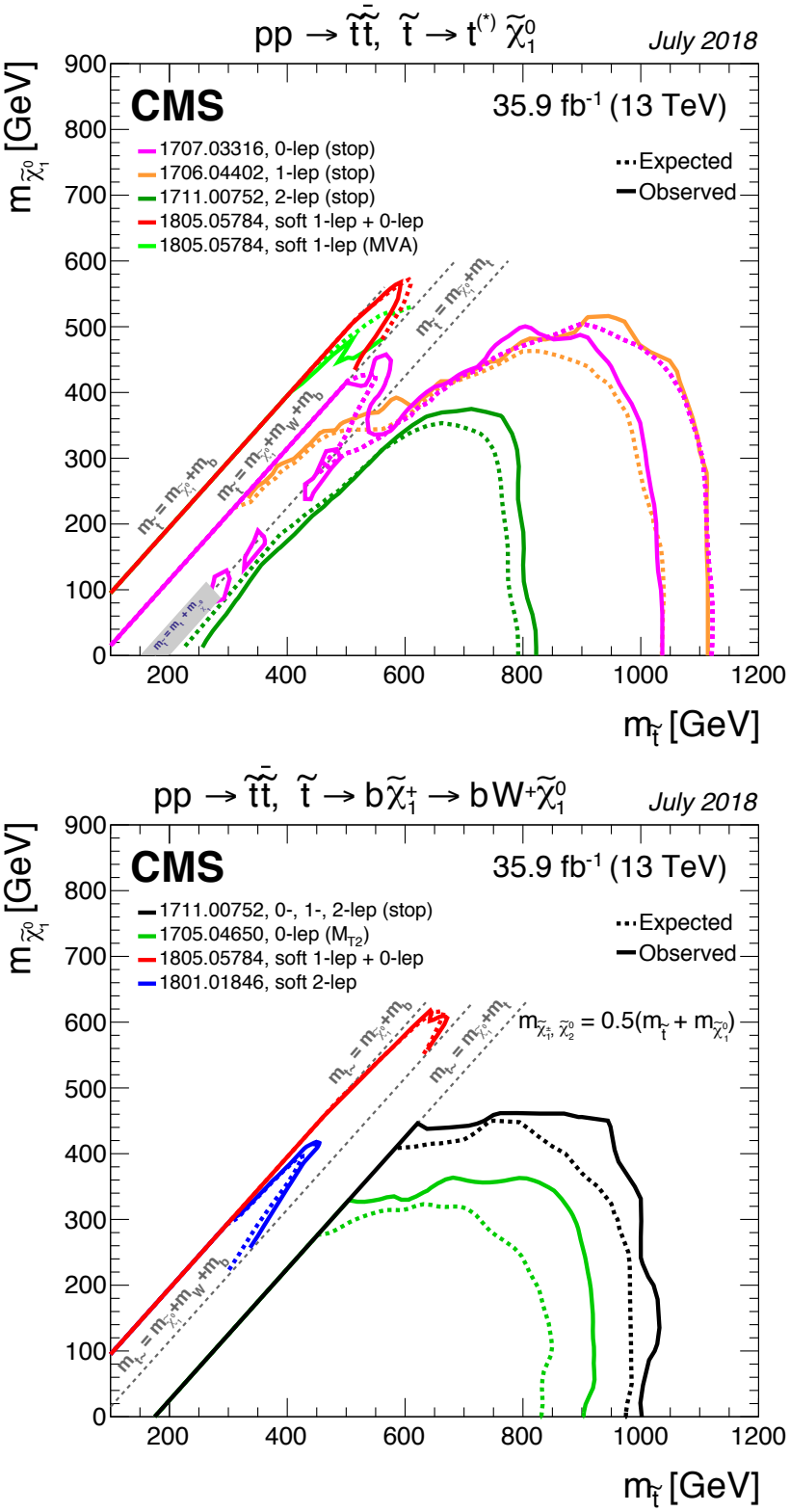

Figure 5.31: Observed and expected mass limits for the direct decay (top) and chargino-mediated (bottom) decays of the top squark shown in the $m_{\tilde{t}}$-$m_{\tilde{\chi}^0_1}$ mass plane [114].

5.9 Outlook

Run II luminosity projections and low cross section signal scenarios

The data collected at the CMS detector is expected to reach a total integrated luminosity of around 150 fb^{-1} by the end of the Run II data taking period. This amounts to more than four times the data collected during the 2016 data taking period. This substantial increase in the size of the dataset opens new possibilities for improving the sensitivity of new physics searches. Fig. 5.32 shows the expected cross section upper limits extrapolated to a 150 fb^{-1} dataset for the four-body and chargino-mediated scenarios. The projected limits are obtained by scaling the expected signal and background yields according to the increase in the luminosity. The relative systematic and statistical uncertainties for the simulated samples are assumed to stay constant. The increase in the luminosity may also make it possible for this analysis to gain

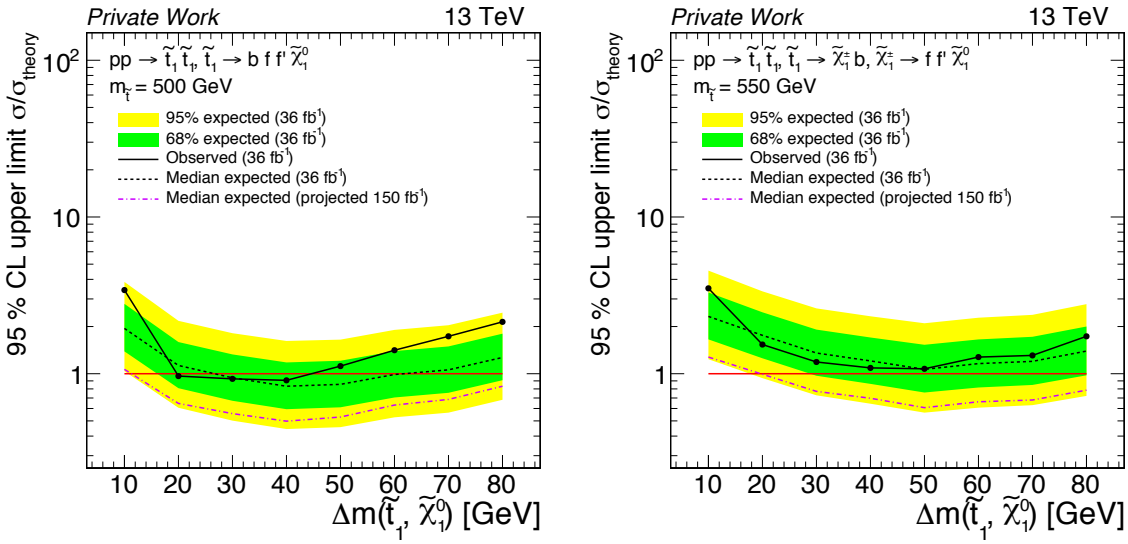

Figure 5.32: Expected and observed upper limits for the four-body (left) and chargino-mediated (right) scenarios with the indicated top squark masses. The projected expected limits corresponding to an integrated luminosity of 150 fb^{-1} are shown as the dashed-dotted purple lines.

sensitivity to signal processes which are currently beyond the reach of the search. In particular SUSY scenarios involving the production of neutralinos and charginos (collectively referred to as "electroweakinos") with small mass gaps between the SUSY particles may result in final states with one or more soft leptons and could have the potential to be constrained by the signal regions of this analysis. However, the production cross sections of electroweakinos at LHC are typically much smaller than those of top squarks which makes searches for these particles much more elusive. The gain in the integrated luminosity achieved by the end of Run II can provide the extra boost needed to probe these hard-to-reach regions of the SUSY parameter space. In particular, the analysis was found to have potential sensitivity to two

models which are described below.

First, an additional SMS electroweakino scenario is considered where the pair production of mass degenerate neutralinos and charginos ($\widetilde{\chi}_1^{\pm}$-$\widetilde{\chi}_2^0$) is followed by their decay into an LSP and offshell Z and W bosons ($pp \to \widetilde{\chi}_2^0 \widetilde{\chi}_1^{\pm}$, $\widetilde{\chi}_2^0 \to \mathrm{Z}^* \widetilde{\chi}_1^0$, $\widetilde{\chi}_1^{\pm} \to \mathrm{W}^* \widetilde{\chi}_1^0$). The mass difference between the $\widetilde{\chi}_1^{\pm}$ and the LSP is assumed to be between 3.5 and 50 GeV and the simulated signal samples are produced in a similar fashion as the top squark signal samples of the analysis. The production cross sections are calculated at NLO+NLL and assuming a pure wino state for the mass degenerate electroweakinos [115, 116].

Moreover, the sensitivity of the analysis was checked in a phenomenological minimal supersymmetric model (pMSSM) [117], where the parameters of interest are the higgsino (μ) and bino (M_1) masses. The wino mass (M_2) is set to $M_2 = 2M_1$ in order to reduce the parameter space and the ratio of the vacuum expectation values of the MSSM Higgs doublets, $\tan(\beta)$, is set to 10. All the other mass parameters are assumed to be decoupled in this model. The values for these parameters are largely inspired by GUT unification and naturalness arguments. In this "higgsino pMSSM" scenario, the NLO cross sections, the decay and the mass spectra of the SUSY particles are calculated based on the methods described in [118].

Although the nominal analysis based on the 2016 CMS data did not show a substantial sensitivity to either of the two models, the additional data collected during 2017 and 2018 may allow for the exclusion of parts of the parameter spaces in these scenarios. The upper limits corresponding to the electroweakino and higgsino pMSSM scenarios for a few of the most sensitive mass configurations are shown in Fig. 5.33. The sources of systematic uncertainties affecting these signal models are taken into account.The expected limits are calculated at 95% CL interval using the methods as described in Sec. 5.6.1. The expected limits are extrapolated to 150 fb^{-1} by performing the limit calculation after scaling the background and signal yields according to the increase in the luminosity while keeping the relative uncertainties constant. The extrapolated limits corresponding to a luminosity of 150 fb^{-1} indicate that a simple "rerun" of the analysis on the full Run II data can only result in relatively small regions of these mass planes to be excluded.

Nevertheless, the higher statistical power of a larger dataset can open doors for additional improvements and optimizations of the analysis which may have significant effects on the sensitivity of the search. For instance, the effects of additional categories in the C_T and M_T variables on the sensitivity to the signal scenarios should be investigated for the analysis of the full Run II data. Since these signal samples are expected to have lower hadronic activity and smaller amount of missing transverse energy than the main signal processes of the analysis, lowering the H_T and $p_\mathrm{T}^\mathrm{miss}$ thresholds in the signal regions can also improve the sensitivity to these signals. A preliminary investigation showed that including an additional set of signal

regions with the requirement of $200 \leq C_{\mathrm{T}} < 300\,\mathrm{GeV}$ can lower the expected upper limit of these signals by up to 25%. However, lowering the requirement on C_{T} implies having a lower $p_{\mathrm{T}}^{\mathrm{miss}}$ threshold and since the $p_{\mathrm{T}}^{\mathrm{miss}}$ based triggers are not fully efficient below 300 GeV (see. Fig. 5.4), a set of dedicated triggers have been developed by the analysis group [119] and added to the L1 and HLT trigger menus. Besides the requirements on the $p_{\mathrm{T}}^{\mathrm{miss}}$, these new triggers also require the events to include a muon with $p_{\mathrm{T}} > 3\,\mathrm{GeV}$ and a jet with $p_{\mathrm{T}} > 100\,\mathrm{GeV}$, where the muon and the jet are reconstructed at the HLT level. These new conditions allow for the $p_{\mathrm{T}}^{\mathrm{miss}}$ threshold to be lowered down to 80 GeV, while maintaining a relatively an acceptable firing rate for the trigger.

Top squark lifetime

As mentioned in Sec. 5.1, the lifetime of the top squark is assumed to be zero in the simulated signal samples used in this analysis. It has been noted, however, that in the four-body decay scenario and for smaller values of Δm, e.g. $\Delta m \lesssim 30\,\mathrm{GeV}$, the decay width of the top squark can become large enough to invalidate the zero lifetime assumption [52]. In these cases, the proper decay length of the top squark could range from a few centimeters to more than a meter. Dedicated studies must be performed in the future versions of the analysis in order to investigate the effects of these nonzero lifetimes. As a first step, an interpretation of the nominal analysis can be performed on the four-body signal simulations which include various lifetime scenarios for the top squark. Even more dedicated investigations can be performed in order to take advantage of exotic signatures such as displaced vertices for leptons and jets or anomalously heavy tracks that could be created depending on the lifetime of the top squark. A metastable top squark could also form a color-singlet state with quarks and gluons, a state known as an R-hadron which may or may not be electrically charged. Searches involving these topologies are often background-free since such processes do not typically occur in SM and therefore an optimized search can vastly improve the sensitivity to the signals in these kinematic regions. On the other hand, these nontraditional signatures require dedicated reconstruction and identification techniques which may also have some degree of model dependence. Some examples of searches within the CMS Collaboration investigation similar topologies can been found in [120–122].

Soft b-tagging

The b jets used in this analysis have a minimum p_{T} threshold of 30 GeV; however, as seen in Fig. 5.34, a large fraction of b quarks produced in the signal processes can have p_{T} values below this threshold. Successful attempts have been made in other CMS analyses [113, 123] to identify soft b quarks based on the presence of a secondary vertex in the event. Including similar soft b-tagging methods in this analysis can provide new ways to discriminate between

the signal and background processes. Additional requirements can be imposed on the reconstructed SVs in order to suppress the light-quark background. These requirements include parameters such as the distance and the significance of the distance between the SV and the primary vertex, the number of tracks associated to the SV, and the total p_{T} of the tracks associated to the SV. Figure 5.35 shows the comparison of the selected SV multiplicities (N_{SV}) in the signal and the dominant background processes after applying the quality criteria for the SVs and the kinematic selections corresponding to SR1 (see Tab. 5.1). It can be seen that the region satisfying $N_{\mathrm{SV}} = 0$ contains the majority of the background events, suggesting that creating a set of orthogonal SRs which satisfy $N_{\mathrm{SV}} \geq 1$ may provide additional sensitivity to the signal processes. More in depth studies have to be performed in order to design and estimate the expected sensitivity of the new set of SRs and also to ensure the validity of the background estimation methods of the analysis in the new kinematical regions.

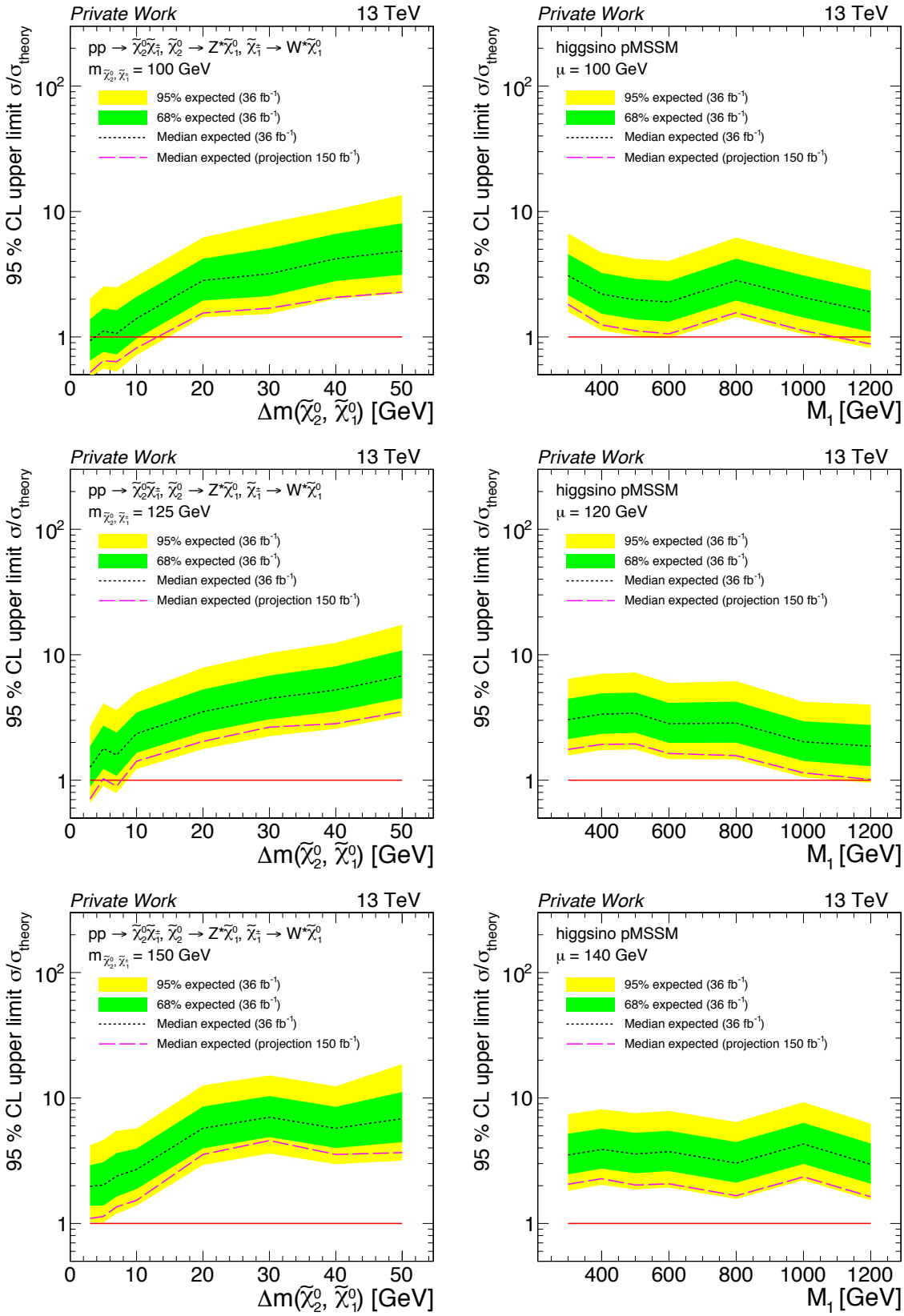

Figure 5.33: Expected upper limits for the electroweakino production (left) and pMSSM higgsino (right) models with the indicated SUSY particle masses. The projected expected limits corresponding to an integrated luminosity of 150 fb^{-1} are shown as the dashed magenta lines.

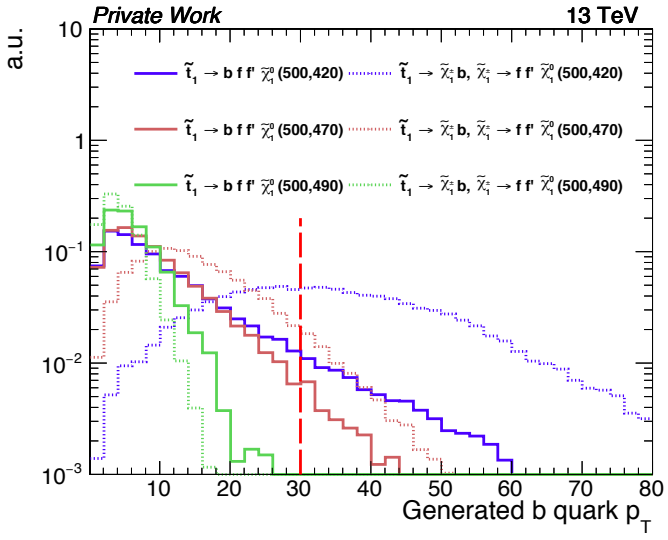

Figure 5.34: The p_T distribution of generated b quarks are shown in the four-body (solid lines) and the chargino-mediated (dotted lines) scenarios for a few Δm cases.

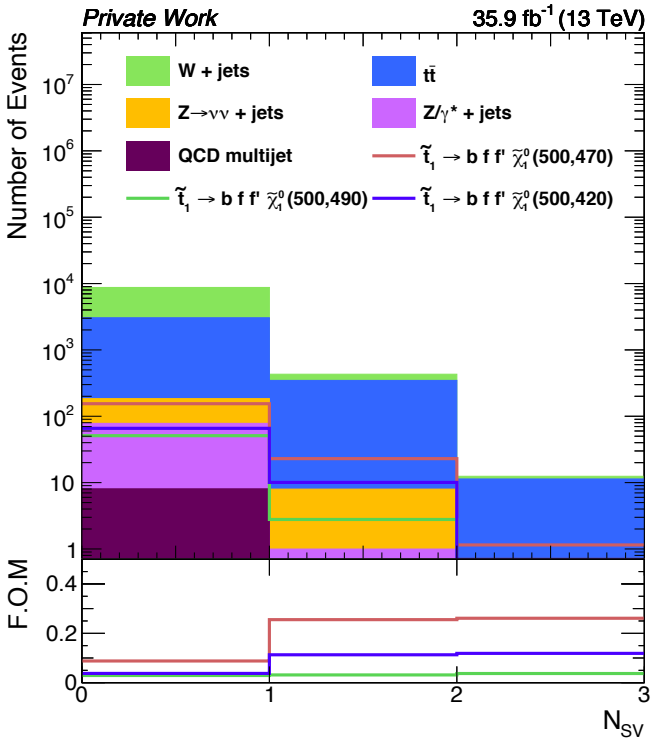

Figure 5.35: The SV multiplicity distribution is shown for the few signal scenarios and the dominant backgrounds.

Conclusions

In this thesis, an analysis of the proton-proton collision data collected by the CMS detector during the 2016 data taking period of the LHC has been presented. The topic of the analysis is a search for the pair production of top squarks in supersymmetric scenarios where the mass difference between the top squark and the LSP is less than the W boson mass. In particular the single lepton channel of the four-body and the chargino-mediated decays of the top squark are investigated. The analysis exploits the soft lepton p_{T} spectrum of the signal processes in this compressed region, by defining the signal regions as events satisfying $p_{\mathrm{T}}(\ell) \leq 30\,\mathrm{GeV}$ and using events with $p_{\mathrm{T}}(\ell) > 30\,\mathrm{GeV}$ to obtain the normalization of the dominant backgrounds (W+jets and $\mathrm{t\bar{t}}$) in the signal regions. The contribution of nonprompt sources of leptons in the signal and control regions are estimated directly from data. The robustness of background estimation methods is checked by performing the full estimation method in several validation regions orthogonal but kinematically similar to the nominal regions of the analysis. Assuming a 100% branching ratio for each of the decay scenarios, top squark masses of up to 500 and 540 GeV are excluded at 95% confidence level for the four-body and chargino-mediated decays, respectively. A statistical combination of the results of the analysis has been performed with the results of a previously published CMS results in the 0ℓ channel of the same signal processes. The combined limits provide some of the most stringent limits on the allowed top squark masses in the compressed region of the spectrum.

Appendix

A.1 Materials for reinterpretations

In order for the results of this analyses to be usable by the high energy physics community, in addition to published results [18] several additional ingredients are provided in order to facilitate the reinterpretation of the results. As a cross check, the extra material were used by SModels Collaboration [124, 125] to reproduce the exclusion limits of the analysis as shown in Fig. A.1. The additional material include the covariance matrix of the background estimation (Fig. A.2), and acceptance-times-efficiency maps of the signal models in each of the regions (shown in inclusive regions in Fig. A.3 and Fig. A.4). The results of the analysis can then be reinterpreted in the context of any other signal scenario by using the covariance matrix, the background estimation (Tab. 5.5), and expected contribution of the specific signal model in the analysis regions. In this case, a simplified likelihood method [126] can be used to obtain upper limits on the signal of interest.

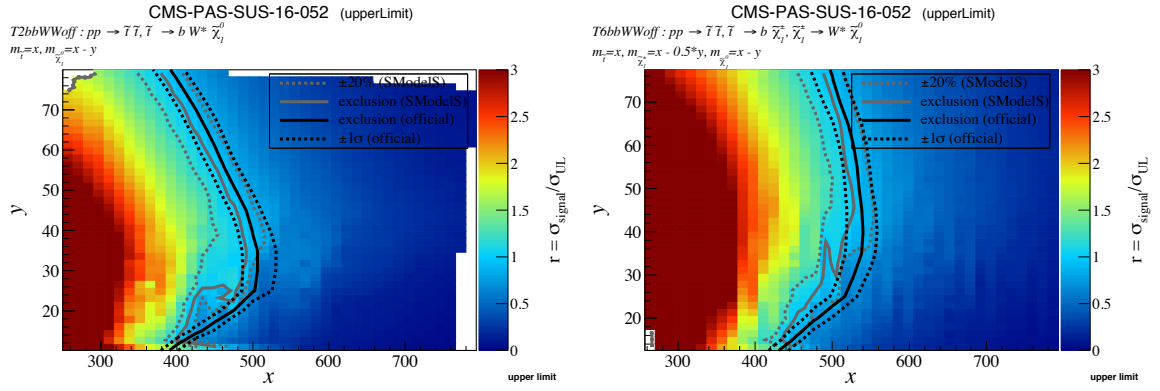

Figure A.1: Reproduced exclusion mass limits calculated by the SModels Collaboration [124, 125] using the results of this analysis, namely the background estimates, the signal efficiency maps (Fig. A.3 and Fig. A.4) and the covariance matrix (Fig. A.2).

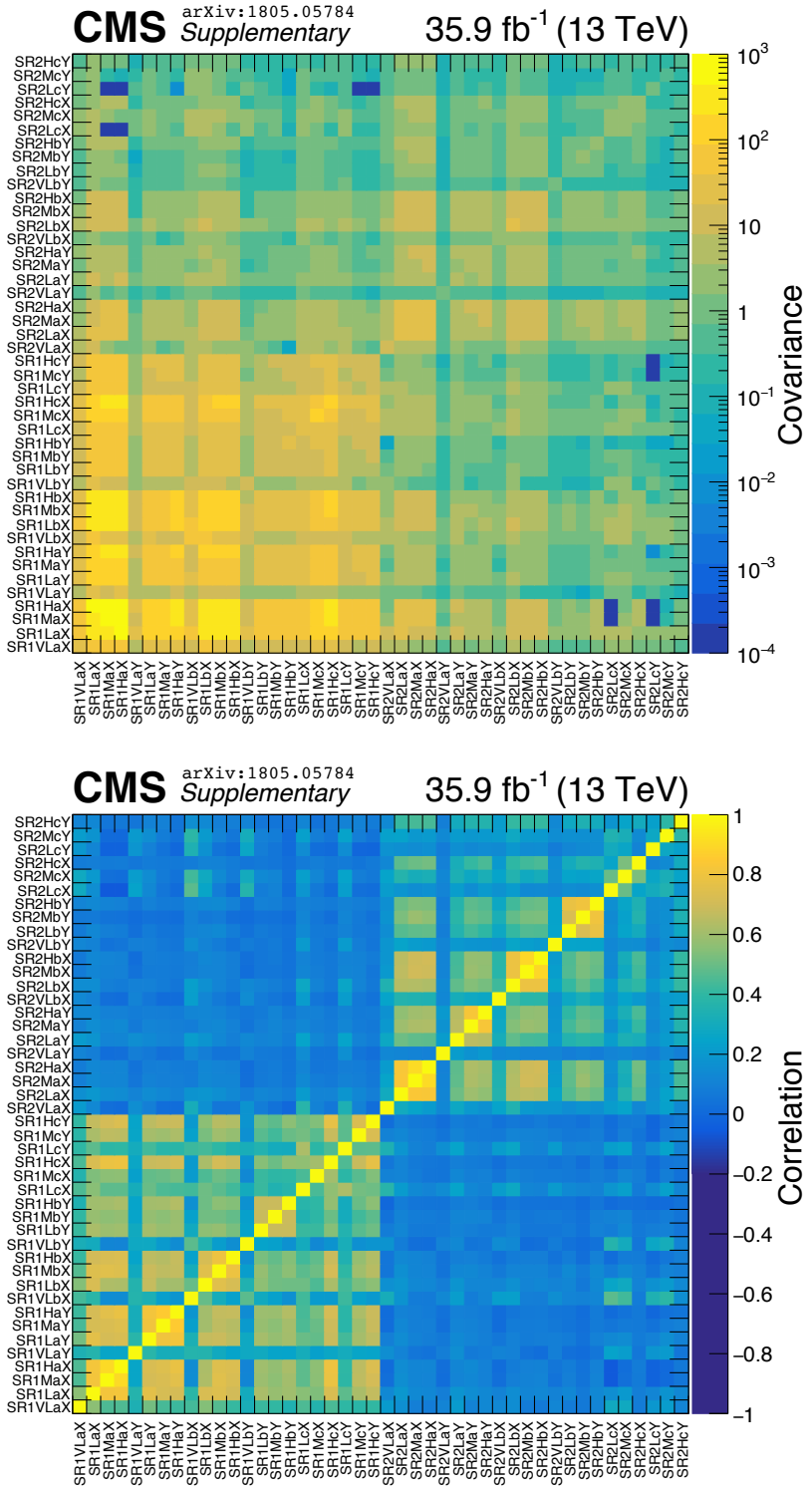

Figure A.2: The covariance (top) and correlation matrices (bottom) for the background estimates.

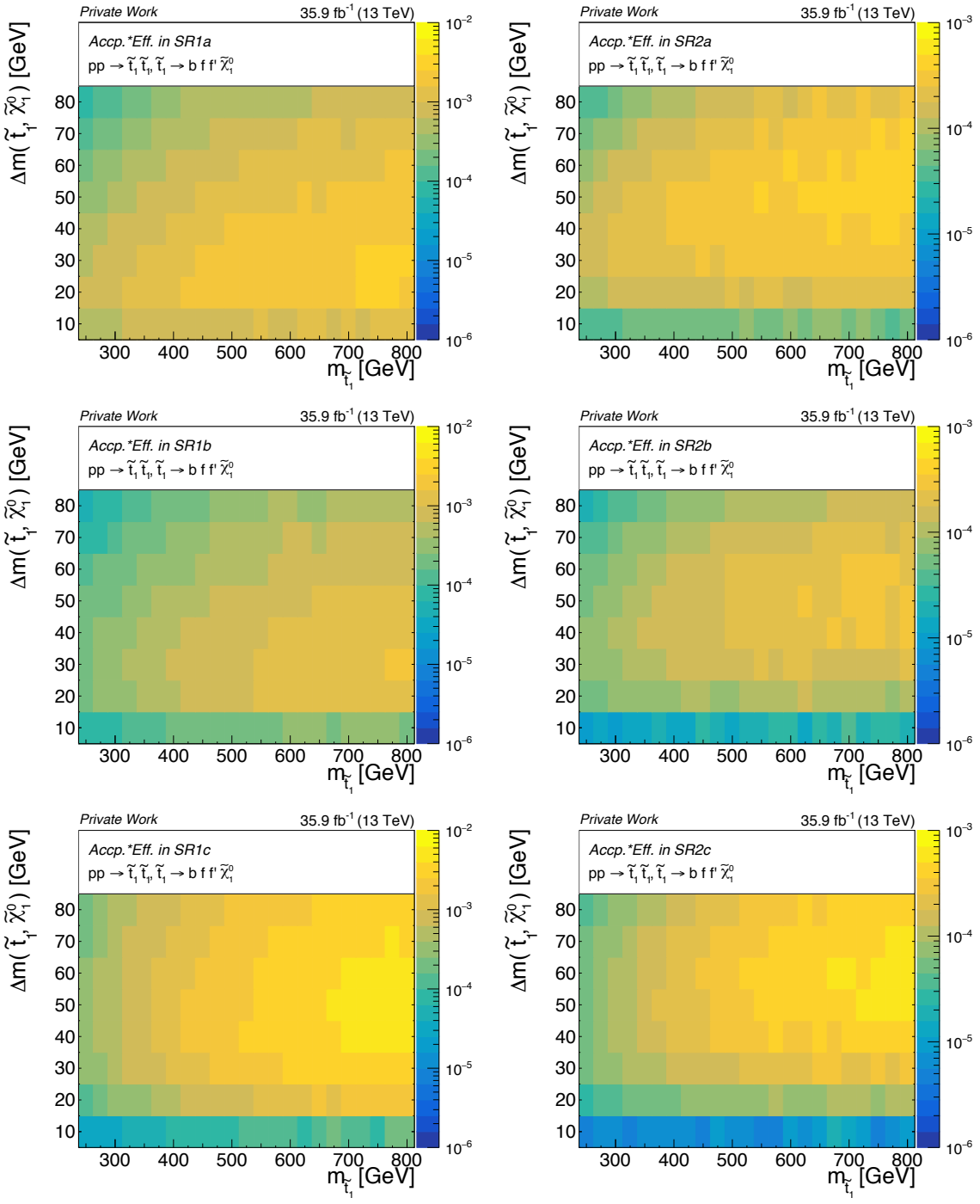

Figure A.3: Acceptance times efficiency maps for the four-body signal in $p_{\mathrm{T}}(\ell)$ and C_{T} inclusive signal regions.

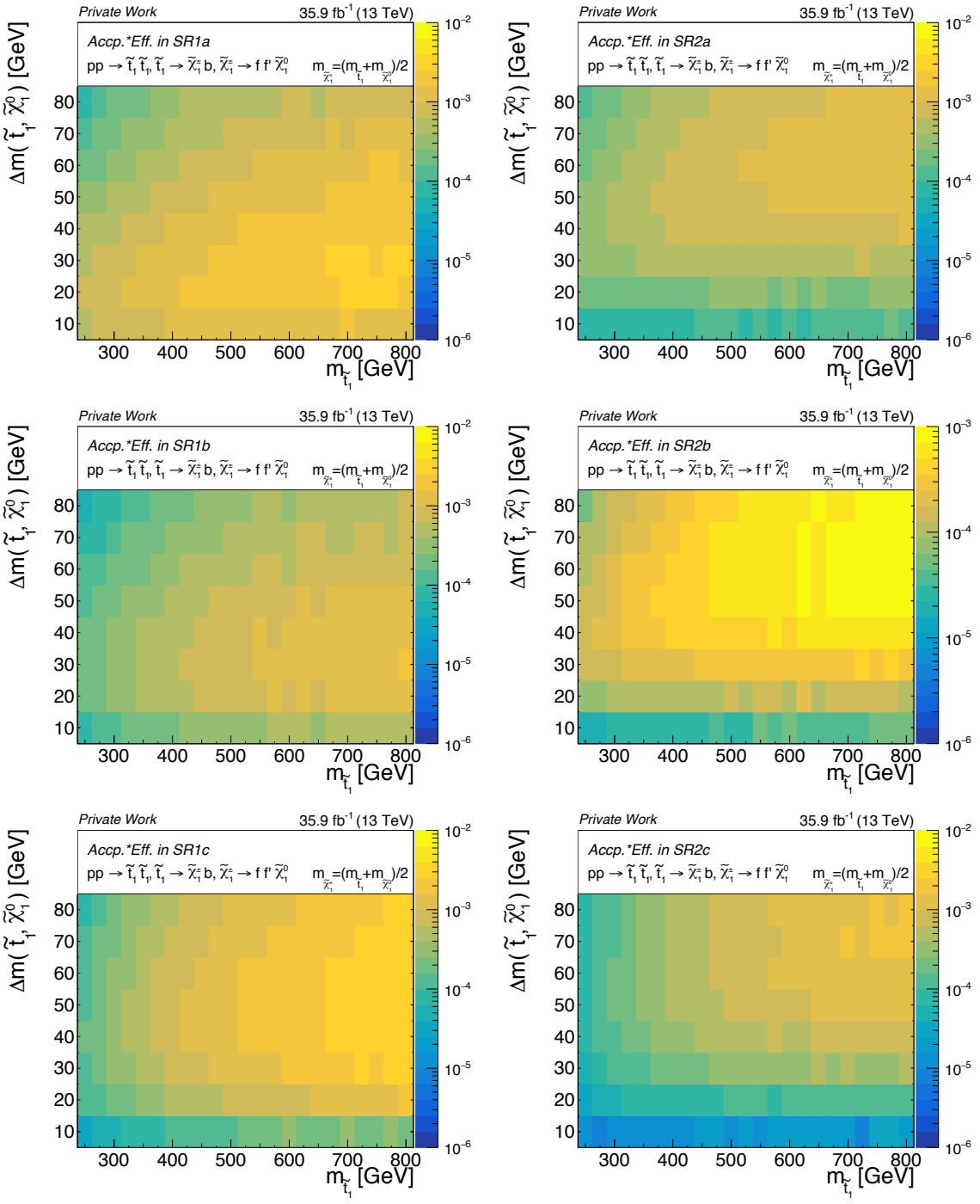

Figure A.4: Acceptance times efficiency maps for the chargino-mediated signal in $p_{\mathrm{T}}(\ell)$ and C_{T} inclusive signal regions.

A.2 Data event overlaps between the *0ℓ* and *1ℓ* analyses

The number of overlapping data events between the *0ℓ* and *1ℓ* regions are normalized to the average size of the two relevant regions and are shown in figures A.5-A.8.

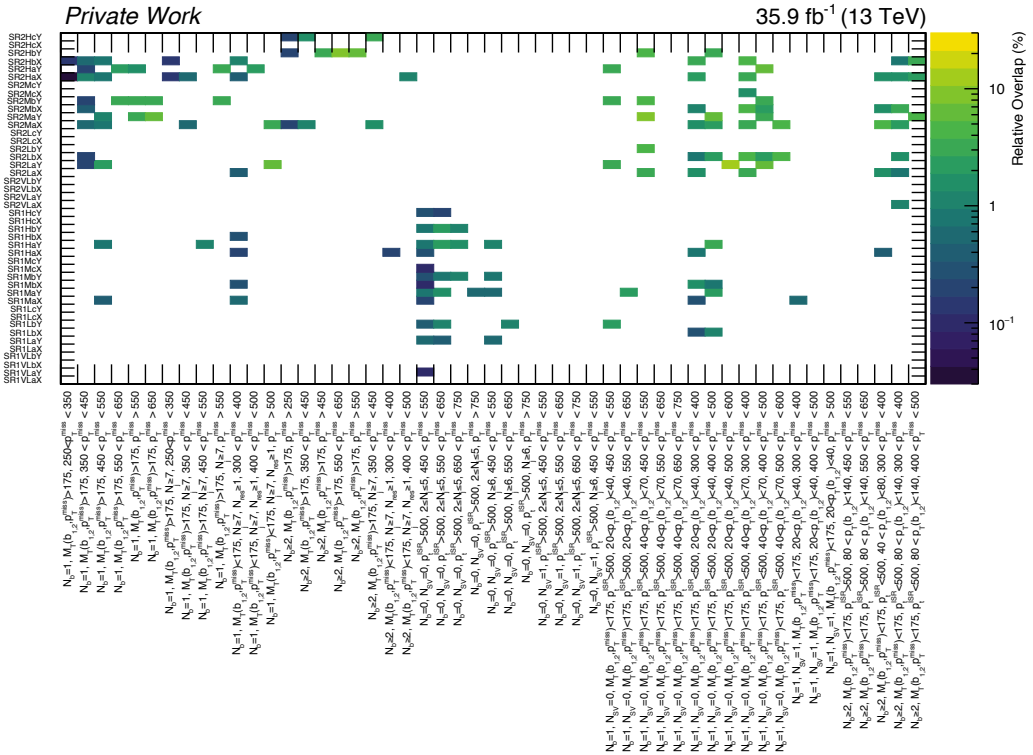

Figure A.5: Relative overlaps, as measured from data events, between the *1ℓ* SRs and *0ℓ* CRs normalized to the average sizes of the two regions.

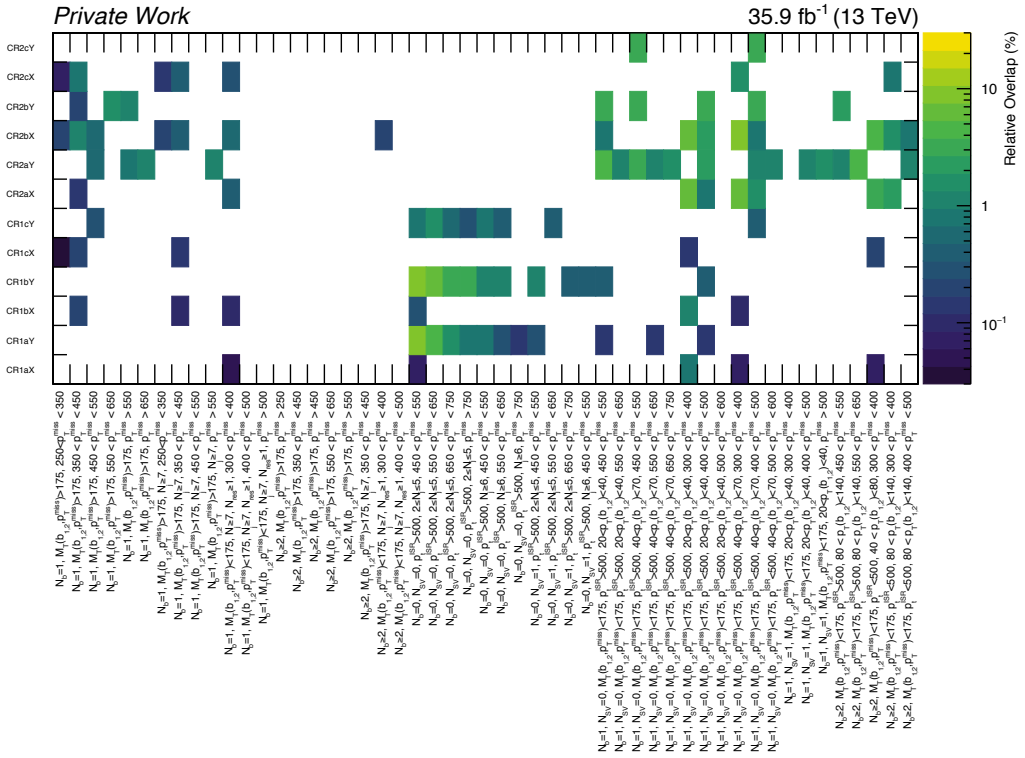

Figure A.6: Relative overlaps, as measured from data events, between the *1ℓ* CRs and *0ℓ* CRs normalized to the average sizes of the two regions.

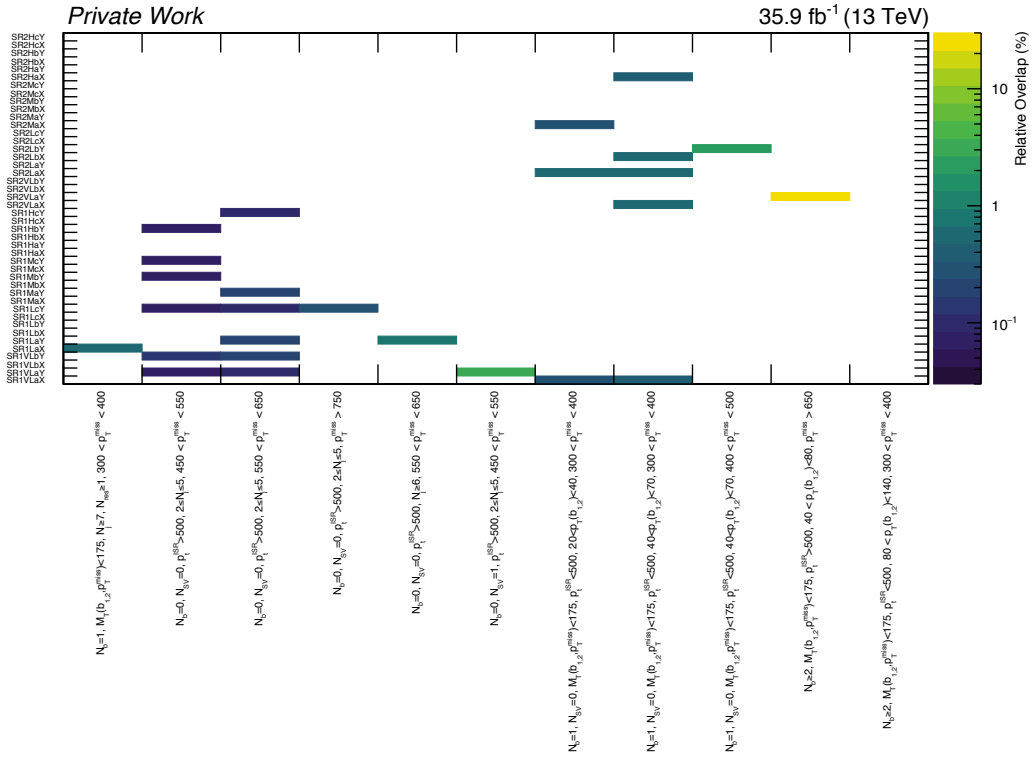

Figure A.7: Relative overlaps, as measured from data events, between the *1ℓ* SRs and *0ℓ* SRs normalized to the average sizes of the two regions.

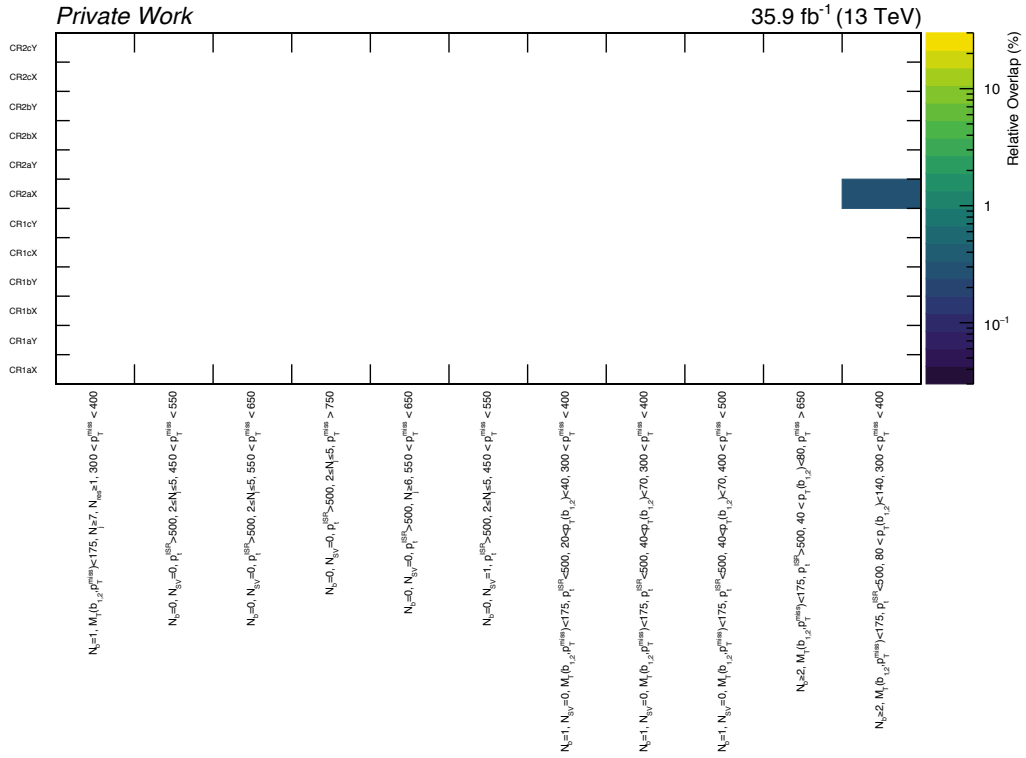

Figure A.8: Relative overlaps, as measured from data events, between the *1ℓ* CRs and *0ℓ* SRs normalized to the average sizes of the two regions.

List of Figures

List of Tables

Bibliography

[1] S. L. Glashow, "Partial Symmetries of Weak Interactions", *Nucl. Phys.* **22** (1961) 579–588, doi:10.1016/0029-5582(61)90469-2.

[2] A. Salam and J. C. Ward, "Weak and electromagnetic interactions", *Il Nuovo Cimento* **11** (February, 1959) 568–577, doi:10.1007/BF02726525.

[3] S. Weinberg, "A Model of Leptons", *Phys. Rev. Lett.* **19** (1967) 1264–1266, doi:10.1103/PhysRevLett.19.1264.

[4] P. W. Higgs, "Broken Symmetries and the Masses of Gauge Bosons", *Phys. Rev. Lett.* **13** (1964) 508–509, doi:10.1103/PhysRevLett.13.508.

[5] F. Englert and R. Brout, "Broken Symmetry and the Mass of Gauge Vector Mesons", *Phys. Rev. Lett.* **13** (1964) 321–323, doi:10.1103/PhysRevLett.13.321.

[6] ATLAS Collaboration, "Observation of a new particle in the search for the Standard Model Higgs boson with the ATLAS detector at the LHC", *Phys. Lett.* **B716** (2012) 1–29, doi:10.1016/j.physletb.2012.08.020, arXiv:1207.7214.

[7] CMS Collaboration, "Observation of a new boson at a mass of 125 GeV with the CMS experiment at the LHC", *Phys. Lett.* **B716** (2012) 30–61, doi:10.1016/j.physletb.2012.08.021, arXiv:1207.7235.

[8] Super-Kamiokande Collaboration, "Evidence for oscillation of atmospheric neutrinos", *Phys. Rev. Lett.* **81** (1998) 1562–1567, doi:10.1103/PhysRevLett.81.1562, arXiv:hep-ex/9807003.

[9] SNO Collaboration, "Measurement of the rate of $\nu_e + d \rightarrow p + p + e^-$ interactions produced by ^8B solar neutrinos at the Sudbury Neutrino Observatory", *Phys. Rev. Lett.* **87** (2001) 071301, doi:10.1103/PhysRevLett.87.071301, arXiv:nucl-ex/0106015.

[10] D. Clowe et al., "A direct empirical proof of the existence of dark matter", *Astrophys. J.* **648** (2006) L109–L113, doi:10.1086/508162, arXiv:astro-ph/0608407.

[11] A. G. Riess et al., "Observational Evidence from Supernovae for an Accelerating Universe and a Cosmological Constant", *AJ* **116** (September, 1998) 1009–1038, doi:10.1086/300499, arXiv:astro-ph/9805201.

[12] R. Haag, J. T. Łopuszański, and M. Sohnius, "All possible generators of supersymmetries of the S-matrix", *Nuclear Physics B* **88** (March, 1975) 257–274, doi:10.1016/0550-3213(75)90279-5.

[13] P. Ramond, "Dual Theory for Free Fermions", *Phys. Rev. D* **3** (May, 1971) 2415–2418, doi:10.1103/PhysRevD.3.2415.

[14] J. Wess and B. Zumino, "A Lagrangian Model Invariant Under Supergauge Transformations", *Phys. Lett.* **49B** (1974) 52, doi:10.1016/0370-2693(74)90578-4.

[15] J. Wess and B. Zumino, "Supergauge transformations in four dimensions", *Nuclear Physics B* **70** (1974), no. 1, 39 – 50, doi:https://doi.org/10.1016/0550-3213(74)90355-1.

[16] H. Nilles, "Supersymmetry, supergravity and particle physics", *Physics Reports* **110** (1984), no. 1, 1 – 162, doi:https://doi.org/10.1016/0370-1573(84)90008-5.

[17] CMS Collaboration, "Interpretation of Searches for Supersymmetry with simplified Models", *Phys. Rev.* **D88** (2013), no. 5, 052017, doi:10.1103/PhysRevD.88.052017, arXiv:1301.2175.

[18] CMS Collaboration, "Search for top squarks decaying via four-body or chargino-mediated modes in single-lepton final states in proton-proton collisions at $\sqrt{s} = 13$ TeV", *JHEP* **2018** (Sep, 2018) 65, doi:10.1007/JHEP09(2018)065, arXiv:1805.05784.

[19] CMS Collaboration, "Search for supersymmetry in events with at least one soft lepton, low jet multiplicity, and missing transverse momentum in proton-proton collisions at $\sqrt{s} = 13$ TeV", Technical Report CMS-PAS-SUS-16-031, CERN, Geneva, 2016.

[20] N. Rad, "Searches for strong production of supersymmetry at CMS", in *Proceedings, XXVI International Workshop on Deep-Inelastic Scattering and Related Subjects (DIS2018): Kobe, Japan, Apr 16-20, 2018*. https://pos.sissa.it/316/070/pdf.

[21] E. Noether, "Invariant variation problems", *Transport Theory and Statistical Physics* **1** (1971), no. 3, 186–207, doi:10.1080/00411457108231446, arXiv:https://doi.org/10.1080/00411457108231446.

[22] Particle Data Group Collaboration, "Review of Particle Physics", *Chin. Phys.* **C40** (2016), no. 10, 100001, doi:10.1088/1674-1137/40/10/100001.

[23] UA1 Collaboration, "Experimental Observation of Isolated Large Transverse Energy Electrons with Associated Missing Energy at s**(1/2) = 540-GeV", *Phys. Lett.* **B122** (1983) 103–116, doi:10.1016/0370-2693(83)91177-2. [,611(1983)].

[24] UA2 Collaboration, "Observation of Single Isolated Electrons of High Transverse Momentum in Events with Missing Transverse Energy at the CERN anti-p p Collider", *Phys. Lett.* **B122** (1983) 476–485, doi:10.1016/0370-2693(83)91605-2. [,7.45(1983)].

[25] UA2 Collaboration, "Evidence for Z0 —> e+ e- at the CERN anti-p p Collider", *Phys. Lett.* **B129** (1983) 130–140, doi:10.1016/0370-2693(83)90744-X. [,7.69(1983)].

[26] UA1 Collaboration, "Experimental Observation of Lepton Pairs of Invariant Mass Around 95-GeV/c**2 at the CERN SPS Collider", *Phys. Lett.* **B126** (1983) 398–410, doi:10.1016/0370-2693(83)90188-0. [,7.55(1983)].

[27] S. L. Glashow, "The renormalizability of vector meson interactions", *Nuclear Physics* **10** (1959) 107 – 117, doi:https://doi.org/10.1016/0029-5582(59)90196-8.

[28] J. Goldstone, "Field Theories with Superconductor Solutions", *Nuovo Cim.* **19** (1961) 154–164, doi:10.1007/BF02812722.

[29] Y. Nambu, "Quasi-Particles and Gauge Invariance in the Theory of Superconductivity", *Phys. Rev.* **117** (Feb, 1960) 648–663, doi:10.1103/PhysRev.117.648.

[30] J. Goldstone, A. Salam, and S. Weinberg, "Broken Symmetries", *Physical Review* **127** (August, 1962) 965–970, doi:10.1103/PhysRev.127.965.

[31] CMS Collaboration, "Observation of a new boson at a mass of 125 GeV with the CMS experiment at the LHC", *Phys. Lett.* **B716** (2012) 30–61, doi:10.1016/j.physletb.2012.08.021, arXiv:1207.7235.

[32] ATLAS Collaboration, "Observation of Higgs boson production in association with a top quark pair at the LHC with the ATLAS detector", arXiv:1806.00425.

[33] CMS Collaboration, "Observation of $t\bar{t}H$ production", *Phys. Rev. Lett.* **120** (2018), no. 23, 231801, doi:10.1103/PhysRevLett.120.231801, arXiv:1804.02610.

[34] ATLAS Collaboration, "Observation of $H \to b\bar{b}$ decays and VH production with the ATLAS detector", *Phys. Lett.* **B786** (2018) 59–86, doi:10.1016/j.physletb.2018.09.013, arXiv:1808.08238.

[35] CMS Collaboration, "Observation of Higgs boson decay to bottom quarks", *Phys. Rev. Lett.* **121** (2018), no. 12, 121801, doi:10.1103/PhysRevLett.121.121801, arXiv:1808.08242.

[36] CMS Collaboration, "Observation of the Higgs boson decay to a pair of τ leptons with the CMS detector", *Phys. Lett.* **B779** (2018) 283–316, doi:10.1016/j.physletb.2018.02.004, arXiv:1708.00373.

[37] ATLAS, CMS Collaboration, "Measurements of the Higgs boson production and decay rates and constraints on its couplings from a combined ATLAS and CMS analysis of the LHC pp collision data at $\sqrt{s} = 7$ and 8 TeV", *JHEP* **08** (2016) 045, doi:10.1007/JHEP08(2016)045, arXiv:1606.02266.

[38] B. Odom, D. Hanneke, B. D'Urso, and G. Gabrielse, "New Measurement of the Electron Magnetic Moment Using a One-Electron Quantum Cyclotron", *Physical Review Letters* **97** (July, 2006) 030801, doi:10.1103/PhysRevLett.97.030801.

[39] Planck Collaboration, "Planck 2018 results. VI. Cosmological parameters", arXiv:1807.06209.

[40] R. J. Adler, B. Casey, and O. C. Jacob, "Vacuum catastrophe: An elementary exposition of the cosmological constant problem", *American Journal of Physics* **63** (July, 1995) 620–626, doi:10.1119/1.17850.

[41] WMAP Collaboration, "Seven-Year Wilkinson Microwave Anisotropy Probe (WMAP) Observations: Cosmological Interpretation", *Astrophys. J. Suppl.* **192** (2011) 18, doi:10.1088/0067-0049/192/2/18, arXiv:1001.4538.

[42] G. Steigman, "Primordial Nucleosynthesis: The Predicted and Observed Abundances and Their Consequences", *PoS* **NICXI** (2010) 001, doi:10.22323/1.100.0001, arXiv:1008.4765.

[43] L. Canetti, M. Drewes, and M. Shaposhnikov, "Matter and Antimatter in the Universe", *New J. Phys.* **14** (2012) 095012, doi:10.1088/1367-2630/14/9/095012, arXiv:1204.4186.

[44] CMS Collaboration, "Summaries of CMS cross section measurements", *Public CMS Twiki* (2016). http://go.web.cern.ch/go/pNj7.

[45] S. Coleman and J. Mandula, "All Possible Symmetries of the S Matrix", *Phys. Rev.* **159** (July, 1967) 1251–1256, doi:10.1103/PhysRev.159.1251.

[46] S. Weinberg and E. Witten, "Limits on massless particles", *Physics Letters B* **96** (October, 1980) 59–62, doi:10.1016/0370-2693(80)90212-9.

[47] S. P. Martin, "A Supersymmetry primer", doi:10.1142/9789812839657_0001,10.1142/9789814307505_0001, arXiv:hep-ph/9709356. [Adv. Ser. Direct. High Energy Phys.18,1(1998)].

[48] N. Sakai, "Naturalnes in supersymmetric GUTS", *Zeitschrift für Physik C Particles and Fields* **11** (Jun, 1981) 153–157, doi:10.1007/BF01573998.

[49] R. K. Kaul and P. Majumdar, "Cancellation of quadratically divergent mass corrections in globally supersymmetric spontaneously broken gauge theories", *Nuclear Physics B* **199** (1982), no. 1, 36 – 58, doi:https://doi.org/10.1016/0550-3213(82)90565-X.

[50] B. de Carlos and J. A. Casas, "One loop analysis of the electroweak breaking in supersymmetric models and the fine tuning problem", *Phys. Lett.* **B309** (1993) 320–328, doi:10.1016/0370-2693(93)90940-J, arXiv:hep-ph/9303291.

[51] A. Delgado et al., "The light stop window", *Eur. Phys. J.* **C73** (2013), no. 3, 2370, doi:10.1140/epjc/s10052-013-2370-5, arXiv:1212.6847.

[52] R. Gröber, M. M. Mühlleitner, E. Popenda, and A. Wlotzka, "Light Stop Decays: Implications for LHC Searches", *Eur. Phys. J.* **C75** (2015) 420, doi:10.1140/epjc/s10052-015-3626-z, arXiv:1408.4662.

[53] W. Beenakker et al., "Stop production at hadron colliders", *Nucl. Phys.* **B515** (1998) 3–14, doi:10.1016/S0550-3213(98)00014-5, arXiv:hep-ph/9710451.

[54] C. Borschensky et al., "Squark and gluino production cross sections in pp collisions at $\sqrt{s}$ = 13, 14, 33 and 100 TeV", *Eur. Phys. J.* **C74** (2014), no. 12, 3174, doi:10.1140/epjc/s10052-014-3174-y, arXiv:1407.5066.

[55] LHC SUSY Cross Section Working Group, "SUSY Cross Sections", *LHC Physics Twiki*. https://twiki.cern.ch/twiki/bin/view/CMSPublic/SUSYSMSSummaryPlots13TeV.

[56] O. S. Brüning et al., "LHC Design Report". CERN Yellow Reports: Monographs. CERN, Geneva, 2004. https://cds.cern.ch/record/782076.

[57] J. Haffner, "The CERN accelerator complex. Complexe des accélérateurs du CERN",. General Photo.

[58] CMS Collaboration, "Public CMS Luminosity Information", *Public CMS Twiki* (2016). https://twiki.cern.ch/twiki/bin/view/CMSPublic/LumiPublicResults.

[59] J.-L. Caron, "LHC Layout. Schema general du LHC.", (Sep, 1997). AC Collection. Legacy of AC. Pictures from 1992 to 2002.

[60] CMS Collaboration, "The CMS Experiment at the CERN LHC", *JINST* **3** (2008) S08004, doi:10.1088/1748-0221/3/08/S08004.

[61] CMS Collaboration, "CMS physics: Technical design report", *CERN-LHCC-2006-001* (2006).

[62] CMS Collaboration, "Interactive Slice of the CMS detector",. https://cds.cern.ch/record/2205172.

[63] CMS Collaboration, "Precise Mapping of the Magnetic Field in the CMS Barrel Yoke using Cosmic Rays", *JINST* **5** (2010) T03021, doi:10.1088/1748-0221/5/03/T03021, arXiv:0910.5530.

[64] CMS Collaboration, "Energy Calibration and Resolution of the CMS Electromagnetic Calorimeter in *pp* Collisions at $\sqrt{s} = 7$ TeV", *JINST* **8** (2013) P09009, doi:10.1088/1748-0221/8/09/P09009, arXiv:1306.2016. [JINST8,9009(2013)].

[65] USCMS, ECAL/HCAL Collaboration, "The CMS barrel calorimeter response to particle beams from 2-GeV/c to 350-GeV/c", *Eur. Phys. J.* **C60** (2009) 359–373, doi:10.1140/epjc/s10052-009-0959-5,10.1140/epjc/s10052-009-1024-0. [Erratum: Eur. Phys. J.C61,353(2009)].

[66] CMS Collaboration, "Measurement of the properties of a Higgs boson in the four-lepton final state", *Phys. Rev.* **D89** (2014), no. 9, 092007, doi:10.1103/PhysRevD.89.092007, arXiv:1312.5353.

[67] ATLAS Collaboration, "Measurements of Higgs boson production and couplings in the four-lepton channel in pp collisions at center-of-mass energies of 7 and 8 TeV with the ATLAS detector", *Phys. Rev.* **D91** (2015), no. 1, 012006, doi:10.1103/PhysRevD.91.012006, arXiv:1408.5191.

[68] CMS Collaboration, "Performance of CMS muon reconstruction in *pp* collision events at $\sqrt{s} = 7$ TeV", *JINST* **7** (2012) P10002, doi:10.1088/1748-0221/7/10/P10002, arXiv:1206.4071.

[69] CMS Collaboration, "Particle-flow reconstruction and global event description with the CMS detector", *JINST* **12** (2017), no. 10, P10003, doi:10.1088/1748-0221/12/10/P10003, arXiv:1706.04965.

[70] CMS Collaboration, "Description and performance of track and primary-vertex reconstruction with the CMS tracker", *JINST* **9** (2014), no. 10, P10009, doi:10.1088/1748-0221/9/10/P10009, arXiv:1405.6569.

[71] R. Fruhwirth, "Application of Kalman filtering to track and vertex fitting", *Nucl. Instrum. Meth.* **A262** (1987) 444–450, doi:10.1016/0168-9002(87)90887-4.

[72] W.Adam, B. Mangano, T. Speer, T.Todorov, "Track reconstruction in the CMS tracker", 2006. *CMS Note* CMS-NOTE-2006-041, https://cds.cern.ch/record/934067.

[73] HCAL Calibration Group Collaboration, O. Kodolova, "HCAL calibration in high luminosity environment", in *Proceedings, CMS Workshop: Perspectives on Physics and on CMS at Very High Luminosity, HL-LHC: Alushta, Crimea, Ukraine, May 28–31, 2012*, pp. 169–175. 2013.

[74] R. Frühwirth and A. Strandlie, "Track fitting with ambiguities and noise: A study of elastic tracking and nonlinear filters", *Comput. Phys. Commun.* **120** (1999), no. 2-3, 197–214, doi:10.1016/S0010-4655(99)00231-3.

[75] K. Rose, "Deterministic Annealing for Clustering, Compression, Classification, Regression, and Related Optimization Problems", in *Proceedings of the IEEE*, pp. 2210–2239. 1998. doi:10.1109/5.726788.

[76] R. Fruhwirth, W. Waltenberger, and P. Vanlaer, "Adaptive vertex fitting", *J. Phys.* **G34** (2007) N343, doi:10.1088/0954-3899/34/12/N01.

[77] CMS Collaboration, "Tracking and Primary Vertex Results in First 7 TeV Collisions", Technical Report CMS-PAS-TRK-10-005, CERN, Geneva, 2010.

[78] CMS Collaboration, "Performance of the CMS muon detector and muon reconstruction with proton-proton collisions at $\sqrt{s} = 13$ TeV", *JINST* **13** (2018), no. 06, P06015, doi:10.1088/1748-0221/13/06/P06015, arXiv:1804.04528.

[79] CMS Collaboration, "Performance of Electron Reconstruction and Selection with the CMS Detector in Proton-Proton Collisions at $\sqrt{s} = 8$ TeV", *JINST* **10** (2015), no. 06, P06005, doi:10.1088/1748-0221/10/06/P06005, arXiv:1502.02701.

[80] W. Adam, R. Frühwirth, A. Strandlie, and T. Todor, "Reconstruction of Electrons with the Gaussian-Sum Filter in the CMS Tracker at the LHC",.

[81] A. A. Anuar, "Electrons and photons at High Level Trigger in CMS for Run II", *J. Phys. Conf. Ser.* **664** (2015), no. 8, 082001, doi:10.1088/1742-6596/664/8/082001.

[82] M. Cacciari, G. P. Salam, and G. Soyez, "The Anti-k(t) jet clustering algorithm", *JHEP* **04** (2008) 063, doi:10.1088/1126-6708/2008/04/063, arXiv:0802.1189.

[83] CMS Collaboration, "Jet algorithms performance in 13 TeV data", Technical Report CMS-PAS-JME-16-003, CERN, Geneva, 2017. http://cds.cern.ch/record/2256875.

[84] CMS Collaboration, "Determination of Jet Energy Calibration and Transverse Momentum Resolution in CMS", *JINST* **6** (2011) P11002, doi:10.1088/1748-0221/6/11/P11002, arXiv:1107.4277.

[85] CMS Collaboration, "Jet energy scale and resolution performances with 13TeV data",. https://cds.cern.ch/record/2160347.

[86] CMS Collaboration, "Identification of heavy-flavour jets with the CMS detector in pp collisions at 13 TeV", *JINST* **13** (2018), no. 05, P05011, doi:10.1088/1748-0221/13/05/P05011, arXiv:1712.07158.

[87] D. Guest et al., "Jet Flavor Classification in High-Energy Physics with Deep Neural Networks", *Phys. Rev.* **D94** (2016), no. 11, 112002, doi:10.1103/PhysRevD.94.112002, arXiv:1607.08633.

[88] CMS Collaboration, "Search for supersymmetry in events with soft leptons, low jet multiplicity, and missing transverse energy in proton–proton collisions at $\sqrt{s}$=8 TeV", *Phys. Lett.* **B759** (2016) 9–35, doi:10.1016/j.physletb.2016.05.033, arXiv:1512.08002.

[89] T. Sjöstrand, S. Mrenna, and P. Z. Skands, "PYTHIA 6.4 physics and manual", *JHEP* **05** (2006) 026, doi:10.1088/1126-6708/2006/05/026, arXiv:hep-ph/0603175.

[90] T. Sjöstrand, S. Mrenna, and P. Z. Skands, "A Brief Introduction to PYTHIA 8.1", *Comput. Phys. Commun.* **178** (2008) 852, doi:10.1016/j.cpc.2008.01.036, arXiv:0710.3820.

[91] S. Alioli, P. Nason, C. Oleari, and E. Re, "NLO single-top production matched with shower in POWHEG: s- and t-channel contributions", *JHEP* **09** (2009) 111, doi:10.1088/1126-6708/2009/09/111, arXiv:0907.4076. [Erratum: doi:10.1007/JHEP02(2010)011].

[92] E. Re, "Single-top Wt-channel production matched with parton showers using the POWHEG method", *Eur. Phys. J. C* **71** (2011) 1547, doi:10.1140/epjc/s10052-011-1547-z, arXiv:1009.2450.

[93] J. Alwall et al., "MadGraph 5: going beyond", *JHEP* **06** (2011) 128, doi:10.1007/JHEP06(2011)128, arXiv:1106.0522.

[94] J. Alwall et al., "The automated computation of tree-level and next-to-leading order differential cross sections, and their matching to parton shower simulations", *JHEP* **07** (2014) 079, doi:10.1007/JHEP07(2014)079, arXiv:1405.0301.

[95] NNPDF Collaboration, "Parton distributions for the LHC Run II", *JHEP* **04** (2015) 040, doi:10.1007/JHEP04(2015)040, arXiv:1410.8849.

[96] J. Alwall et al., "Comparative study of various algorithms for the merging of parton showers and matrix elements in hadronic collisions", *Eur. Phys. J.* **C53** (2008) 473–500, doi:10.1140/epjc/s10052-007-0490-5, arXiv:0706.2569.

[97] CMS Collaboration, "Event generator tunes obtained from underlying event and multiparton scattering measurements", *Eur. Phys. J.* **C76** (2016), no. 3, 155, doi:10.1140/epjc/s10052-016-3988-x, arXiv:1512.00815.

[98] F. Kraus, "QCD & Monte Carlo Event Generators". Monte Carlo Lectures, 2012. "https://www.ippp.dur.ac.uk/~krauss/Lectures/MonteCarlos/Heidelberg14.pdf".

[99] GEANT4 Collaboration, "GEANT4: A Simulation toolkit", *Nucl. Instrum. Meth.* **A506** (2003) 250–303, doi:10.1016/S0168-9002(03)01368-8.

[100] CMS Collaboration, "The fast simulation of the CMS Detector at LHC", *J. Phys. Conf. Ser.* **331** (2011) 032049, doi:10.1088/1742-6596/331/3/032049.

[101] CMS Collaboration, "CMS Luminosity Measurements for the 2016 Data Taking Period", Technical Report CMS-PAS-LUM-17-001, CERN, Geneva, 2017. "https://cds.cern.ch/record/2257069".

[102] CMS Collaboration, "Performance of missing transverse momentum in pp collisions at sqrt(s)=13 TeV using the CMS detector", Technical Report CMS-PAS-JME-17-001, CERN, Geneva, 2018.

[103] CMS Collaboration, "Measurement of the inelastic proton-proton cross section at $\sqrt{s} = 13$ TeV", *JHEP* **07** (2018) 161, doi:10.1007/JHEP07(2018)161, arXiv:1802.02613.

[104] CMS Collaboration, "Search for supersymmetry in multijet events with missing transverse momentum in proton-proton collisions at 13 TeV", *Phys. Rev.* **D96** (2017), no. 3, 032003, doi:10.1103/PhysRevD.96.032003, arXiv:1704.07781.

[105] CMS Collaboration, "Search for electroweak production of charginos and neutralinos in WH events in proton-proton collisions at $\sqrt{s} = 13$ TeV", *JHEP* **11** (2017) 029, doi:10.1007/JHEP11(2017)029, arXiv:1706.09933.

[106] CMS Collaboration, "Measurements of Inclusive W and Z Cross Sections in pp Collisions at $\sqrt{s} = 7$ TeV", *JHEP* **01** (2011) 080, doi:10.1007/JHEP01(2011)080, arXiv:1012.2466.

[107] I. Mikulec, "Lepton efficiencies for identification, isolation and impact parameter requirements using the tag-and-probe method". Private Communication.

[108] D. Spitzbart, "Search for supersymmetry in the single lepton final state in 13 TeV pp collisions with the CMS experiment", Master's thesis, Technische Universität Wien, 2016. "http://repositum.tuwien.ac.at/obvutwhs/content/titleinfo/1370375".

[109] CMS Collaboration, "Search for new physics in same-sign dilepton events in proton–proton collisions at $\sqrt{s} = 13\,\text{TeV}$", *Eur. Phys. J.* **C76** (2016), no. 8, 439, doi:10.1140/epjc/s10052-016-4261-z, arXiv:1605.03171.

[110] M. Zarucki, "Fake rate background estimation method". Private Communication.

[111] G. Cowan, K. Cranmer, E. Gross, and O. Vitells, "Asymptotic formulae for likelihood-based tests of new physics", *Eur. Phys. J.* **C71** (2011) 1554, doi:10.1140/epjc/s10052-011-1554-0,10.1140/epjc/s10052-013-2501-z, arXiv:1007.1727. [Erratum: Eur. Phys. J.C73,2501(2013)].

[112] ATLAS Collaboration, CMS Collaboration, LHC Higgs Combination Group, "Procedure for the LHC Higgs boson search combination in Summer 2011", Technical Report CMS-NOTE-2011-005. ATL-PHYS-PUB-2011-11, CERN, Geneva, Aug, 2011.

[113] CMS Collaboration, "Search for direct production of supersymmetric partners of the top quark in the all-jets final state in proton-proton collisions at $\sqrt{s} = 13$ TeV", *JHEP* **10** (2017) 005, doi:10.1007/JHEP10(2017)005, arXiv:1707.03316.

[114] CMS Collaboration, "Public CMS SUSY 13 TeV Summary Plots", *Public CMS Wiki* (2018). https://twiki.cern.ch/twiki/bin/view/CMSPublic/PhysicsResultsSUS#Run_2_Summary_plots_13_TeV_2016.

[115] B. Fuks, M. Klasen, D. R. Lamprea, and M. Rothering, "Precision predictions for electroweak superpartner production at hadron colliders with Resummino", *Eur. Phys. J.* **C73** (2013) 2480, doi:10.1140/epjc/s10052-013-2480-0, arXiv:1304.0790.

[116] W. Beenakker et al., "The Production of charginos / neutralinos and sleptons at hadron colliders", *Phys. Rev. Lett.* **83** (1999) 3780–3783, doi:10.1103/PhysRevLett.100.029901,10.1103/PhysRevLett.83.3780, arXiv:hep-ph/9906298. [Erratum: Phys. Rev. Lett.100,029901(2008)].

[117] MSSM Working Group Collaboration, A. Djouadi et al., "The Minimal supersymmetric standard model: Group summary report", in *GDR (Groupement De Recherche) - Supersymetrie Montpellier, France, April 15-17, 1998*. 1998. arXiv:hep-ph/9901246.

[118] CMS Collaboration, "Search for new physics in events with two soft oppositely charged leptons and missing transverse momentum in proton-proton collisions at $\sqrt{s} =$ 13 TeV", *Phys. Lett.* **B782** (2018) 440–467, doi:10.1016/j.physletb.2018.05.062, arXiv:1801.01846.

[119] M. Zarucki, "SUSY Trigger Developments for 2018". Private Communication.

[120] CMS Collaboration, "Search for long-lived particles with displaced vertices in multijet events in proton-proton collisions at $\sqrt{s}$ =13 TeV", arXiv:1808.03078.

[121] CMS Collaboration, "Search for disappearing tracks as a signature of new long-lived particles in proton-proton collisions at $\sqrt{s} = 13$ TeV", *JHEP* **08** (2018) 016, doi:10.1007/JHEP08(2018)016, arXiv:1804.07321.

[122] CMS Collaboration, "Search for long-lived charged particles in proton-proton collisions at $\sqrt{s} = 13$ TeV", *Phys. Rev.* **D94** (2016), no. 11, 112004, doi:10.1103/PhysRevD.94.112004, arXiv:1609.08382.

[123] CMS Collaboration, "Search for the pair production of third-generation squarks with two-body decays to a bottom or charm quark and a neutralino in proton–proton collisions at $\sqrt{s} = 13$ TeV", *Phys. Lett.* **B778** (2018) 263–291, doi:10.1016/j.physletb.2018.01.012, arXiv:1707.07274.

[124] F. Ambrogi et al., "SModelS v1.1 user manual: Improving simplified model constraints with efficiency maps", *Comput. Phys. Commun.* **227** (2018) 72–98, doi:10.1016/j.cpc.2018.02.007, arXiv:1701.06586.

[125] J. Dutta, S. Kraml, A. Lessa, and W. Waltenberger, "SModelS extension with the CMS supersymmetry search results from Run 2", *LHEP* **1** (2018), no. 1, 5–12, doi:10.31526/LHEP.1.2018.02, arXiv:1803.02204.

[126] CMS Collaboration, "Simplified likelihood for the re-interpretation of public CMS results", Technical Report CMS-NOTE-2017-001. CERN-CMS-NOTE-2017-001, CERN, Geneva, Jan, 2017.

Acknowledgements

"Educate yourself for some years, reap the benefits for a lifetime."

This is a rough translation of what my grandfather used to tell his children, my cousins and me as we were growing up. He learned to read and write as a middle-aged adult, which is probably why he valued education more than anyone else that I have known. This simple saying resonated with me throughout my studies and particularly during the challenging times. Now, although my official education may be over, I know that the learning process is far from it. I am deeply grateful to so many people who have helped me in different ways, within and outside the academic life. Without many of them writing this thesis would have been much more grueling, and without some, this thesis wouldn't have been possible.

First of all, I would like to thank my supervisor Prof. Claudia Wulz for accepting me as her student and for her continuous support throughout my PhD studies. A special thanks goes to Ivan Mikulec and Wolfgang Adam, working with whom has been a priceless learning experience. Their patient guidance, constructive advice and well-rounded knowledge of the topic are the foundations on which this thesis is built on. At times, I was frustrated for not having an advisor in Vienna, but looking back, I feel extremely fortunate for having had these three brilliant advisors who always took the time out of their busy days to answer my questions or discuss my concerns. I particularly want to thank them for making my stays at CERN more pleasurable with the multiple hiking and ski trips, dinner invitations and the brief sailing lesson on lac Léman.

I am thankful to the *Doktoratskolleg - Particles and Interactions* (DKPI) not just for providing the funding for my research but also creating the community of faculties and students and organizing all the gatherings at colloquia, summer schools. I also want to thank the colleagues at HEPHY, Jochen schieck, Robert Schöfbeck, Vasile Ghete, Manfred Jeitler, Dietrich Liko, Martin Flechl, Joseph Pradler, Wolfgang Waltenberger, Ilse Krätschmer, Suchita Kulkarni, Xiaoyong Chu, and Alberto Escalante for always taking the time to answer questions and discuss various topics, whether during lunch or at 1 a.m. on a Saturday.

A personal thanks goes to my Apostelgasse, Wohllebengasse and Nikolsdorfer comrads: Ece Asilar (whose laughter has been engraved in the walls of WLG!), Daniel Spitzbart, Ma-

teusz Zarucki (I hope I spelled your name right this time!), Federico Ambrogi, Johannes Brandstetter, Thomas Madlener, and Lukas$_i$ with i=$1, 2...N$. The shared sufferings and the common battles that I fought besides them turned fellow colleagues into good friends. From the chipmunk infestations in Arambol, to the long nights at CERN followed by FriesZeit at R1, or finding our way through the madness of Shinjuku, and the eternal battle between python and ROOT, no matter what kind of challenges faced us, these words of wisdom helped us get through: *"Things come as they are!"* Indeed they do! Indeed they do.

I would like to thank all the friends, old and new, who turned the past few years from "barely bearable" to enjoyable. I especially want to thank my dearest friend, Yalda Zamani, for accompanying me through the difficult times and the happy times of the past years. Speaking with her always takes my mind to a more peaceful place and seeing her performances never ceases to take my breath away! Thanks to Anna Dobrosovestnova for all the *constructivist* breakfast/lunch/dinner chats and the hangouts with our mutual friend Kelly. I also want to thank the VB friends, Tajna for always being a joyful companion on bike rides, Ahmed for distracting the people standing by the net, Yan for yelling at me for my terrible foot-work, Josef for just being a classy human being, and Stefan for not doing *The Stefan*.

I became an uncle around the same time I had my interview at DKPI, and since then I have been fortunate to have two more nephews. It has been such a bitter-sweet experience seeing Arshan, Shayan, and Tiam grow half-way across the globe but it always brings me great pleasure to see their cheerful smiles and endless energy. Words can't describe how grateful I am to my family for their unconditional support and continuous encouragement, even from a few thousand kilometers away. Thanks Maman for showing me how to be kind and strong and thanks Baba for inspiring me to push myself beyond what seems possible. Thanks Omid for making me memorize sines and cosines when I had no idea what they were and thanks Payam for always finding ways to make us laugh. Thanks Shideh and Azam for being the best sisters that I never had. Love you all!